Fall 12-2-2011

Two dimensional electron gas at oxide interfaces

Karolina Janicka
University of Nebraska-Lincoln, janicka@bigred.unl.edu

TWO DIMENSIONAL ELECTRON GAS AT OXIDE INTERFACES

by

Karolina Janicka

A DISSERTATION

Presented to the Faculty of

The Graduate College at the University of Nebraska

In Partial Fulfillment of Requirements

For the Degree of Doctor of Philosophy

Major: Physics and Astronomy

Under the Supervision of Professor Evgeny Y. Tsymbal

Lincoln, Nebraska

December, 2011

TWO DIMENSIONAL ELECTRON GAS AT OXIDE INTERFACES

Karolina Janicka, Ph.D.

University of Nebraska, 2011

Adviser: Evgeny Y. Tsymbal

Extraordinary phenomena can occur at the interface between two oxide materials. A spectacular example is a formation of a two-dimensional electron gas (2DEG) at the $SrTiO_3/LaAlO_3$ interface. In this dissertation the properties of the 2DEG are investigated from first principles.

The spatial extent of the 2DEG formed at the $SrTiO_3/LaAlO_3$ n-type interface is studied. It is shown that the confinement of the 2DEG is controlled by metal induced gap states formed in the band gap of $SrTiO_3$. The confinement width is then determined by the attenuation length of the metal induced gap states into $SrTiO_3$ which is governed by the lowest decay rate evanescent states of bulk $SrTiO_3$ which in turn can be found from the complex band structure of bulk $SrTiO_3$.

Magnetic properties of the 2DEG formed at the n-type interface of the $SrTiO_3/LaAlO_3$ superlattices are investigated. It is found that for a thin $SrTiO_3$ film the interface is ferromagnetic but for a thicker $SrTiO_3$ film the magnetic moment decreases and eventually disappears. This is a result of delocalization of the 2DEG that spreads over thicker $SrTiO_3$ film which leads to violation of the Stoner criterion. Further, it is

shown that inclusion of the Hubbard U interaction enhances the Stoner parameter and stabilizes the magnetism.

The effect of the 2DEG and the polar interfaces for the thin film ferroelectricity is investigated using both first principles and model calculations. Using a TiO_2-terminated $BaTiO_3$ film with LaO monolayers at the two interfaces it is shown that the intrinsic electric field produced by the polar interface forces ionic displacements in $BaTiO_3$ to produce the electric polarization directed into the interior of the $BaTiO_3$ layer. This creates a ferroelectric dead layer near the interfaces that is non-switchable and thus detrimental to ferroelectricity. It is found that the effect is stronger for a larger effective ionic charge at the interface and longer screening length due to a stronger intrinsic electric field that penetrates deeper into the ferroelectric.

Acknowledgements

First and foremost, I would like to thank Professor Evgeny Tsymbal for being the best advisor one can wish for. I was very impressed and influenced by his extensive scientific knowledge, ability to create excellent research ideas, and outstanding physical intuition. Evgeny, I would like to thank you for your strong and continuous academic guidance and support I received from you during my Ph. D. studies. I enjoyed the uplifting encouragement from you that made me believe that everything is in the range of my scientific capabilities. I greatly appreciate your help and understanding during the tough times in the Ph. D. pursuit.

I am indebted to Professor Julian Velev from University of Puerto Rico for his guidance in my research work and for collaborating with me on all projects presented in this thesis. I would like to thank you, Julian, for your patience when teaching me how to do *ab initio* calculations and for all scientific discussions we had.

I would like to express my appreciation to Professor Peter Dowben, Professor Sitaram Jaswal and Professor Xiao Zeng for serving on my Supervisory Committee. I would like to thank them for their careful reading of this dissertation. I would also like to thank Professor Peter Dowben and Professor Sitaram Jaswal for their continuous support during my Ph. D. studies.

I am very thankful to Dr. Yong Wang for many interesting discussion we had and that I could collaborate with him on the work presented in Chapter 7. In particular, I am

grateful to Yong for developing a phenomenological model to explain results of the first-principles calculations presented in this Chapter.

I would like to thank Professor J. D. Burton for help he provided to me during my studies and for collaborating with me on research projects that are not part of this dissertation.

I would like to thank Professor Manish Niranjan from Indian Institute of Technology Hyderabad for collaborating with me on work presented in Chapter 7 and for many interesting discussion we had.

Finally, I would like to thank all the friends, colleagues and my family for being there for me during my doctoral studies. Especially, I would like to thank my husband Alex and my son Karol for their constant love and support.

Dla Kokorka

Table of Contents

Chapter 1 Oxide materials and interfaces 1
1.1 Oxide materials 1
1.2 Interfaces between oxides 5
References 10
Chapter 2 Two-dimensional electron gases at oxide interfaces: Experimental results 11
2.1 Interface conductivity 11
2.2 Origin of the two-dimensional electron gas 17
2.3 Spatial extent of the two-dimensional electron gas 23
2.4 Electronic orderings of the two-dimensional electron gas 24
2.5 Conclusions 27
References 28
Chapter 3 Two-dimensional electron gases at oxide interfaces: Theoretical results ...30
3.1 Computational methodologies 31
3.2 Polar catastrophe model 34
3.3 Interface electronic structure 37
3.4 Confinement of the two-dimensional electron gas 38
3.5 Electronic ordering at the $SrTiO_3/LaAlO_3$ interface 40
3.6 The p-type interface 42
References 44
Chapter 4 Computational methodology 46
4.1 The Born Oppenheimer approximation 46
4.2 Density functional theory 49
4.3 Plane waves, pseudopotentials and projector augmented wave method 55
References 65
Chapter 5 Quantum nature of the two-dimensional electron gas confinement at the $SrTiO_3/LaAlO_3$ interface 66
5.1 Metal-induced gap states 66

5.2 Calculation methodology 70
5.3 Results 71
5.4 Conclusions 80
References 82
Chapter 6 Magnetism at the $SrTiO_3/LaAlO_3$ interface 84
6.1 Introduction 84
6.2 Stoner model 86
6.3 Calculation methodology 93
6.4 Results 94
6.5 Conclusions 99
References 100
Chapter 7 Effect of polar interfaces and two-dimensional electron gas on thin-film ferroelectricity. 102
7.1 Introduction 103
7.2 Computational methodology 106
7.3 Electronic structure 107
7.4 Atomic structure and polarization 112
7.5 Phenomenological model 117
7.6 Summary 123
Appendix 7A: Band alignment in $LaO/(BaTiO_3)_{21.5}$ system 124
Appendix 7B: Intrinsic and depolarizing fields 127
References 130
List of publications 136

List of Figures

Figure 1.1: The perovskite structure. The small B cation (black) is at the center of an octahedron of oxygen anions (gray). The large A cations (white) occupy the unit cell corners. 2

Figure 1.2: Spectacular properties of many oxides arise from the complex interactions between their charge, orbital, spin, and lattice degrees of freedom. These interactions can be modified at the interface by mechanisms of symmetry breaking, charge transfer, electrostatic coupling, frustration, and strain, leading to new behavior. The figure is adapted from Ref. [6]. 6

Figure 2.1: RHEED data and crystal structure of two types of $LaAlO_3/SrTiO_3$ interfaces prepared in Ref. [1]. (a) and (b) TiO_2/LaO n-type interface; (c) and (d) SrO/AlO_2 p-type interface. The figure adapted from Ref. [1]. 13

Figure 2.2: A schematic picture of polar catastrophe for both types of $SrTiO_3/LaAlO_3$ interfaces. (a) The unreconstructed n-type interface has neutral $SrTiO_3$ planes but $LaAlO_3$ planes have alternating net charges (ρ) producing non-negative electric field (E), leading in turn to divergence of electric potential (V) with $LaAlO_3$ thickness. (b) For the unreconstructed p-type interface the potential diverge negatively. (c) Polar catastrophe at the n-type interface can be removed by transfer of half a electron from $LaAlO_3$ surface to the interface. (d) Polar catastrophe at the p-type interface can be avoided by removing half an electron from the interfacial SrO plane in the form of oxygen vacancies. The figure is adapted from the Ref. [15]. 19

Figure 3.1: Schematic pictures of various geometries employed in first principles studies of $SrTiO_3/LaAlO_3$. The shaded green regions denote vacuum. Structures (a) and (c) represent nonstoichiometric symmetric superlattices for n- and p-type interface, respectively. Structures (b) and (d) represent stoichiometric slab with two surfaces and a single interface of n or p type, respectively. Structure (e) represents an asymmetric superlattice where both films are stoichiometric. Finally structure (f) represents the $LaAlO_3$ film embedded between two $SrTiO_3$ films whose other ends have free surfaces. The figure is adapted from Ref. [11]. 33

Figure 3.2: Schematic energy diagram for the n-type $SrTiO_3/LaAlO_3$ interface. We use the same color coding for atoms as in Fig. 3.1. The shaded areas are filled valence bands. The conductions bands are empty and their edges are denoted by the solid lines. The figure is adapted from Ref. [11]. 35

Figure 5.1: Schematic picture of the $(LaO)_1/(SrTiO_3)_{21}$ superlattice. Green, gray, red, and blue circles correspond to Sr, Ti, O, and La ions, respectively. 70

Figure 5.2: Layer-resolved DOS on the TiO_2 planes in $LaO/(SrTiO_3)_{23}$ superlattice (m = 1). Index l denotes the TiO_2 monolayer position away from the LaO monolayer placed at $l = 0$. Left panels show the DOS in the vicinity of the Fermi energy (E_F) denoted by the vertical line. The shaded areas indicate the occupied states forming 2DEG. The dashed line demonstrates the variation of the conduction band minimum (CBM) in $SrTiO_3$. Right panels show the DOS of the O-2s states at energies about 20eV below E_F. 73

Figure 5.3: Schematic band diagram of the $SrTiO_3/LaAlO_3$ interface and the illustration of the formation of the MIGS. Band bending (blue line) at the $SrTiO_3/LaAlO_3$ interface leads to the notched structure at the $SrTiO_3$ film close to the interface where CBM is below the Fermi level. This forms a classically allowed region where extra electrons from the $LaAlO_3$ film (dark blue circles) can reside. Due to quantum-mechanical tunneling these electrons can tunnel into classically forbidden region forming MIGS (red circles) that determine the confinement of the 2DEG. 75

Figure 5.4: Charge on Ti sites (solid symbols) for $(LaAlO_3)_m/(SrTiO_3)_{23}$ superlattices with m = 1 (squares), m = 3 (circles) and m =5 (triangles), and the conduction band minimum (open squares) as a function of distance from the interface z. The interfacial TiO_2 monolayer is placed at z = 0 as a reference. The Fermi energy (EF) is shown by a horizontal line and is related to the CBM plot only. 76

Figure 5.5: $k_{||}$-resolved charge density (a) and the lowest decay rate of the evanescent states in $SrTiO_3$ (b) within the two-dimensional Brillouin zone. The charge density is evaluated for the energy range from E_F – 1.0 eV to E_F. The decay rate (in units of $2\pi/a$) is evaluated for bulk $SrTiO_3$ at 0.2 eV below the CBM. 78

Figure 5.6: Band structure along Γ-M direction of the $LaO/(SrTiO_3)_{23}$ superlattice (*m* = 1). Close to the Γ point the dispersion of conducting bands is quadratic. 79

Figure 6.1: Example of a nonmagnetic DOS. Only occupied part (below Fermi level, ε_F) is shown. The figure is adapted from Ref. [9]. 88

Figure 6.2: Spin-splitting of DOS. Only occupied part (below Fermi level, ε_F) is shown. The figure is adapted from Ref. [9]. 89

Figure 6.3: Density of states for majority- and minority-spin electrons on the Ti atom at the interface for $(LaAlO_3)_3$/ $(SrTiO_3)_n$ superlattices. a) U=0, b) U=5 eV. The Fermi energy is denoted by the vertical solid line. 97

Figure 7.1: Density of states (DOS) projected onto the 3*d* states of Ti atoms located at the left and right interfaces (solid lines) and in the middle of the $BaTiO_3$ layer (shaded area) for (a) Vacuum/LaO/$(BaTiO_3)_{8.5}$/LaO, (b) LaO/$(BaTiO_3)_{8.5}$, and (c) $(SrRuO_3)_{5.5}$/LaO/$(BaTiO_3)_{8.5}$/LaO heterostructures. The Fermi level lies at zero energy and denoted by the dashed line. The insets show the valence band maximum (VBM) with respect to the Fermi energy within the $BaTiO_3$ layer as a function of *z*. 109

Figure 7.2: Schematic illustration of the charge distribution and the intrinsic electric field in a $BaTiO_3$ film terminated with positively charged $(LaO)^+$ monolayers at the left and right interfaces. A gradient shadow region indicates the screening charge penetrating into $BaTiO_3$. Blue arrows indicate the direction of the intrinsic electric field that has a tendency to pin the local polarization along the field direction. 111

Figure 7.3: Displacements (D) of cations (Ba and Ti) with respect to oxygen anions (a, b, c) and local polarizations (P) (d, e, f) across a $BaTiO_3$ layer in Vacuum/LaO/$(BaTiO_3)_8$/LaO (a, d), LaO/$(BaTiO_3)_{8.5}$ (b, e) and $(SrRuO_3)_{5.5}$/LaO/$(BaTiO_3)_{8.5}$/LaO (c, f) heterostructures. Solid squares and open circles in (a-c) denote Ba-O and Ti-O displacements respectively. In figures (d-f) the

local polarizations are obtained using the displacements calculated from first-principles in conjunctions with the Born effective charges (squares) and from the phenomenological model (solid lines). 114

Figure 7.4: Displacements (D) of cations (Ba and Ti) with respect to oxygen anions (a, b, c) and local polarizations (P) (d, e, f) across the $BaTiO_3$ layer in $LaO/(BaTiO_3)_n$ heterostructures containing n = 8.5 (a, d), 14.5 (b, e) or 21.5 (c, f) unit cells of $BaTiO_3$. Solid squares and open circles in (a-c) denote Ba-O and Ti-O displacements respectively. In figures (d-f) the local polarizations are obtained using the displacements calculated from first-principles in conjunctions with the Born effective charges (squares) and from the phenomenological model (solid lines). .. 116

Figure 7.5: Average polarization $\bar{P}$ of a $BaTiO_3$ film (a) as a function of the decay length λ for three film thicknesses t and (b) as a function of the film thickness t for two values of λ calculated within the phenomenological model (solid symbols) and using first-principles calculations and the Born charge model (open symbols). The inset in (a) shows $\bar{P}$ for $E_i = 0$. 121

Figure 7.6: Band alignment in $LaO/(BaTiO_3)_{21.5}$ system. (a) Local DOS on TiO_2 monolayers (l) as a function of the energy. The curved line to the left (right) indicates the position of the valence band maxima (conduction band minima) and the vertical solid line denotes the Fermi energy E_F; (b) Planar-averaged electrostatic potential across $BaTiO_3$ (thin line) and the macroscopic electrostatic potential (thick line); (c) Position of the core-like O-2s states for different TiO_2 layers (squares) and the macroscopic electrostatic potential shifted by -18.2 eV (solid line). 126

List of Tables

Table 2.1: Low-temperature values of sheet resistance R_S, sheet carrier density n_s, and Hall mobility μ_H found by different experimental groups from transport and Hall measurements of the n-type $LaAlO_3/SrTiO_3$ interface for different growth conditions. The table is adapted from Ref. [10]. 14

Table 6.1: Magnetic moments on the interface Ti atom (m_{Ti}), magnetization of the unit cell (m), the exchange splitting (ΔE), and the parameter $2N(\varepsilon_F)I$ entering the Stoner criterion (6.11) for $(LaAlO_3)_3/ (SrTiO_3)_n$ superlattices with different $SrTiO_3$ layer thickness (n) calculated within PBE (U =0). 95

Table 6.2: Magnetic moments on the interface Ti atom (m_{Ti}), magnetization of the unit cell (m), the exchange splitting (ΔE), and the parameter $2N(\varepsilon_F)I$ entering the Stoner criterion (6.11) for $(LaAlO_3)_3/ (SrTiO_3)_n$ superlattices with different $SrTiO_3$ layer thickness (n) calculated within PBE+U with U = 5 eV. 98

Chapter 1 Oxide materials and interfaces

1.1 Oxide materials

Oxide materials have long been known as hosts to an incredible variety of physical phenomena. Even the simplest binary monoxides exhibit broad range of properties ranging from insulating to metallic, magnetic, or even superconducting, depending on the type of the cation and the crystal structure. The more complex ternary or higher-order oxides show even more exotic properties like ferroelectricity, colossal magnetoresistance, or high-temperature superconductivity.

Such a broad spectrum of physical properties found in oxides results mainly from a unique balance between ionic and covalent bonding so that even subtle structural changes, like bond lengths or angles, have a profound effect on the interplay among the valence electrons and dramatically affect material properties. Furthermore, the properties are extremely sensitive to pressure or chemical doping offering many routes to control and engineer new functionalities in these systems making oxides very promising materials for industrial applications [1, 2].

Oxide materials often involve strongly correlated electrons for which the bandwidth is comparable to the on-site Coulomb interaction. These systems are very challenging from the theoretical point of view as they can neither be described by nearly free electron model, nor by a completely ionic model. They exhibit many exotic behaviors and often condense into variety of phases with separate ordering of their

charge, spin and orbital degrees of freedom. The different electronic phases compete with each other and are highly sensitive to external parameters such as electric and magnetic fields and temperature. Moreover different electronic degrees of freedom couple with each other or with the lattice, leading to remarkable and useful phenomena such as colossal magnetoresistance or magnetoelectric effect.

One family of oxide materials that has received enormous amount of attention consists of compounds with chemical formula ABO_3 and crystallizes in the perovskite structure, shown in Fig. 1.1. The perovskite is characterized by a small cation, B, at the center of an octahedron of oxygen anions, with large cations, A, at the unit cell corners.

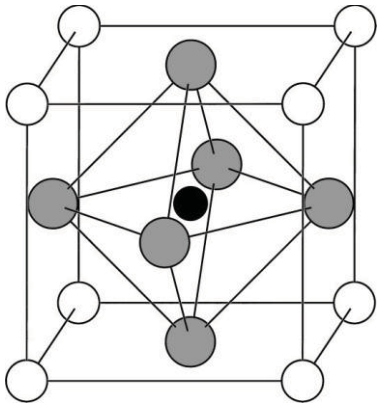

Figure 1.1: The perovskite structure. The small B cation (black) is at the center of an octahedron of oxygen anions (gray). The large A cations (white) occupy the unit cell corners.

The ideal cubic perovskite structure from Fig. 1.1 is stable only within a very limited range of ionic radii and undergoes different types of symmetry-lowering

distortions depending on the size of the A and B cations. The deviation from the ideal structure is often quantified through the Goldschmidt tolerance factor $t = (r_A + r_O)/\sqrt{2}(r_B + r_O)$ [3], which is equal to 1 when the ionic radii r_A, r_B and r_O are such that all the anions just touch the cations. For example, in $BaTiO_3$ the Ti^{4+} ions occupying sites B are too small for the oxygen octahedron (t >1) and prefer to move off-center, generating an electric dipoles and giving rise to ferroelectricity. On the other hand, when A cation is too small, as in $BiFeO_3$, then t < 1. In this case the oxygen octahedra are too large and they must tilt to fit into the cell. Such tilting has a profound effect on magnetic and transport properties of perovskite oxides as it leads to reduction of B–O–B angle which diminishes the orbital overlap and superexchange interaction.

In addition to ionic mismatch, the structural distortions in perovskite oxides can be also induced by orbitally degenerate electronic configuration that undergoes Jahn-Teller distortion as in the case for manganites (e.g. $LaMnO_3$).

An important example of a perovskite oxide is $SrTiO_3$. At room temperature it has a cubic structure as depicted in Fig. 1.1 with an experimental lattice constant of 3.905 Å. As temperature is decreased below 105 K it undergoes a phase transition to tetragonal structure driven by tilting neighboring oxygen octahedra in opposite directions.

$SrTiO_3$ has been thoroughly investigated during past decades and now high-quality single crystals of $SrTiO_3$ are freely available. The reason for the scientific interest in $SrTiO_3$ is that it is used as a standard substrate for depositing oxide materials. Indeed $SrTiO_3$ has a similar structure and lattice constant to many other important oxides

allowing for their epitaxial growth. In addition, it is chemically inert and usually it does not interact with deposited materials.

An important property of $SrTiO_3$ is that it can be grown on Si [4]. This provides a route to integrate oxide-based devices into microelectronic industry.

$SrTiO_3$ has many attractive properties by itself. In its stoichiometric form it is a paraelectric insulator with rather large indirect band gap of 3.25 eV but by introducing oxygen vacancies it can be doped to a metallic or even superconducting state. The concentration of oxygen vacancies can be carefully controlled in single crystals or even in thin films.

$SrTiO_3$ has also remarkable dielectric properties. It has a very large dielectric constant (several hundred at room temperature) making $SrTiO_3$ a good candidate for a gate in field effect transistors. Furthermore, $SrTiO_3$ can be driven into ferroelectric state by application of strain.

$LaAlO_3$ is another perovskite oxide, which is especially important for this thesis. It is a band insulator with a large band gap of 5.6 eV. At high temperatures it has a cubic perovskite structure. As temperature decreases below 813 K it undergoes a structural transition to rhomboedrally distorted perovskite structure driven by oxygen octahedral rotation. The rotation angle is however small and $LaAlO_3$ in the low-temperature rhomboedral phase can be described as pseudocubic with lattice constant of 3.791 Å. The reasonable lattice mismatch of 3% to $SrTiO_3$ allows the epitaxial growth of $LaAlO_3$ films on $SrTiO_3$.

1.2 Interfaces between oxides

While oxide materials exhibit a variety of remarkable and potentially useful phenomena already in the bulk form, perhaps even more exciting is the possibility of combining the properties of individual oxides into various heterostructures. Indeed, the introduction of interfaces in the semiconductor structures spawned discovery of many fascinating physical phenomena which led to invention of numerous semiconductor devices, like transistors, lasers or solar cells, that dominate the nowadays technology. Interestingly, in the bulk of the material, the behavior of conventional semiconductors like silicon is less exciting. Since oxide materials exhibit spectacular physics already in the bulk, we can expect that physical phenomena possible at oxide interfaces go well beyond those exhibited by interfaces between conventional semiconductors.

The physics of oxide interfaces is largely unexplored since the progress in this field was for many years thwarted by difficulties in growing epitaxial oxide multilayers [5]. This problem was recently overcome by development of new deposition techniques like molecular beam epitaxy (MBE) and pulsed laser deposition (PLD). These methods enable growth of high-quality oxide heterostructures with atomically sharp interfaces. They are grown layer by layer as can be monitored in situ by reflection high-energy electron diffraction (RHEED). Currently, it is possible to deposit thin films even one atomic layer thick.

The spectacular properties of oxide materials involve ordering and mutual interaction of different degrees of freedom like charge, spin, orbital and lattice. The presence of an interface can affect these degrees of freedom and may lead to new exciting

physical phenomena. We can distinguish five different mechanisms by which the interface affects the properties of oxides: symmetry breaking, charge transfer, strain, frustration and electrostatic coupling [6]. This is illustrated schematically in Fig. 1.2.

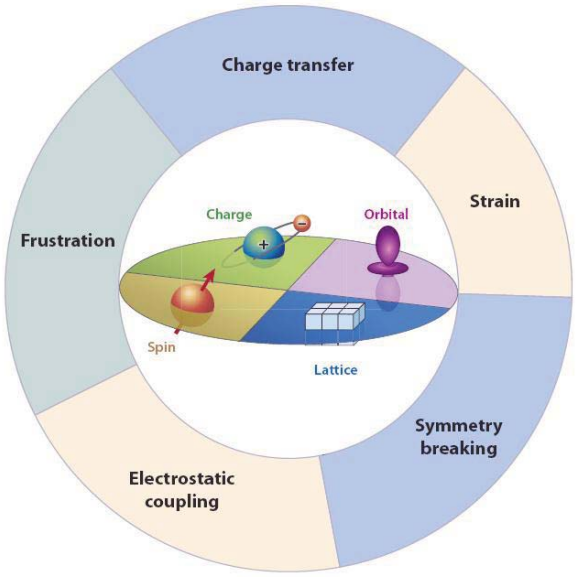

Figure 1.2: Spectacular properties of many oxides arise from the complex interactions between their charge, orbital, spin, and lattice degrees of freedom. These interactions can be modified at the interface by mechanisms of symmetry breaking, charge transfer, electrostatic coupling, frustration, and strain, leading to new behavior. The figure is adapted from Ref. [6].

When we create an interface between two oxides, we break the translational symmetry of both materials. This modifies electronic states at the interface altering the

hybridization of the ionic orbitals which in turn modifies electronic orderings. Furthermore, new states can be formed within band gaps that are localized close to the interface. These interface states are direct consequence of translational symmetry breaking that invalidates the Bloch theorem and don't require change of the charge density. The interface states can pin the position of the Fermi level determining transport properties and charge transport across the interface.

Similarly, as in the case of surface, the atoms at the interface can undergo reconstruction further breaking the symmetry of the constituent bulk oxides. In perovskites for example, the presence of interface can induce rotation of oxygen octahedra in the ideal cubic structure of the bulk oxide which can change its conducting and magnetic properties as well as the ferroelectric order.

When two oxides are stacked together creating an interface, there is always charge transfer between them in order to equalize electronic chemical potentials of both materials. This phenomenon is mainly responsible for rich physics in conventional semiconductor heterostructures that led to devices like p-n junction, Schottky diodes, or high-mobility transistors based on two-dimensional electron gas (2DEG). The same effects exist at the oxide interfaces. In particular, high mobility 2DEG was reported at high-quality ZnO-$Mg_xZn_{1-x}O$ interface that allows observation of the quantum Hall effect (QHE) [7]. While ZnO is not particularly interesting oxide, it suggests possibility of 2DEG at the interface between oxides with different types of electronic orders, like magnetism or superconductivity that could interact with QHE [6].

Recently, 2DEG was observed at the interface between two band insulators $SrTiO_3$ and $LaAlO_3$ [8]. While the origin of this 2DEG is not fully understood yet, it is clear that the mechanism is quite different than in the case of semiconductor heterostructures. This system will be discussed in depth in subsequent chapters.

The charge transfer at the oxide interfaces leads to effective doping of the space-charge region. The filling or emptying electronic states at the interface strongly affects interaction between electronic degrees of freedom. For example, in the case of interface between two insulating antiferromagnets $LaMnO_3$ and $SrMnO_3$ the charge transfer leads to the interface ferromagnetism [9].

Lattice mismatch between substrate and deposited material leads to the biaxial strain. The strain changes the distance between the ions in the oxide thin film altering the orbital overlap and hence affecting electronic and lattice degrees of freedom. For example, $SrTiO_3$ becomes ferroelectric under strain and multiferroicity can be induced by epitaxial strain in $EuTiO_3$ [10]. By choosing different substrate the magnitude and the sign of epitaxial strain can be altered providing a powerful tool for tuning the properties of oxides and stabilizing alternative orderings.

Particularly interesting effects can arise at the interface between oxides with electronic or lattice orderings which cannot coexist, i.e., there is a frustration at the interface. In an attempt to reduce frustration materials often undergoes dramatic changes that lead to new phases that are absent in the bulk of both constituents. For example, at the interface between ferromagnetic $La_{0.6}Sr_{0.4}MnO_3$ (LSMO) and antiferromagnetic $La_{0.6}Sr_{04}FeO_3$ spin frustration leads to the canting of spins and a reduction of overall

magnetic moment. As both ferromagnetism and conductivity in LSMO are mediated by electron hopping, the conductivity of LSMO is also reduced due to interfacial effect. Application of magnetic field restores ferromagnetic alignment and increases conductivity leading to large magnetoresistance [11].

At the interface where one or both oxides are ferroelectric, the electrostatic boundary conditions must be satisfied leading to an electrostatic coupling between the layers. For example, in the case of $BaTiO_3/SrTiO_3$ superlattices grown on $SrTiO_3$ substrate $BaTiO_3$ is under compressive strain that induces out-of-plane electric polarization. Since $SrTiO_3$ is not under strain, one could expect that it remains paraelectric as in the bulk. However, the condition for continuity of the electric displacement across the interfaces means that any polarization mismatch between the layers would give rise to depolarizing field with a large energy cost. The structure thus adopts uniformly polarized state with the polarization value determined by the competition between the energy cost of polarizing the paraelectric $SrTiO_3$ layers and the energy gain in preserving the polarization in $BaTiO_3$ layers.

References

[1] Y. Tokura and H. Y. Hwang, Nature Mater. **7**, 694 (2008).

[2] J. Heber, Nature **459**, 28 (2009).

[3] A. S. Bhalla, R. Guo, and R. Roy, Mat. Res. Innovat. 4, 3 (2000).

[4] L. V. Goncharova *et al.*, J. Appl. Phys. **100**, 014912 (2006).

[5] J. Manhart and D. G. Schlom, Science **327**, 1607 (2010).

[6] P. Zubko, *et al.*, Annu. Rev. Condens. Matter Phys. **2**, 141 (2011).

[7] A. Tsukazaki, *et al.*, Nat. Mater. **9**, 889 (2010).

[8] A. Ohtomo and H. Hwang, Nature **427**, 423 (2004).

[9] N. Ogawa *et al.*, Phys. Rev. B **78**, 212409 (2008).

[10] J. H. Lee *et al.*, Nature **466**, 954 (2010).

[11] M. Izumi, *et al.*, Mater. Sci, Eng. B **84**, 53 (2001).

Chapter 2 Two-dimensional electron gases at oxide interfaces: Experimental results

Number of remarkable phenomena arises at the interfaces between various oxide materials. A spectacular example is the existence of two-dimensional electron gas (2DEG) at the interface between insulating perovskite oxides $LaAlO_3$ and $SrTiO_3$ [1]. The interface conductivity can be controlled by external electric field [2] making this system promising for the development of novel applications in nanoscale oxide electronics. In addition low-temperature superconductivity [3] and signatures of magnetic order [4] at the $LaAlO_3/SrTiO_3$ interface have been reported. In this chapter I will review experimental results for the $LaAlO_3/SrTiO_3$ interface.

2.1 Interface conductivity

In their seminal 2004 paper, Ohtomo and Hwang reported the epitaxial (001) oriented growth of $LaAlO_3$ film on the $SrTiO_3$ substrate using pulsed laser deposition (PLD) [1]. As shown in Fig. 2.1b and d, there are two possible types of interfaces. The first has the atomic planes TiO_2/LaO at the interface and is referred to as the n-type interface. The second is formed by adjacent SrO/AlO_2 planes and is called the p-type interface. Since techniques were developed to prepare TiO_2-terminated surface of $SrTiO_3$ single crystal with atomically flat terraces [5], the n-type interface was obtained by direct deposition of $LaAlO_3$ on such surface. The p-type interface, on the other hand, was obtained by first

depositing single monolayer of SrO and then switching to $LaAlO_3$. Results of reflection high energy electron diffraction (RHEED) measurements for both types of interfaces are shown in Fig. 2.1a and c [1]. RHEED data shows layer by layer growth indicating high-quality atomically abrupt interfaces.

Conductance of both types of $SrTiO_3/LaAlO_3$ interfaces was measured using laser annealed ohmic contacts to reach the interface [1]. While p-type interface was insulating, the n-type interface was found to be metallic [1]. In addition, Hall measurements have shown that the current is carried by electrons indicating presence of 2DEG at the interface [1].

The existence of 2DEG at the n-type $SrTiO_3/LaAlO_3$ interface was independent of growth method although the values of sheet resistance, as well as electron mobility and carrier density, as found from Hall measurements, were dependent on annealing conditions and especially on oxygen partial pressure during the growth [1] (see Table 2.1). In particular, for low oxygen pressure very large carrier density and low-temperature mobility were observed with values exceeding 10^{17} cm^{-2} and 10^4 $cm^2V^{-1}s^{-1}$, respectively [1].

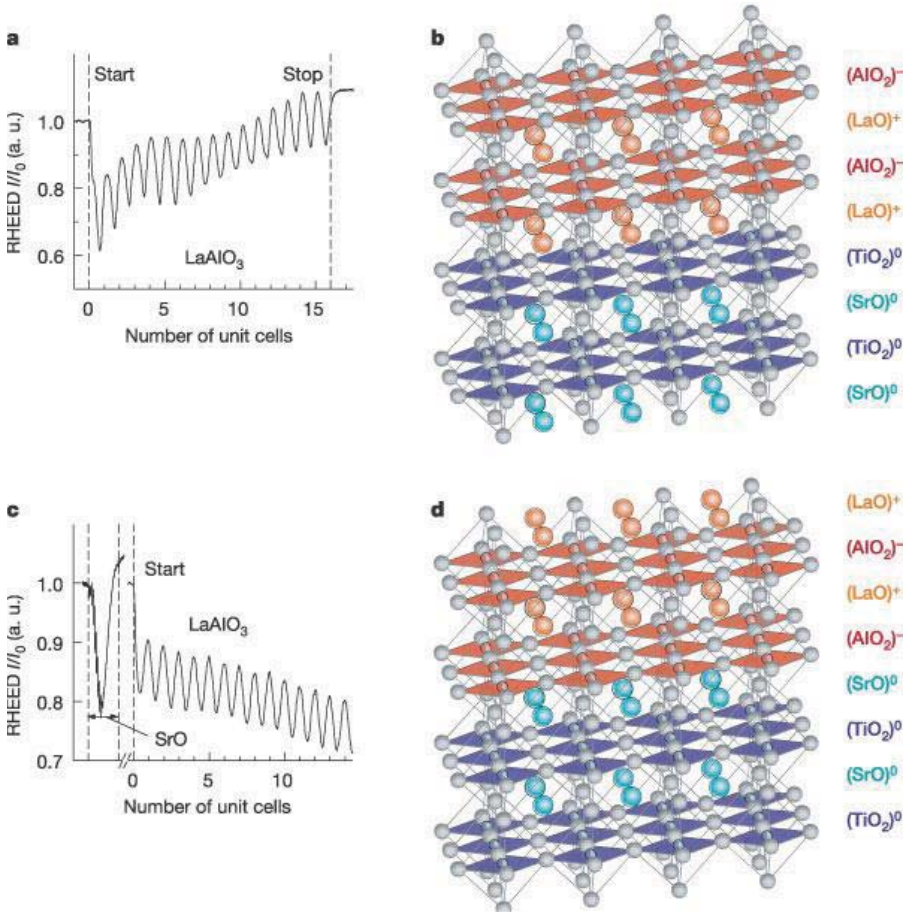

Figure 2.1: RHEED data and crystal structure of two types of $LaAlO_3/SrTiO_3$ interfaces prepared in Ref. [1]. (a) and (b) TiO_2/LaO n-type interface; (c) and (d) SrO/AlO_2 p-type interface. The figure adapted from Ref. [1].

The fact that interface between two insulators is conducting was a remarkable finding and sparked a great interest in this system. The $SrTiO_3/LaAlO_3$ interface was grown in a similar manner by many other experimental groups [2, 5-9] and in most cases the presence of 2DEG at the n-type interface was confirmed. The reported sheet resistance R_S, Hall conductivity μ_H and charge density n_S for different growth conditions are

compiled in Table 2.1 [10]. For low oxygen partial pressure (~10^{-6} mbar) without annealing it appears that existing experiments converge to the following values: $R_S \sim 10^{-2}\Omega/\square$, $n_S \sim 10^{16} - 10^{17}$ cm^{-2} and $\mu_H \sim 10^4$ $cm^2V^{-1}s^{-1}$. Some discrepancies exist when samples are post-annealed in oxygen. Ohtomo and Hwang [1] didn't find any significant change in the transport properties before and after annealing, whereas Kalabukhov *et al.* [7] and Basletic *et al.* [9] grew samples under similar conditions but observed an increase in R_S and decrease in μ_H and n_S after annealing (see Table 2.1).

For samples grown at high oxygen partial pressure (~ 10^{-4} mbar) different groups find similar carrier density in the range of $10^{13} - 10^{14}$ cm^{-2}. Disagreement however exists in case of sheet resistance and mobility. At low temperatures Ohtomo *et al.* [1] and Herranz *et al.* [6] found $R_S \sim 10^4\,\Omega/\square$, and $\mu_H \sim 10$ $cm^2V^{-1}s^{-1}$ while Kalabukhov *et al.* [7] and Thiel *et al.* [2] report R_S and μ_H values two order of magnitude smaller and larger, respectively. Finally samples grown at very high oxygen partial pressure (> 10^{-2} mbar) [7] or samples annealed at high oxygen partial pressure [7] have been observed to be completely insulating.

Thiel et al. [2] observed that for samples grown under relatively high oxygen partial pressure the interface is not conducting unless the thickness of $LaAlO_3$ film exceeds a critical value of four unit cells. For $LaAlO_3$ films thicker than four unit cells the sheet carrier density undergoes a step-like jump and remains of the order of 10^{13} cm^{-2} even after prolonged annealing in the presence of oxygen partial pressure [2].

Table 2.1: Low-temperature values of sheet resistance R_S, sheet carrier density n_s, and Hall mobility μ_H found by different experimental groups from transport and Hall measurements of the n-type $LaAlO_3/SrTiO_3$ interface for different growth conditions. The table is adapted from Ref. [10].

p_{O2} [mbar]	Annealing conditions	R_S [Ω/□]	n_S [cm^{-2}]	μ_H [$cm^2V^{-1}s^{-1}$]	Ref.
10^{-6}	not annealed	10^{-2}	10^{17}	10^4	[1]
10^{-6}	annealed in 1atm of O_2 at 400°C for 2 h	10^{-2}	$2\cdot10^{16}$	10^4	[1]
10^{-6}	not annealed	10^{-2}	$5\cdot10^{16}$	10^4	[7]
10^{-6}	annealed at 500 mbar during cooling	10^3	10^{13}	10^3	[7]
10^{-6}	annealed at 300 mbar during cooling	10^2	$3\cdot10^{13}$	$7\cdot10^2$	[9]
10^{-6}	not annealed	$3\cdot10^{-3}$		10^4	[6]
10^{-6}	not annealed		$2\cdot10^{16}$	10^4	[8]
10^{-5}	not annealed	10^2	10^{16}	1	[1]
10^{-5}	not annealed	10^{-3}	$5\cdot10^{17}$	$2\cdot10^3$	[9]
$2\cdot10^{-5}$	cooled at high oxidation		$2\cdot10^{13}$	$3\cdot10^2$	[8]
10^{-4}	not annealed	10^4	10^{14}	10	[1]

10^{-4}	not annealed	10^{2}	10^{13}	10^{3}	[7]
10^{-4}	annealed at 500 mbar during cooling	10^{2}	10^{13}	10^{3}	[7]
10^{-4}	not annealed	$3 \cdot 10^{-3}$		10	[6]
$5 \cdot 10^{-2}$	not annealed	insulating	insulating	insulating	[7]
$10^{-6} – 10^{-3}$	annealed at 300 mbar during cooling	insulating	insulating	insulating	[6]

Sheet carrier density at the n-type interface was also measured with hard X-ray photoelectron spectroscopy [11] and later with resonant inelastic X-ray scattering [12] for the samples grown at the same conditions as in Ref. [2]. In contrast to results from Hall measurements [2] they found that sheet carrier density is already nonzero for $LaAlO_3$ thickness of two unit cells [11, 12]. The authors suggested that the finite sheet carrier density for two unit cells thick $LaAlO_3$ films is immobile and doesn't contribute to transport [11, 12].

The above results were obtained for thin film $LaAlO_3$ grown on $SrTiO_3$ substrate creating a $SrTiO_3/LaAlO_3$ interface and $LaAlO_3$ surface. Other variants are also possible. For example, an additional capping layer can be grown on top of $LaAlO_3$. In particular, Huijben *et al.* [13] grew $LaAlO_3$ film on TiO_2-terminated $SrTiO_3$ surface creating TiO_2/LaO interface and then capping layer of $SrTiO_3$ on $LaAlO_3$ creating AlO_2/SrO interface. The resulting herterostructure contained both n-type and p-type interfaces. In agreement with measurements for systems with a single interface the p-type interface was

found to be insulating and the n-type interface was metallic [13]. Interestingly the n-type interface is conducting for all $LaAlO_3$ thicknesses studied: carrier density starts out small but finite for one unit cell of $LaAlO_3$ and increases with $LaAlO_3$ thickness until it saturates at ~ 10^{14} cm^{-2} for $LaAlO_3$ films thicker than 6 unit cells [13].

2.2 Origin of the two-dimensional electron gas

One of the key questions that remain to be answered is the origin of conductivity at the n-type $SrTiO_3/LaAlO_3$ interface. To date, at least three different mechanisms have been proposed.

In their original paper Ohtomo and Hwang [1] proposed a polar catastrophe model in which 2DEG arises due to intrinsic electronic reconstruction [1, 14-15]. This mechanism can be understood in the following simplified picture. The structure of ABO_3 perovskites can be viewed as a stacking of alternating layers of AO and BO_2 planes in the (001) direction. In the simple ionic limit oxygen has a formal valence of O^{2-} while the valences of A and B cations can take different values as long as charge neutrality is satisfied. In case of $SrTiO_3$ we have $A^{2+}B^{4+}$ so that SrO and TiO_2 planes are neutral. On the other hand, for $LaAlO_3$ cations valences are $A^{3+}B^{3+}$ making LaO and AlO_2 planes to have net charges of +1e and –1e, respectively.

If we place a stoichiometric $LaAlO_3$ film on top of $SrTiO_3$ substrate the polar discontinuity results at the interface. Electrostatically the system is equivalent to a chain of capacitors in series. The potential across each capacitor is additive and diverges with

number of capacitors (i.e. the thickness of $LaAlO_3$ film) leading to a polar catastrophe. This scenario is shown schematically in Fig. 2.2a and b for both n-type TiO_2/LaO and p-type SrO/AlO_2 interfaces.

Such a polar catastrophe has been encountered before for semiconductor heterostructures [16]. In those cases, the interface undergoes a considerable atomic reconstruction that changes the interface stoichiometry and removes the divergence of the electrostatic potential.

The divergence of electrostatic potential can be also removed by purely electronic means if half an electron (hole) is transferred from the $LaAlO_3$ surface to the n-type TiO_2/LaO (p-type SrO/AlO_2) interface [1, 14-15]. As shown in Fig. 2.2c, for the n-type interface this process produces an interface dipole that causes electric field to oscillate around zero and the potential remains finite. Ohtomo and Hwang [1] argued that for the n-type TiO_2/LaO such electronic reconstruction has a lower energy barrier and/or ground state energy than the typical atomic reconstruction due to multivalent nature of Ti cations, which can exist as either Ti^{3+} or Ti^{4+} and thus Ti atoms at the interface can accommodate extra electrons transferred from $LaAlO_3$. As a result of this charge transfer we have free carriers at the interface that form a 2DEG and are responsible for conductivity.

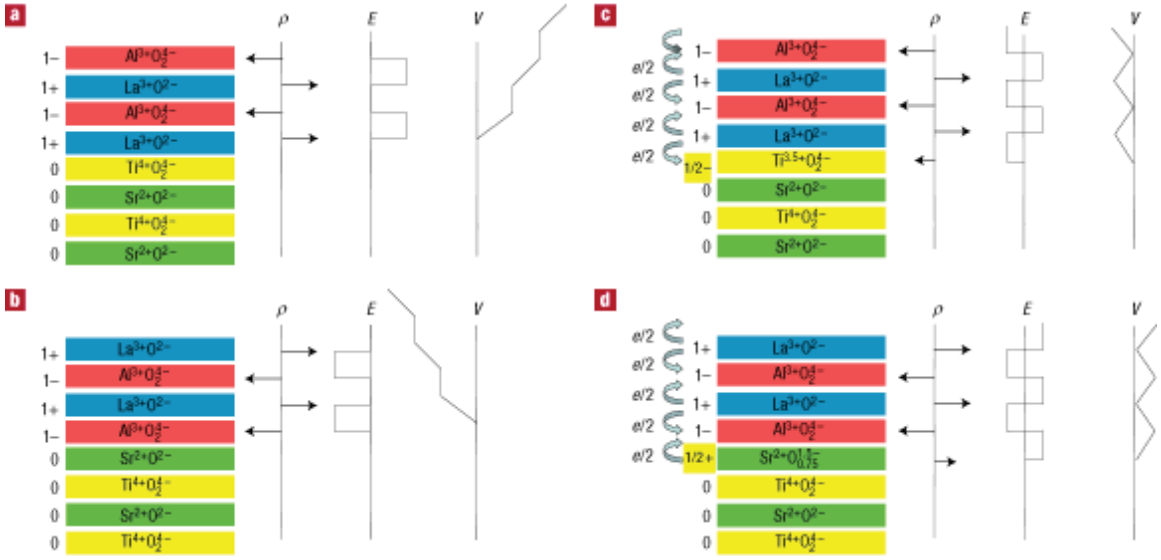

Figure 2.2: A schematic picture of polar catastrophe for both types of $SrTiO_3/LaAlO_3$ interfaces. (a) The unreconstructed n-type interface has neutral $SrTiO_3$ planes but $LaAlO_3$ planes have alternating net charges (ρ) producing non-negative electric field (E), leading in turn to divergence of electric potential (V) with $LaAlO_3$ thickness. (b) For the unreconstructed p-type interface the potential diverge negatively. (c) Polar catastrophe at the n-type interface can be removed by transfer of half a electron from $LaAlO_3$ surface to the interface. (d) Polar catastrophe at the p-type interface can be avoided by removing half an electron from the interfacial SrO plane in the form of oxygen vacancies. The figure is adapted from the Ref. [15].

For the p-type SrO/AlO_2 interface the polar catastrophe mechanism requires transfer of positive charge to the interface. Since in this case there are no mixed-valence states to accommodate for the half a hole, it is plausible that, similarly to semiconductor interfaces with polar discontinuity, the electronic reconstruction has a higher energy barrier and/or

ground state energy than the atomic reconstruction [15]. Indeed, the transport measurements showed that the p-type interface is insulating [1].

Nagakawa *et al.* [15] argued that the atomic reconstruction at the p-type interface has a form of high density oxygen vacancies. As shown in Fig. 2.2d, the concentration of 0.25 oxygen vacancies per lateral unit cell at the p-type interface would remove the polar catastrophe. This hypothesis was supported by atomic-resolution electron energy loss spectroscopy (EELS) studies that found the presence of 0.32 oxygen vacancies per two-dimensional unit cell in the $SrTiO_3$ near the SrO/AlO_2 interface while in the case of the n-type interface they found the value three times smaller [15].

It was proposed that the 2DEG at the n-type $SrTiO_3/LaAlO_3$ interface is caused by the presence of oxygen vacancies [6-8] rather than by polar catastrophe mechanism. Indeed, oxygen vacancies are the most common type of defect in oxides and are often created in large concentration when surfaces are cleaned or during the growth, especially in low oxygen partial pressures. Oxygen vacancies act as electron donors and can cause metallic behavior even in bulk $SrTiO_3$. The importance of oxygen vacancies in the creation of 2DEG at the n-type $SrTiO_3/LaAlO_3$ interface was recently emphasized by observation of 2DEG with very similar properties at the surface of $SrTiO_3$ [17] where the oxygen vacancies are the only possible source of free carriers.

Undoubtedly, oxygen vacancies play an important role in the electronic properties of the n-type $SrTiO_3/LaAlO_3$ interface. This can be seen from Table 2.1 which shows the strong dependence of the interface transport properties on oxygen partial pressure and annealing conditions, the parameters that control the concentration of oxygen vacancies.

Nevertheless, many experiments observed 2DEG even for samples grown under high oxygen partial pressure and/or post-annealing in oxygen [2, 8, 15]. For such samples the number of oxygen vacancies should be strongly suppressed, as explicitly seen from atomic scale EELS data that indicated only small concentration of oxygen vacancies at the n-type interface [15].

This suggests that oxygen vacancies are not the source of the interface conductivity and that the polar catastrophe mechanism is dominant in the formation of 2DEG. In fact, the polar catastrophe model is supported by a number of experiments. As discussed above, this model implies that Ti cations with valence Ti^{3+} exist at the n-type interface. Atomic scale EELS studies found a significant concentration of Ti^{3+} ions in $SrTiO_3$ close to the n-type interface [15]. In addition, the existence of the critical thickness for formation of 2DEG [2] naturally follows from the polar catastrophe model. The electronic reconstruction occurs when the energy cost for the charge transfer is smaller than the electrostatic energy of the effective capacitor series. For small $LaAlO_3$thicknesses the electrostatic energy is smaller and no charge transfer occur leading to the insulating interface. As we increase the $LaAlO_3$ thickness, the electrostatic energy increases and at certain point (critical thickness) it overcomes the energy cost for electronic reconstruction leading to charge transfer to the interface and formation of 2DEG.

While most of researchers seem to reach a consensus that both oxygen vacancies and polar catastrophe contribute to the formation of 2DEG at the n-type $SrTiO_3/LaAlO_3$ interface, there are some problems with that picture. First, for samples above critical

thickness grown at high oxygen pressure and/or post-annealed in oxygen, the sheet carrier density found from Hall measurements is order of magnitude smaller than the value predicted from polar catastrophe mechanism, $n_s = 0.5/a_{STO}^2 \sim 3.3 \cdot 10^{14}$ cm^{-2}. Possible explanation is that some carriers are immobile and don't contribute to transport [11-12].

Second, it was found that for samples grown at very high oxygen pressure and/or annealed in oxygen the n-type interface can become completely insulating [6-7]. This observation poses a great puzzle since it seems to contradict the polar catastrophe model. On the other hand, the abrupt jump in sheet carrier density at the critical thickness of $LaAlO_3$ [2] is difficult to explain using oxygen vacancies alone. Perhaps, apart from removing the oxygen vacancies, the heavy oxidation has other side effect. For example, it may introduce additional oxygen atoms at the $LaAlO_3$ surface that diffuse into the body of the material enhancing disorder and/or intermixing and make $LaAlO_3$ nonpolar.

Yet another mechanism for creation of 2DEG at the n-type $SrTiO_3/LaAlO_3$ interface is the cation intermixing. Using atomic scale EELS [15] and SXRD [18-19] substantial intermixing of cations Sr and La across the n-type interface has been observed. On the other hand, for the p-type interface the intermixing was significantly smaller. As the ionic radii of La and Sr are more than twice as large as those of Al and Ti, the observation of the La-Sr intermixing reflects the natural tendency of the system rather than an effect due to kinetic disruption during the growth. Indeed, such intermixing reduces the dipole energy at the interface so it is energetically favorable [15, 18].

As a consequence of Sr-La intermixing $La_{1-x}Sr_xTiO_3$ forms at the interface. This alloy is metallic for wide range of concentration $0.05 < x < 0.95$ which could explain the interface conductivity [18]. However, this mechanism cannot explain the critical thickness of $LaAlO_3$ above which the interface becomes conducting.

2.3 Spatial extent of the two-dimensional electron gas

One of the important characteristics of the 2DEG formed at the n-type $SrTiO_3/LaAlO_3$ interface is its spatial extent. Information about the spatial extent of the 2DEG is not accessible from typical transport experiments for this system that use contacts through the sample [1] and thus measure the total current but not the current distribution across $SrTiO_3$.

Siemons *et al.* [8] solved the Poisson equation for the interface system assuming a Thomas-Fermi distribution of carriers. They found that the electrons extend into $SrTiO_3$ over 50 nm at low temperatures but the confinement length decreases dramatically at high temperatures [8].

Using sample grown at low oxygen pressure (10^{-6} mbar) and without annealing Herranz *et al.* [6] reported low temperature Shubnikov – de Haas oscillations in magnetoresistance for magnetic field both perpendicular and parallel to the interface. They found that the period of oscillation is the same for both cases which indicates a three-dimensional character of the conduction electron gas and thus a large spatial extent of 2DEG [6].

The direct measurement of the 2DEG width at the n-type interface grown at different conditions was obtained using a conducting-tip atomic force microscope (CT-AFM) in cross-section geometry [9]. For samples prepared at low oxygen partial pressure (10^{-6} mbar) and not subjected to further annealing it was found that the electron gas extends up to hundreds of μm into the $SrTiO_3$ and thus has a three-dimensional character [9]. In this case the electron carriers originate most likely from extrinsic dopants such as oxygen vacancies. On the other hand, for samples grown and/or annealed at high oxygen partial pressure (10^{-4} mbar), the electron gas was found to be localized within few nanometers from the interface [9].

The two-dimensional character of the electron gas for samples grown and/or annealed at high oxygen partial pressure was confirmed by observation of two-dimensional superconductivity at the n-type interface with the spatial extent of about 10 nm [3] and by hard X-Ray photoelectron spectroscopy measurements [11].

2.4 Electronic orderings of the two-dimensional electron gas

According to the polar catastrophe model, the electrons are donated to the n-type $SrTiO_3/LaAlO_3$ interface and occupy empty Ti 3d states. Due to the localized nature of the Ti 3d states the Coulomb interaction between these electrons is very important and may lead to different electronic orderings.

The simplest example is magnetic ordering. In this case electrons can lower their Coulomb interaction energy by occupying states with the same spin direction since,

according to the Pauli exclusion principle, this increases their separation. The idea of ferromagnetism in the 2DEG formed at the n-type $SrTiO_3/LaAlO_3$ interface is attractive from the point of view of applied physics as it would open the possibilities to create spintronic devices based on this system.

Experimental indications of magnetism of the 2DEG formed at the n-type $SrTiO_3/LaAlO_3$ interface were first provided by Brinkman *et al.* [4]. Using samples grown at relatively high oxygen partial pressure, they observed a minimum in the sheet resistance with lowering of the temperature [4]. Since such a minimum is reminiscent of the Kondo effect that stems from the scattering of the itinerant electrons from a localized magnetic moment, they postulated that localized magnetic moments exist at the interface and are formed by the Ti^{3+} ions [4]. This interpretation is consistent with the observed negative isotropic magnetoresistance [4] which can also be explained by scattering from the localized magnetic moments. Furthermore, the magnetoresistance at 300 mK was found to exhibit a hysteretic behavior suggesting the presence of ferromagnetic domains [4].

Very interesting results have been reported by Zalk *et al.* [20]. They investigated samples grown under similar conditions to those used by Brinkman *et al.* [4]. They found low-temperature magnetoresistance oscillations versus external magnetic field intensity, B. Surprisingly, the oscillations were periodic in $\sqrt{B}$ instead of the standard Shubnikov-de Haas 1/B periodicity [20]. The authors suggested that this comes from the commensurability condition of the edge states. They also speculated that the

magnetoresistance oscillations are related to the ferromagnetic ordering, and that the quantum Hall effect might be present.

In contrast to Ref. [4], in Reyren *et al.* [3] positive magnetoresistance was reported with no minimum in the sheet resistance, and no hysteresis in magnetoresistance. Instead, they reported that the 2DEG becomes superconducting at low temperatures [3]. In their studies the thickness of $LaAlO_3$ film was smaller than in Ref. [4] and the samples were grown under lower oxygen partial pressure ($< 10^{-5}$) although they annealed the samples afterwards which should eliminate most of oxygen vacancies. Nevertheless, these differences could affect the sheet carrier density and mobility that could in turn affect the stability of magnetic phase.

Yet different results have been reported by Shalom *et al.* [21]. They studied samples grown under rather low oxygen partial pressure $10^{-4} – 10^{-5}$ mbar. In agreement with Ref. [3], Shalom and coworkers observed superconductivity below 130 mK. At higher temperatures, they found highly anisotropic magnetoresistance that has different signs for fields parallel and perpendicular to the interface. No hysteresis down to the superconducting transition temperature was, however, found. The authors proposed that the system is antiferromagnetic with the Néel temperature about 35 K [21].

The experiments seem to indicate that different magnetic orders compete with each other and with superconductivity at the interface. This may suggest that the superconducting pairing interaction may be mediated by spin fluctuations. Clearly more experiments are needed to confirm this picture.

2.5 Conclusions

Since the discovery of the 2DEG at the n-type $SrTiO_3/LaTiO_3$ interface in 2004 by Ohtomo and Hwang [1], a lot of experimental data have been collected for this system. Growth conditions, such as oxygen partial pressure and annealing temperature, have been identified as the major factor that controls the electronic properties of the 2DEG.

The experimental situation is, however, far from being clear. Even the origin of the 2DEG is not well understood. The polar catastrophe mechanism seems to play an important role in the formation of the 2DEG at the n-type interface. However, the relative contribution of other factors, such as oxygen vacancies and intermixing at the interface, is still under debate. At the same time there seems to be a consensus that the insulating behavior of the p-type interface is due to the oxygen vacancies formed at this interface.

The presence of magnetism at the interface remains a controversial issue and more experiments are needed to clarify the picture. Furthermore, the mechanism of the observed two-dimensional superconductivity is not understood.

References

[1] A. Ohtomo and H. Y. Hwang, Nature **427**, 423 (2004).

[2] S. Thiel, *et al.*, Science **313**, 1942 (2006).

[3] N. Reyren, *et al.*, Science **317**, 1196 (2007).

[4] A. Brinkman, *et al.*, Nature Mater. **6**, 493 (2007).

[5] M. Kawasaki, *et al.*, Science **266**, 1540 (1994).

[6] G. Herranz, *et al.*, Phys. Rev. Lett. **98**, 216803 (2007).

[7] A. Kalabukhov, *et al.*, Phys. Rev. B **75**, 121404(R) (2007).

[8] W. Siemons, *et al.*, Phys. Rev. Lett. **98**, 196802 (2007).

[9] M. Basletic, *et al.*, Nature Mater. **7**, 621 (2008).

[10] H. Chen, A. M. Kolpak, and S. Ismail-Beigi, Adv. Mater. **22**, 2881 (2010).

[11] M. Sing *et al.*, Phys. Rev. Lett. **102**, 176805 (2009).

[12] G. Berner *et al.*, Phys. Rev. B **82**, 241405(R) (2010).

[13] M. Huijben *et al.*, Nature Mater. **5**, 556 (2006).

[14] H. Y. Hwang, Science **313**, 1895 (2006).

[15] N. Nagakawa, *al.*, Nature Mater. **6**, 493 (2007).

[16] W. A. Harrison *et al.*, Phys. Rev. B **18**, 4402 (1978).

[17] A. F. Santander-Syro, *et al.*, Nature **469**, 189 (2011).

[18] P. R. Willmott *et al.*, Phys. Rev. Lett. **99**, 155502 (2007).

[19] S. A. Pauli *et al.*, Phys. Rev. Lett. **106**, 036101 (2011).

[20] M. van Zalk *et al.*, arXiv.org0806.4450 (2008).

[21] M. Ben Shalom *et al.* Phys. Rev. B **80**, 140403 (2009).

Chapter 3 Two-dimensional electron gases at oxide interfaces: Theoretical results

In this chapter I will review the theoretical work on the $SrTiO_3/LaAlO_3$ interface system. Although some interesting results have been obtained using the model Hamiltonian approach [1], I will focus solely on *ab initio* calculations. *Ab initio* or first principles calculations allow for parameter-free description of the system which can be directly compared with experiment. In fact, this technique can be treated as a numerical experiment where, unlike in real experiments, one has an ability to turn on or off certain effects like for example ionic relaxation, oxygen vacancies, or electronic correlations. This is a great advantage since it allows understanding physical mechanisms responsible for system behavior. On the other hand, it is often very difficult to include all complexity of the system using first principles methods. In particular, an accurate description of disorder or strong electronic correlations is very expensive and for large systems serious approximations must be made that must be kept in mind when interpreting results of *ab initio* calculations.

3.1 Computational methodologies

First principles studies of the $SrTiO_3/LaAlO_3$ interface have considered mostly an idealized system without any imperfections such as oxygen vacancies or cation intermixtures. This allows studying intrinsic properties of the material which are not hindered by extrinsic defects. It should be however noted that this choice is dictated by practical reasons since inclusions of imperfections is computationally very expensive. Nevertheless, oxygen vacancies and interface intermixing were investigated by several authors [2-6].

Most works employed density functional theory (DFT) within the local density approximation (LDA) or the generalized gradient approximation (GGA). In order to better describe strong electronic interaction between localized Ti *3d* electrons some authors used LDA+U method [7-10].

The $SrTiO_3/LaAlO_3$ system was treated within a supercell method using four different types of supercell geometry which are shown in Fig. 3.1. Initial studies focused primarily on symmetric superlattices consisting of nonstoichiometric films of $SrTiO_3$ and $LaAlO_3$ along (001) direction. When $SrTiO_3$ film has an extra TiO_2 layer and $LaAlO_3$ film has an extra LaO layer, then two identical n-type interfaces are formed (see Fig. 3.1a). On the other hand, an extra SrO layer in $SrTiO_3$ film and an extra AlO_2 layer in $LaAlO_3$ film lead to p-type interfaces (see Fig. 3.1c). The main advantage of symmetric superlattices is that the resulting structure has a relatively small unit cell and doesn't require extensive computational time. The disadvantage is that this geometry doesn't

permit study of the origin of the two-dimensional electron gas (2DEG). Indeed, for the n-type (p-type) interface due to lack of stoichiometricity one additional electron (hole) is introduced into the system which means that essentially 0.5 carriers per 2D cell are doped at each interface. Therefore, the origin of the carriers at the interface is in a sense trivial as being a result of artificial chemical composition. Incidentally, as we will discuss below, the sheet density of 0.5 carriers per 2D cell is exactly the charge required to fully compensate the polar field of the stoichiometric $LaAlO_3$ film and is donated to the interface in the limit of thick $LaAlO_3$ film. Therefore, the symmetric superlattices are ideal to study the properties of the 2DEG for thick $LaAlO_3$ films.

The second type of geometry adds vacuum region to the supercell. Here stoichiometric $SrTiO_3$ and $LaAlO_3$ films form a single interface and both have a free surface at the other end (see Fig.3.1b and d). The third type of geometry corresponds to the asymmetric superlattices (Fig. 3.1e) where both types of interface are present. Here both $SrTiO_3$ and $LaAlO_3$ films are stoichiometric. Finally, in the fourth type of geometry we have a $LaAlO_3$ film that is embedded between two stoichiometric $SrTiO_3$ films whose other ends have a free surface (Fig. 3.1f). When the $LaAlO_3$ film is stoichiometric then both types of interface are present and the structure is asymmetric. On the other hand, for nonstoichiometric $LaAlO_3$ film the structure has a mirror symmetry and only one type of interface is present.

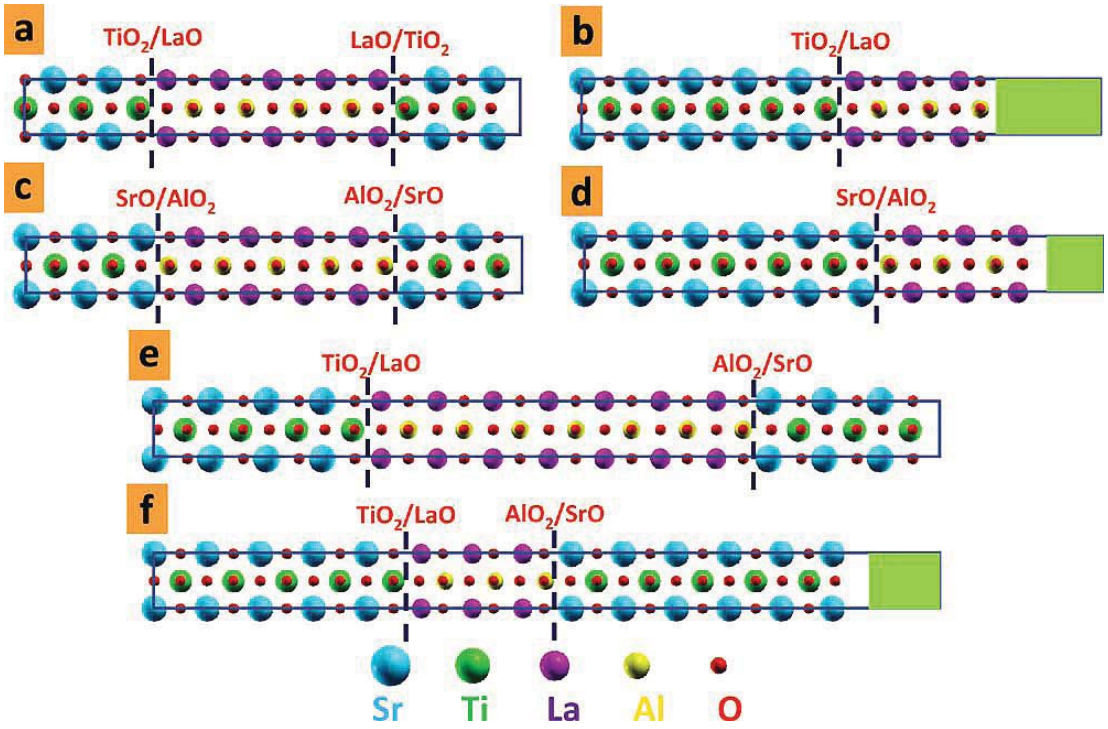

Figure 3.1: Schematic pictures of various geometries employed in first principles studies of $SrTiO_3/LaAlO_3$. The shaded green regions denote vacuum. Structures (a) and (c) represent nonstoichiometric symmetric superlattices for n- and p-type interface, respectively. Structures (b) and (d) represent stoichiometric slab with two surfaces and a single interface of n or p type, respectively. Structure (e) represents an asymmetric superlattice where both films are stoichiometric. Finally structure (f) represents the $LaAlO_3$ film embedded between two $SrTiO_3$ films whose other ends have free surfaces. The figure is adapted from Ref. [11].

3.2 Polar catastrophe model

As discussed in the previous chapter, three different mechanisms for the origin of the 2DEG at the $SrTiO_3/LaAlO_3$ n-type interface have been proposed: polar catastrophe, oxygen vacancies and interface intermixing. The problem is that in experiment all three mechanisms may be present simultaneously and therefore it is difficult to determine which one is the most important. On the other hand, in the first principles approach one can easily separate a particular mechanism and analyze its importance for creation of the 2DEG. For example, by considering a defect-free interface with stoichiometric $SrTiO_3$ and $LaAlO_3$ films the polar catastrophe mechanism can be explored.

The polar catastrophe mechanism can be better understood by considering the idealized (without electronic reconstruction) energy band diagram for the n-type interface as shown in Fig. 3.2. On the left side of the interface we have $SrTiO_3$ where fully occupied valence bands are composed of the O *p*-states and empty conduction bands are formed by the Ti *3d*-states. On the $LaAlO_3$ side the valence band is also composed of the O *p*-states while the conduction band is formed by the La *5d*-states. Both films are assumed to have free surface so that the system geometry corresponds to Fig. 3.1b. Due to the polar nature of $LaAlO_3$ there is an electric field through the stoichiometric $LaAlO_3$ film so that bands slope up linearly inside $LaAlO_3$ film as seen in Fig. 3.2. The slope is upward since for the n-type interface the positively charged $(LaO)^+$ layer is at the interface which attracts the electrons. Note that for the p-type interface the slope is downward.

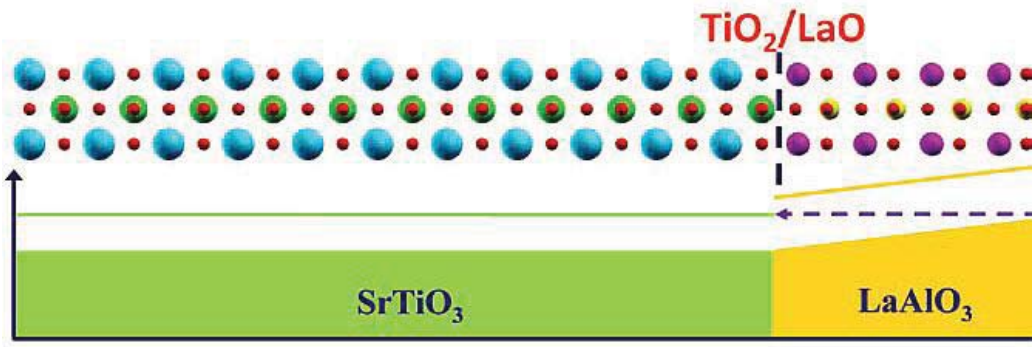

Figure 3.2: Schematic energy diagram for the n-type $SrTiO_3/LaAlO_3$ interface. We use the same color coding for atoms as in Fig. 3.1. The shaded areas are filled valence bands. The conductions bands are empty and their edges are denoted by the solid lines. The figure is adapted from Ref. [11].

As seen from Fig. 3.2, the energy gap of the entire system is given by the difference between the conduction band edge of $SrTiO_3$ and the valence band edge at the $LaAlO_3$ surface. As $LaAlO_3$ film becomes thicker, the surface valence band edge increases linearly with thickness. Therefore, as $LaAlO_3$ film reaches certain critical thickness, the gap closes and system becomes metallic. This is accompanied by the electron transfer from $LaAlO_3$ surface to the $SrTiO_3$ film. As now $LaAlO_3$ film is positively charged, it attracts these additional electrons localizing them close to the interface and leading to the formation of the 2DEG. As the thickness of the $LaAlO_3$ film further increases, more electrons are transferred to the interface. This continues until the internal electric field in $LaAlO_3$ film is fully compensated. This is achieved when 0.5 electrons per 2D unit cell is transferred to the interface.

The above analysis was based on idealized energy band diagram of the interface structure that was constructed from electronic structure of bulk $SrTiO_3$ and $LaAlO_3$. In reality we have substantial electronic and ionic relaxations close to the interface and the surfaces that lead to band bending and screening of the internal electric field in the $LaAlO_3$ film. These effects can be properly taken into account by first principles calculations.

First principles calculations for system geometries as in Fig. 3.1b and f have confirmed the presence of insulator-metal transition as thickness of the $LaAlO_3$ film increases [3, 8, 12, 13]. The quantity that can be directly compared with experiment is the critical thickness. From the discussion above, however, it is clear that the critical thickness depends on the band gap of $SrTiO_3$. Within LDA or GGA the band gap of $SrTiO_3$ ranges between 1.8-1.9 eV [3, 12, 13] which strongly underestimates the experimental value of 3.2 eV. Consequently, the critical thickness would be also underestimated. In order to correct for the band gap error the critical thickness can be estimated as a product of experimental band gap of $SrTiO_3$ and inverse of internal electric field obtained from LDA/GGA calculations (the band offset between $SrTiO_3$ and $LaAlO_3$ is very small ~ 0.1 eV but it can be simply included). Alternatively, one can use LDA+U method to obtain correct $SrTiO_3$ band gap [8].

Different first principles calculations lead to critical thickness in the range of 4 to 6 unit cells of $LaAlO_3$. This discrepancy comes from different calculated values of internal electric field in $LaAlO_3$. One can understand the spread of values of the internal electric field by noting that the internal electric field is inversely proportional to the

dielectric constant. It was shown that the dielectric constant in $LaAlO_3$ is very sensitive to the in-plane lattice constant and the value of internal electric field [11]. These, in turn are very sensitive to the technical parameter of calculations such as pseudopotential, plane wave cutoff, etc. which explains different critical thickness obtained by different authors.

In general, calculated values of critical thickness seem to overestimate experimental values [14-16] that range between 2 and 4 unit cells of $LaAlO_3$ depending on the measurement method (see Chapter II). Possibly, this could be explained by underestimation of $LaAlO_3$ band gap that leads to overestimation of the dielectric constant and consequently underestimation of the internal electric field.

Concluding this section we note first principles calculations for the defect-free n-type $SrTiO_3/LaAlO_3$ interface predict insulator-metal transition with increasing thickness and taking into account approximations involved, the value of the critical thickness is in a reasonable agreement with experiment. This strongly supports polar catastrophe model as being an important mechanism responsible for the origin of 2DEG at the $SrTiO_3/LaAlO_3$ n-type interface.

3.3 Interface electronic structure

The extra electrons doped from the $LaAlO_3$ film were found to occupy interface Ti *3d* states. In the bulk $SrTiO_3$ the *3d* states are split by octahedral crystal field into t_{2g} triplet and e_g doublet with t_{2g} lying at lower energies. At the interface the t_{2g} are further split into lower lying d_{xy} states and degenerate d_{xz} and d_{yz} states. For 2DEG electron

density of 0.5 electron per 2D unit cell all t_{2g} bands were found to be partially occupied [3, 12, 17].

The character of the occupied bands at the interface was used to explain discrepancies between experimental and theoretical values of the 2DEG charge density [17]. The argument is that some of d_{xy}, d_{xz} and d_{yz} bands which are strongly bound to the interface and have large effective mass can undergo Anderson localization and therefore will not appear in transport explaining low 2DEG charge density found in high-quality samples (see Chapter II) [12, 17].

3.4 Confinement of the two-dimensional electron gas

An important characteristic of the 2DEG at the n-type $SrTiO_3/LaAlO_3$ interface is its spatial extent. It is well known that spatial extent of 2DEG formed at interfaces between conventional semiconductors is determined by band bending. As discussed in details in Chapter V, the confinement of the 2DEG at SrTiO3/$LaAlO_3$ n-type interface is not solely due to bend bending [18]. In fact, the 2DEG extends beyond band bending region and decays exponentially with characteristic length of about 2 nm [18]. This behavior can be explained as a result of the metal induced gap states (MIGS) which decay exponentially into bulk of $SrTiO_3$ with characteristic decay length determined by the lowest decay rate of the complex band structure at the Fermi energy of the system (see Chapter V for details) [18]. Recently, more accurate calculations by Son *et al.*, [12] have shown that at larger distances from the interface the spatial decay of the 2DEG

changes from exponential to the one governed by power law. This, however, doesn't contradict the MIGS model as the decay rate of MIGS depends on the energy and therefore the MIGS charge density at a given distance from interface is given by an integral over energy of the exponential factors with both exponents and prefactors being energy dependent. In addition, for $SrTiO_3$ there are two complex bands with comparably low decay length and both should be included. Further, the dependence is complicated by band bending. These effects can cause non-precise exponential decay of the 2DEG.

An alternative mechanism for the confinement of the 2DEG was proposed in Chen *et al.* [3]. They pointed out that at the n-type interface Ti-La distance is considerably smaller than Ti-Ti distance. This proximity together with relatively large spatial extent of La *5d* states leads to strong enhancement of the tight-binding hopping parameter between interfacial Ti *3d* and La *5d* states. This large hopping parameter leads to formation of the bonding and antibonding states with the bonding states being mainly of the Ti *3d* character while antibonding states of the La *5d* character. As a result Ti *3d* states have lower energy at the interface than in the bulk and are therefore occupied by extra electrons doped from the $LaAlO_3$ film. This model was supported by first principles calculations where the spatial extent of the 2DEG was found to vary as Ti-La bond at the interface was changed [3].

3.5 Electronic ordering at the $SrTiO_3/LaAlO_3$ interface

As discussed above, the extra electrons transferred from the $LaAlO_3$ film to the interface occupy Ti *3d* states. Due to localized nature of these states, the Coulomb interaction between those states is expected to be strong and may lead to various electronic orderings. Indeed, as discussed in Chapter II, superconductivity and different types of magnetic order including ferromagnetism and antiferromagnetism have been observed at the SrTiO3/$LaAlO_3$ n-type interface. Since the description of superconductivity is typically beyond the capabilities of first principled methods, most studies focused on magnetic order. Here the symmetric superlattice geometries from Fig. 3.1a were used.

We showed that for thick $SrTiO_3$ the system is nonmagnetic within LDA but application of LDA+U method with U = 5 eV makes 2DEG ferromagnetic [19]. Interestingly, for thin $SrTiO_3$ films the 2DEG is ferromagnetic even within LDA and addition of Hubbard U leads to half-metalicity [19]. This was explained as a result of 2DEG confinement that enhances the density of states at the Fermi level so that the Stoner criterion is fulfilled (see Chapter VI for details).

Pentcheva and Picket studied both unrelaxed [5] and relaxed [9] n-type interfaces using c(2 × 2) lateral cell, and applying LDA+U with U = 8 eV and J = 1 eV. In addition to the ferromagnetism they found a checkerboard charge order that makes interface insulating. This result was insensitive to inclusion of atomic relaxations. Upon removing

Hubbard U, the ferromagnetism and charge order were suppressed and the interface was metallic [9].

The finding of insulating charged order state [5, 9] seems to be at odds with experiments that clearly find conducting interface. However, as argued by authors of Ref. [5, 9], with half the Ti sites empty and strong fluctuations that are pronounced by the 2D character of the system, frequent hopping is expected that may explain high interface conductivity.

Different results were reported by Zhong and Kelly [10]. Using LDA+U with U= 5 eV and J = 0.64 eV they obtained instead a p(2 × 2) antiferromagnetic insulating state with charge ordering. Further, in contrast to Ref. [9], they found atomic relaxations to be crucial for stabilization of magnetic ordering. They, however, also found that the insulating ferromagnetic state with c(2 × 2) charge order is only 10 meV higher in energy.

Summarizing this section we note that different types of magnetic and charge orderings were reported by first principles calculations. Interestingly, as discussed in Chapter II, similarly contradicting experimental results were reported. This seems to indicate that different electronic orders compete with each other and depending on experimental conditions or computational parameters one can obtain different results. This suggests exciting direction for future research aiming to switch between different electronic orderings by external means (for example the gate field).

3.6 The p-type interface

Several *ab initio* works have been devoted to the SrTiO3/$LaAlO_3$ p-type interface [3-5]. The main objective here was to elucidate the observed experimentally insulating nature of this interface.

Within LDA or GGA it was found that the p-type interface, similarly to the n-type interface, becomes metallic with the Fermi surface created from hole electronic states of the O *2p* character [3-5]. In contrast to the n-type interface, the holes are not confined to the interface but instead delocalize into the $SrTiO_3$ substrate [3]. This indicates that the electric field originating from the negatively charged $LaAlO_3$ film is not strong enough to localize holes to the interface (at least for the $SrTiO_3$ thickness of 11 unit cells; for larger thicknesses the electric field is expected to finally localize holes but with rather large spatial extent) [3]. This finding supports the idea that for the n-type interface it is the enhancement of Ti-La hybridization at the interface that localizes the extra electrons close to the interface [3]. As, apparently, there is no such binding force at the p-type interface, the holes delocalize over $SrTiO_3$ film.

The above finding that the p-type interface is metallic doesn't agree with experiment. Several effects were thus proposed that can restore the insulating nature of this interface. In particular, Pentcheva and Picket [5] explored the possibility that the strong electronic correlations can induce a self-trapped hole polaron at the p-type interface. They showed that using LDA+U and sufficiently large U on O *2p* states (larger than 7 eV) one may expect ground state to be antiferromagnetic insulator with charge order. These findings were however based on unrelaxed atomic positions and it is not

clear how relaxations that are pronounced at such interface would change this result. Another open question is what should be the "correct" U parameter for O *2p* states.

It was proposed that extrinsic effects, such as oxygen vacancies, can restore insulating nature of the p-type interface [20]. Indeed, as discussed in Chapter II, from the polar catastrophe model it follows that 25% vacancy concentration should accommodate extra holes and make the p-type interface insulating. This was confirmed by first principles calculations for the unrelaxed interface [5]. When relaxations are included higher vacancy concentration (but not higher than 50%) is needed to cause system to be insulating [4]. This agrees with experiment where the vacancy concentration of 32% was found at the insulating p-type interface [22].

The above studies put oxygen vacancies directly at the interface. However, as discussed above, the holes are delocalized over rather large distance from the interface. Consequently, vacancies away from the interface are also able to trap holes. Within the thick $SrTiO_3$ substrate there surely will be enough oxygen vacancies, created either by thermal fluctuations or due to growth conditions, to immobilize all holes transferred from $LaAlO_3$ [11].

References

[1] W. C. Lee and A. H. MacDonald, Phys. Rev. B **76**, 075339 (2007).

[2] C. Cen, *et al.*, Nature Mater. **7**, 298 (2008).

[3] H. Chen, A. M. Kolpak, and S. Ismail-Beigi, Phys. Rev. B **79**, 161402 (2009).

[4] M. S. Park, S. H. Rhim, and A. J. Freeman, Phys. Rev. B **74**, 205416 (2006).

[5] R. Pentcheva and W. E. Picket, Phys. Rev. B **74**, 035112 (2006).

[6] P. R. Willmott, *et al.*, Phys. Rev. Lett. **99**, 155502 (2007).

[7] V. I. Anisimov, F. Aryasetiawan, and A. I. Liechtenstein, J. Phys. Condens. Matter **9**, 767 (1997).

[8] J. Lee and A. Demkov, Phys. Rev. B **78**, 193104 (2008).

[9] R. Pentcheva and W. E. Picket, Phys. Rev. B **78**, 205106 (2008).

[10] Z. Zhong and P. J. Kelly, Europhys. Lett. **84**, 27001 (2008).

[11] H. Chen, A. M. Kolpak, and S. Ismail-Beigi, Adv. Matter. **22**, 2881 (2010).

[12] W. joon Son, *et al.*, Phys. Rev. B **79**, 245411 (2009).

[13] R. Pentcheva and W. E. Picket, Phys. Rev. Lett. **102**, 107602 (2009).

[14] S. Thiel, *et al.*, Science **313**, 1942 (2006).

[15] M. Sing *et al.*, Phys. Rev. Lett. **102**, 176805 (2009).

[16] G. Berner *et al.*, Phys. Rev. B **82**, 241405(R) (2010).

[17] Z. S. Popović, S. Satpathy and R. M. Martin, Phys. Rev. Lett. **101**, 256801 (2008).

[18] K. Janicka, J. Velev, and E. Y. Tsymbal, Phys. Rev. Lett. **102**, 106803 (2009).

[19] K. Janicka, J. Velev, and E. Y. Tsymbal, J. Appl. Phys. **103**, 07B508 (2008).

[20] N. Nagakawa, *al.*, Nature Mater. **6**, 493 (2007).

Chapter 4 Computational methodology

In this work we investigate $LaAlO_3/SrTiO_3$ interface and related systems using first principles electronic structure methods. In this approach one study the properties of materials directly by solving the Schrödinger equation for system of electrons and nuclei. In this chapter I describe how it is achieved and what approximations are used.

4.1 The Born Oppenheimer approximation

The nonrelativistic Hamiltonian (in this work relativistic effects are not considered) for a system of electrons and nuclei interacting by Coulomb forces is given by:

$$H_{tot} = -\sum_I \frac{\hbar^2}{2M_I}\nabla^2_{\mathbf{R}_\mathrm{I}} - \sum_i \frac{\hbar^2}{2m}\nabla^2_{\mathbf{r}_\mathrm{i}} - \sum_{iI}\frac{Z_I e^2}{|\boldsymbol{R}_I - \boldsymbol{r}_i|} + \frac{1}{2}\sum_{i\neq j}\frac{e^2}{|\boldsymbol{r}_i - \boldsymbol{r}_j|} + \frac{1}{2}\sum_{I\neq J}\frac{Z_I Z_J e^2}{|\boldsymbol{R}_I - \boldsymbol{R}_J|} \qquad (4.1)$$

Here $\{\mathbf{R}_\mathrm{I}\}$ and $\{\mathbf{r}_\mathrm{i}\}$ are nuclear and electron coordinates, respectively. The first term is the kinetic energy of nuclei, the second term is the kinetic energy of electrons, the third term is the electron-nucleus interaction, the fourth term is the electron-electron interaction, and the fifth term is the nucleus-nucleus interaction. The corresponding Schrödinger equation is given by

$$H_{tot}\Phi(\{\boldsymbol{r_i}\},\{\boldsymbol{R}_I\}) = W\Phi(\{\boldsymbol{r_i}\},\{\boldsymbol{R}_I\}), \qquad (4.2)$$

where Φ and W are called vibronic wavefunctions and vibronic energies, respectively.

For solid-state systems where the number of electrons and nuclei is very large the direct solution of (4.2) is nearly impossible. Fortunately, the nuclear masses (M_I) are in general much larger than the electron mass (m) which allows us to introduce some simplifying approximations. We first introduce an electronic Hamiltonian, by dropping the kinetic energy of nuclei from H_{tot}

$$H = -\sum_i \frac{\hbar^2}{2m}\nabla_{\mathbf{r}_i}^2 - \sum_{iI}\frac{Z_I e^2}{|\boldsymbol{R}_I - \boldsymbol{r}_i|} + \frac{1}{2}\sum_{i\neq j}\frac{e^2}{|\boldsymbol{r}_i - \boldsymbol{r}_j|} + \frac{1}{2}\sum_{I\neq J}\frac{Z_I Z_J e^2}{|\boldsymbol{R}_I - \boldsymbol{R}_J|} \tag{4.3}$$

Note that the nuclear coordinates appear in *H* merely as parameters. Consequently, the eigenfunctions $\psi_n(\{\boldsymbol{r}_i\};\{\boldsymbol{R}_I\})$ and eigenvalues $E_n(\{\boldsymbol{R}_I\})$ of the electronic Hamiltonian also depend on the nuclear coordinates as parameters; the suffix n summarizes the electronic quantum numbers. Since the electronic eigenfunctions form a complete basis we can write vibronic wavefunctions as

$$\Phi(\{\boldsymbol{r}_i\},\{\boldsymbol{R}_I\}) = \sum_n \chi_n(\{\boldsymbol{R}_I\})\,\psi_n(\{\boldsymbol{r}_i\};\{\boldsymbol{R}_I\}) \ , \tag{4.4}$$

where $\chi_n(\{\boldsymbol{R}_I\})$ can be interpreted as nuclear wavefunctions. Substituting (4.4) into (4.2) we obtain an equation for $\chi_n(\{\boldsymbol{R}_I\})$

$$\left(-\sum_I \frac{\hbar^2}{2M_I}\nabla_{\mathbf{R}_I}^2 + E_n(\{\boldsymbol{R}_I\})\right)\chi_n(\{\boldsymbol{R}_I\}) + \sum_m \Lambda_{\mathrm{nm}}(\{\boldsymbol{R}_I\})\,\chi_m(\{\boldsymbol{R}_I\}) = W\chi_n(\{\boldsymbol{R}_I\}) \ , \tag{4.5}$$

where $\Lambda_{\mathrm{nm}}(\{\boldsymbol{R}_I\}) = -\sum_I \frac{\hbar^2}{2M_I}\langle\psi_n|\nabla_{\mathbf{R}_I}^2\psi_m\rangle - \sum_I \frac{\hbar^2}{M_I}\langle\psi_n|\nabla_{\mathbf{R}_I}\psi_m\rangle\cdot\nabla_{\mathbf{R}_I}$ is called the non-adiabatic operator (here the bracket notation denotes integration over electronic coordinates). It can be shown that $\Lambda_{\mathrm{nm}}(\{\boldsymbol{R}_I\})$ is of the order of m/M_I and therefore can be neglected leading to

$$\left(-\sum_I \frac{\hbar^2}{2M_I}\nabla^2_{\mathbf{R_I}} + E_n(\{\boldsymbol{R}_I\})\right)\chi_n(\{\boldsymbol{R}_I\}) = W\chi_n(\{\boldsymbol{R}_I\}) \ . \quad (4.6)$$

This is called Born-Oppenheimer adiabatic approximation [1]. This is physically a very sound approximation as electrons (due to smaller mass) move much faster than nuclei and therefore see nuclei as immobile. Nuclei on the other hand move in the potential created by electrons. In fact, as seen from (4.6), the electronic eigenvalues thought as a function of nuclear coordinates play the role of a potential for nuclear dynamics and for this reason there are also called adiabatic potential curves. In the Born-Oppenheimer approximation, the dynamics of the system is confined in the given adiabatic curve (we are usually interested in the ground state adiabatic curve $E_0(\{\boldsymbol{R}_I\})$). The mixing between different potential curves leads to the electron-phonon interaction that is important for resistivity or superconductivity. This can be taken into account using perturbation theory that is justified due to smallness of $\Lambda_{\mathrm{nm}}(\{\boldsymbol{R}_I\})$. The only exception is when different adiabatic curves cross. In this case Born-Oppenheimer approximation is not valid and the mixing must be properly accounted for by solving equation (4.5) in the subspace of degenerate potential curves.

We can further simplify Eq. (4.6) (or its time-dependent version) by neglecting quantum effects. In particular, when we consider ground state adiabatic curve, the classical equations of motion for nuclei are

$$M_I\ddot{\boldsymbol{R}}_I = \boldsymbol{F}_I(\{\boldsymbol{R}_I\}) \ \equiv -\nabla_{\mathbf{R_I}} E_0(\{\boldsymbol{R}_I\}). \quad (4.7)$$

The forces $\boldsymbol{F}_I$ can be evaluated with the help of Hellman-Feynman theorem

$$\nabla_{\mathbf{R}_\mathrm{I}} E_0(\{\boldsymbol{R}_I\}) = \langle \psi_0 | \nabla_{\mathbf{R}_\mathrm{I}} \mathrm{H} | \psi_0 \rangle, \tag{4.8}$$

so that simply expectation value of the gradient of the electronic Hamiltonian is needed.

By minimizing forces (so that they vanish), we can find the equilibrium nuclear configurations. This is called nuclear relaxation. Small displacement from the equilibrium can be further studied by expanding $E_0(\{\boldsymbol{R}_I\})$ up to second order in the Taylor series around equilibrium positions. Then equation of motions can be solved analytically and lattice vibration spectra can be obtained. The quantum nature of nuclei can be recovered by quantization of lattice vibration leading to phonons. Alternatively, Eq. (4.7) can be solved directly by Molecular Dynamics techniques [2] which don't require assumption for small displacements.

4.2 Density functional theory

While Born-Oppenheimer approximation allows us to decouple electronic and nuclear subsystems, the solution of the problem described by the electronic Hamiltonian remains a tremendous task. The reason is the presence of the electron-electron interactions that correlates motions of different electrons and prevents us from factorization of the wavefunction into product of single-electron wavefunctions. The most popular approach to this problem is the density functional theory [3, 4] which is used in this work. This approach is based on the fact that the ground state energy of a many-particle system can be expressed as a functional of the ground state density [3]. The actual ground state density can be found by minimization of that functional [3]. In

addition, density functional theory provides a reasonable approximation of the functional. This method allows us to study the ground state properties of the many electron system by solving a simple one-electron Schrodinger equation with a local effective potential.

We consider a system of N electrons interacting with themselves by Coulomb forces and affected by a single-electron external potential. The Hamiltonian is given by

$$H = -\sum_i \frac{\hbar^2}{2m}\nabla_{\mathbf{r}_i}^2 + V_{ext} + \frac{1}{2}\sum_{i\neq j}\frac{e^2}{|\boldsymbol{r}_i - \boldsymbol{r}_j|}, \tag{4.9}$$

where $V_{ext} = \sum_i \ v_{ext}(\boldsymbol{r}_i)$.

The first Hohenberg-Kohn theorem [3] states that there is a one-to-one correspondence between the ground state electron density, n, and the external potential. This theorem together with a trivial observation that the ground state wavefunction, ψ_0, is the functional of the external potential imply that ψ_0 is the functional of the ground state density. Consequently, the ground state energy is a functional of the ground state density and can be written as

$$E_0[n] = T[n] + E_{ee}[n] + \int v_{ext}(\boldsymbol{r})n(\boldsymbol{r})d\boldsymbol{r} \ , \tag{4.10}$$

where T and E_{ee} are ground state expectation values of the kinetic energy and the electron-electron interaction, respectively. Note that from the first theorem it follows that T and E_{ee} are also functionals of the ground state density.

The second Hohenberg-Kohn theorem [3] states that for the fixed external potential when we vary n(**r**), the global minimum of the functional (4.10) is equal to the exact ground state energy and n(**r**) that minimizes the functional is equal to the exact

ground state density. This stationary property allows us to find the ground state density and the ground state energy of the system without solving the Schrödinger equation. Following Kohn and Sham [4] we imagine an auxilary system of N non-interacting electrons, whose ground state density is equal to the ground state density of the interacting system with Hamiltonian (4.9) so that

$$n(\boldsymbol{r}) = \sum_i^{occ} \phi_i^*(\boldsymbol{r})\phi_i(\boldsymbol{r}), \tag{4.11}$$

where ϕ_i are single particle orthonormal orbitals of the non-interacting system known as Kohn-Sham eigenfunctions and the summation is over N lowest states. Minimization with respect to the ground state density can be replaced by minimization with respect to $\{\phi_i\}$. In order to do this it is convenient to rewrite Eq. (4.10) as

$$E_0[n] = T_0[n] + E_H[n] + \int v_{ext}(\boldsymbol{r})n(\boldsymbol{r})d\boldsymbol{r} + E_{xc}[n], \tag{4.12}$$

where $T_0[n] = \sum_{i=1}^{occ} \left\langle \phi_i \middle| \frac{-\hbar^2}{2m}\nabla^2 \middle| \phi_i \right\rangle$ is the ground state expectation value of the kinetic energy of the non-interacting system, $E_H[n] = \frac{1}{2}\int \frac{e^2}{|\boldsymbol{r}-\boldsymbol{r}'|} n(\boldsymbol{r})n(\boldsymbol{r}')d\boldsymbol{r}d\boldsymbol{r}'$ is called Hartree energy, and the exchange-correlation energy is defined as $E_{xc}[n] = T[n] - T_0[n] + E_{ee}[n] - E_H[n]$. Minimization of (4.12) with respect to $\phi_1, \phi_2, \ldots\ldots \phi_N$ subject to the constraint of orthonormality leads to Kohn-Sham Schrödinger-like equation:

$$H_{KS}\phi_i(\boldsymbol{r}) = \left[\frac{-\hbar^2}{2m}\nabla^2 + v_{ext}(\boldsymbol{r}) + V_H(\boldsymbol{r}) + V_{xc}(\boldsymbol{r})\right]\phi_i(\boldsymbol{r}) = \varepsilon_i\phi_i(\boldsymbol{r}), \tag{4.13}$$

where H_{KS} is the Kohn-Sham Hamiltonian, $V_H(\boldsymbol{r}) = \int \frac{e^2}{|\boldsymbol{r}-\boldsymbol{r}'|} n(\boldsymbol{r}')d\boldsymbol{r}'$ is the Hartree potential, $V_{xc}(\boldsymbol{r}) \equiv \frac{\delta E_{xc}[n]}{\delta n(\boldsymbol{r})}$ is called exchange-correlation potential, and ε_i are Lagrange

multipliers that are called Kohn-Sham eigenvalues. Solving Kohn-Sham equation for $\phi_i(\boldsymbol{r})$ and ε_i allows us to find the ground state density from (4.11) and the ground state energy from

$$E_0 = \sum_i^{occ} \varepsilon_i + E_{dc}, \tag{4.14}$$

where $E_{dc} = E_H[n] + E_{xc}[n] - \int V_{xc}(\boldsymbol{r}) n(\boldsymbol{r}) \mathrm{d}\mathbf{r}$ is the so-called double counting correction.

The major problem with the density functional theory is the fact that the exchange-correlation energy functional is unknown and for practical calculations it must be somehow approximated. Many different forms for $E_{xc}[n]$ have been proposed but the most popular is the local density approximation (LDA) [4]

$$E_{xc}^{LDA}[n] = \int \varepsilon_{xc}\big(n(\boldsymbol{r})\big) n(\boldsymbol{r}) d\boldsymbol{r} \,. \tag{4.15}$$

Here $\varepsilon_{xc}\big(n(\boldsymbol{r})\big)$ denotes the exchange-correlation energy per electron of a uniform gas of interacting electrons of density n($\mathbf{r}$). Typically, parameterization for $\varepsilon_{xc}\big(n(\boldsymbol{r})\big)$ based on quantum Monte Carlo calculations [5] is used.

LDA can be straightforwardly extended to the magnetic systems leading to the local spin density approximations (LSDA). In this case the exchange-correlation energy becomes a functional of the ground state densities for electrons with spin up ($n^{\uparrow}$) and down ($n^{\downarrow}$) which are allowed to be different

$$E_{xc}^{LSDA}\left[n^{\uparrow}, n^{\downarrow}\right] = \int \varepsilon_{xc}\left(n^{\uparrow}(\boldsymbol{r}), n^{\downarrow}(\boldsymbol{r})\right) n(\boldsymbol{r}) d\boldsymbol{r}. \tag{4.16}$$

Here $\varepsilon_{xc}\left(n^{\uparrow}(\boldsymbol{r}), n^{\downarrow}(\boldsymbol{r})\right)$ is the exchange-correlation energy per electron of a uniform gas of interacting electrons with spin densities $n^{\uparrow}$ and $n^{\downarrow}$. As a result the ground state energy (4.12) also becomes a functional of $n^{\uparrow}$ and $n^{\downarrow}$. The Kohn-Sham equations must be then solved for each spin $\sigma = \uparrow, \downarrow$ with the spin-dependent exchange correlation potential, $V_{xc}^{\sigma}(\boldsymbol{r}) \equiv \frac{\delta E_{xc}[n^{\uparrow}, n^{\downarrow}]}{\delta n^{\sigma}(\boldsymbol{r})}$.

First principles calculations based on LDA were very successful in predicting binding energies and equilibrium structures of many solids. However, there are many well known failures of LDA. The most serious problem is that LDA consistently underestimates band gaps of semiconductors and insulators. In fact, this is not necessarily problem of LDA as even for the exact exchange correlation functional the Kohn-Sham eigenvalues are not equal to the excitation spectrum of the many-body system of interest.

LDA is known to also have a problem with the systems containing localized electrons, for example 3d electrons in transition metal ions or 4f electrons in rare-earth ions. In this case, one can often improve LDA by adding additional Hubbard-like interaction between the localized electrons. This is an essence of LDA+U method where the Hubbard term is treated in Hartree-Fock manner [6, 7]. In the full spherically symmetric formulation by Liechtenstein *et al.* [7] the additional contribution to the LDA exchange-correlation functional is

$$E_U[\{n_{mm'}^{\sigma}\}] = \frac{1}{2}\sum_{\{m\}\sigma}\Big[\langle mm''|V_{ee}|m'm'''\rangle n_{mm'}^{\sigma} n_{m''m'''}^{-\sigma} - (\langle mm''|V_{ee}|m'm'''\rangle - \langle mm''|V_{ee}|m'''m'\rangle) n_{mm'}^{\sigma} n_{m''m'''}^{\sigma}\Big] \quad , \tag{4.17}$$

where m is the magnetic quantum number, $n^{\sigma}_{mm'}$ is the density matrix, and V_{ee} is the screened Coulomb interaction between the localized electrons. It can be shown that that the matrix elements in Eq. (4.17) can be expressed in terms of two parameters U and J that can be interpreted as Coulomb and Stoner parameters [7]. Note that, in general, the above formulation depends on the choice of the localized basis functions $|m\rangle$ but this ambiguity has no big effect on numerical results.

The density functional theory is applicable to the electronic Hamiltonian given by Eq. (4.3). Here the electron-nucleus interaction plays the role of the external potential V_{ext} and the nucleus-nucleus interaction is just a constant term that doesn't depend on coordinates of electrons. Nevertheless, the latter should be included when working with the electronic Hamiltonian for extended systems as it cancels divergent terms from the Hartree energy. In addition, the nucleus-nucleus interaction is important for evaluation of the ionic forces (4.7) after the self-consistent ground state electron density is found. Using (4.8) the ionic forces are given by

$$\boldsymbol{F}_I(\{\boldsymbol{R}_I\}) = -\int d\boldsymbol{r} n(\boldsymbol{r}) \nabla_{\boldsymbol{R}_I} V_{ext}(\boldsymbol{r}) - \nabla_{\boldsymbol{R}_I} E_{II}\,, \tag{4.18}$$

where $V_{ext}(\boldsymbol{r}) = -\sum_{iI} \frac{Z_I e^2}{|\boldsymbol{R}_I - \boldsymbol{r}_i|}$ and $E_{II} = \frac{1}{2}\sum_{I \neq J} \frac{Z_I Z_J e^2}{|\boldsymbol{R}_I - \boldsymbol{R}_J|}$.

4.3 Plane waves, pseudopotentials and projector augmented wave method

For each system of interest defined by the external potential $v_{ext}(\boldsymbol{r})$ the Kohn-Sham equation (4.13) must be solved selfconsistently. One usually starts with a reasonable approximation for the ground state density from which Hartree and the exchange-correlation potentials are calculated. The new density can be obtained from the solution of the corresponding Kohn-Shame equation according to (4.11). This process is repeated until selfconsistency is reached.

In order to solve the Kohn-Sham equation, one typically expands the Kohn-Sham eigenfunctions in a finite basis and then diagonalizes the Kohn-Sham Hamiltonian matrix in this basis to obtain the Kohn-Sham eigenfunctions and eigenvalues.

We are concerned here with crystals where $v_{ext}(\boldsymbol{r})$ is a lattice periodic function. The Blöch theorem is therefore valid and the Kohn-Sham eigenfunctions can be written as

$$\phi_{\boldsymbol{kn}}(\boldsymbol{r}) = u_{\boldsymbol{kn}}(\boldsymbol{r})e^{i\boldsymbol{k}\cdot\boldsymbol{r}} \ , \tag{4.19}$$

where **k** is a wavevector in the first Brillouin zone, n is a band index and $u_{\boldsymbol{kn}}(\boldsymbol{r})$ has a periodicity of the lattice. This greatly simplifies the problem and thus even for nonperiodic systems like interfaces, it is customary to enforce periodicity using the supercell method.

For periodic systems plan waves constitute a particularly convenient basis. Expanding (4.19) in plane waves leads to [8]

$$\phi_{\boldsymbol{kn}}(\boldsymbol{r}) = \frac{1}{\sqrt{\Omega}} \sum_{\boldsymbol{G}} c_{\boldsymbol{Gkn}} e^{i(\boldsymbol{G}+\boldsymbol{k})\cdot\boldsymbol{r}}, \tag{4.20}$$

where Ω is the volume of the crystal and $\boldsymbol{G}$ are reciprocal lattice vectors. Substituting (4.20) into (4.13), multiplying by $\frac{1}{\sqrt{\Omega}} e^{i\boldsymbol{G}\cdot\boldsymbol{r}}$ and integrating over **r** leads to the matrix equation for the expansion coefficients $c_{\boldsymbol{Gkn}}$

$$\sum_{\boldsymbol{G}'} H_{\boldsymbol{GG}'}(\boldsymbol{k}) c_{\boldsymbol{G}'\boldsymbol{kn}} = \varepsilon_{\boldsymbol{kn}}\, c_{\boldsymbol{G}'\boldsymbol{kn}}, \tag{4.21}$$

where $H_{\boldsymbol{GG}'}(\boldsymbol{k}) = \frac{\hbar^2}{2m}|\boldsymbol{k}+\boldsymbol{G}|^2 \delta_{\boldsymbol{GG}'} + v_{ext}(\boldsymbol{G}-\boldsymbol{G}') + V_H(\boldsymbol{G}-\boldsymbol{G}') + V_{xc}(\boldsymbol{G}-\boldsymbol{G}')$ and for external (ionic), Hartree and exchange-correlation potentials we introduced a Fourier transform $V(\boldsymbol{G}) = \frac{1}{\Omega_{\text{cell}}} \int_{\Omega_{\text{cell}}} V(\boldsymbol{r}) \exp(-i\boldsymbol{G}\cdot\boldsymbol{r}) d\boldsymbol{r}$ with Ω_{cell} being a unit cell volume**.**

In principle, the plane wave basis is infinite, but for large $\boldsymbol{G}$ vectors the diagonal kinetic energy term becomes dominant and thus the basis may be truncated to include only plane waves with the kinetic energy less than some particular cutoff energy E_{cut} i.e., we only keep $\boldsymbol{G}$ vectors satisfying $|\boldsymbol{G}+\boldsymbol{k}| < \sqrt{\frac{2mE_{cut}}{\hbar^2}}$. The cutoff energy is a convergence parameter that must be found for each system (it must be increased until results don't depend on it). In the truncated basis Eq. (4.21) can be solved for each **k** by diagonalizing $H_{\boldsymbol{GG}'}(\boldsymbol{k})$ to obtain $\varepsilon_{\boldsymbol{kn}}$ and $c_{\boldsymbol{G}'\boldsymbol{kn}}$.

In the plane waves methods the size of the Hamiltonian matrix $H_{\boldsymbol{GG}'}$ is typically very large and thus direct diagonalization is very inefficient. Instead, for each k-point one

finds N_{bands} lowest eigenvectors using iterative methods (see Ref. [9] for review). The advantage is that N_{bands} can be much smaller than number of plane waves leading to more efficient method. The specific algorithms for the iterative methods are very sophisticated but the basic idea [8] is to start with some initial guess for the eigenvectors $|c_{\boldsymbol{kn}}^{(0)}\rangle$, where the components of vectors are indexed by $\boldsymbol{G}$ vectors and n =1, …, N_{bands}. Then the corresponding approximate eigenvalues are found from

$$\varepsilon_{\boldsymbol{kn}}^{(0)} = \frac{\left\langle c_{\boldsymbol{kn}}^{(0)} \middle| \widehat{H} \middle| c_{\boldsymbol{kn}}^{(0)} \right\rangle}{\left\langle c_{\boldsymbol{kn}}^{(0)} \middle| c_{\boldsymbol{kn}}^{(0)} \right\rangle}, \tag{4.22}$$

where $\widehat{H}$ is a Hamiltonian matrix with elements $H_{\boldsymbol{GG'}}$. The residual vector

$$|R_{\boldsymbol{kn}}^{(0)}\rangle = \left(\widehat{H} - \varepsilon_{\boldsymbol{kn}}^{(0)}\right)|c_{\boldsymbol{kn}}^{(0)}\rangle \tag{4.23}$$

can be then calculated. $|R_{\boldsymbol{kn}}^{(0)}\rangle$ represents deviation of initial eigenvectors from the true eigenvectors. It is used to improve the eigenvectors so that they become close to the exact ones

$$|c_{\boldsymbol{kn}}^{(n+1)}\rangle = |c_{\boldsymbol{kn}}^{(n)}\rangle + K|R_{\boldsymbol{kn}}^{(n)}\rangle \quad . \tag{4.24}$$

This procedure is repeated until the residual vector vanishes, within some tolerance. Here K is called a preconditioning matrix that can be arbitrarily chosen in order to speed up convergence.

Despite the efficiency of iterative methods, the plane wave basis would be impractical when applied to the actual ionic potentials due to prohibitive size of the

Hamiltonian matrix needed to describe strongly oscillating behavior of the wavefunctions in the core region. However, the most physical properties of solids are independent on the core electrons and only valence electrons are important. This is therefore a good approximation to remove core electrons and strong ionic potential and replace them by much weaker pseudopotential that acts on the valence electrons. Typically, pseudopotential must be nonlocal, i.e. it is different for different angular momenta. However, since it can be described by much smaller number of plane waves, it still leads to a very efficient electronic structure method.

Initially, pseudopotentials were constructed empirically using some general form with few adjustable parameters fitted to atomic data. Nowadays, however, *ab initio* pseudopotentials are in use. They are usually constructed for a free atom and are capable of describing valence electrons in other environments (like solids or molecules), a property referred to as transferability.

Generation of a pseudopotential for a given element starts with all-electron calculations for a free atom using DFT. Note that for consistency when we use pseudopotentials in solids or in molecules, we need to use the same approximation for the exchange-correlation potential that was used for construction of the pseudopotential. Typically, exchange-correlation potentials retain atomic spherical symmetry so that only the radial Schrödinger equation must be solved and each orbital quantum number l can be treated separately. The energy ε_l for which radial equation must be solved (atomic configuration) also needs to be specified. This choice is dictated by valence states for which pseudopotential is to be generated but, in general, it doesn't have to be equal to the

atomic eigenvalues. The next step is to specify a core region as a circle around the atom of radius R_l. Small values of R_l lead to hard pseudopotentials that have a good transferability but are not very smooth and require many plane waves in the basis (larger E_{cut}). Larger values of R_l result in smoother soft pseudopotentials which, however, come at the cost of transferability.

For each l, the "screened" pseudopotential is found in such a way that it generates pseudo wavefunction that satisfy the following properties: i) all-electron and pseudo wavefunctions are the same beyond R_l, ii) the logarithmic derivatives of the all-electron and pseudo wavefunctions are equal at R_l, iii) inside R_l all-electron and pseudo wavefunction differ but the integrated charge inside R_l for both wavefunctions must be equal. The last condition, called norm-conservation [10], ensures that the total charge in the core region is correct and that the normalized all-electron and pseudo wavefunctions agree beyond R_l (first condition ensures agreement up to arbitrary multiplicative constant). More importantly, however, the norm conservation condition leads to good transferability of pseudopotentials. In fact, it requires that the first energy derivatives of the logarithmic derivatives of all-electron and pseudo wavefunctions are equal at R_l. This condition, in turn, ensures that the pseudopotential reproduces the changes of eigenvalues to linear order due to change in the self-consistent potential (which changes when atom is put in a different environment like molecule or solid).

Initially "screened" pseudopotentials satisfying above requirements were produced by assuming some parameterized form of the pseudopotential and varying parameters until the conditions are met. A simpler procedure is to first find pseudo

wavefunction and then generate pseudopotential by inversion of the radial Schrödinger equation. Typically, inside R_l pseudo wavefunction is taken to be a linear combination of few Bessel functions and coefficients of expansion are chosen such that the above conditions are satisfied [11].

The "screened" pseudopotential corresponds to the total potential that contains Hartree and exchange-correlation potentials. In order to obtain the bare ionic pseudopotential which is transferrable to other environments these contributions must be subtracted, i.e. the pseudopotential must be "unscreened".

In the pseudopotential approximation, the ionic potential in Kohn-Sham equation (4.13) is replaced by

$$v_{ext}(\boldsymbol{r}) = \sum_I \frac{Ze^2}{|\boldsymbol{R}_I - \boldsymbol{r}|} \rightarrow \sum_I \left(V_I^{local}(r) + \sum_{lm} |lm\rangle V_{Il}^{nonloc}(r) \langle lm| \right) . \quad (4.25)$$

Here $|lm\rangle$ are spherical harmonics. In practice, we consider only orbital quantum numbers up to $l = 2$ (or $l = 3$ for *f*-electron systems). We explicitly separated local V_I^{local} (l-independent) part of the pseudopotential by $V_{Il}^{tot} = V_I^{local} + V_{Il}^{nonloc}$ where V_{Il}^{tot} is the total pseudopotential. The freedom in choosing V_I^{local} is usually utilized to make is as strong as possible. The nonlocal pseudopotential V_{Il}^{nonloc} equals to zero beyond corresponding core region. It is convenient to express the second term in (4.25) using Kleinman-Bylander form [12] $\sum_{IJ} \sum_{\substack{lm \\ l'm'}} |\beta_{Ilm}\rangle D_{ll'mm'}^{IJ} \langle \beta_{Jl'm'}|$,where $D_{ll'mm'}^{IJ}$ are strengths of nonlocal pseudopotential and β_{Ilm} are a projection functions which are nonzero only within R_l sphere around each atom.

While norm-conserving pseudopotentials lead to an efficient method to solve Kohn-Sham equations, they have a problem treating materials containing certain elements which have nodeless valence states, for example *3d* electrons in transition metal atoms. Such states are localized to the corresponding nucleus and creation of transferable norm-conserving pseudopotentials require very small core radii resulting in very hard pseudopotentials that are prohibitively expensive for plane wave calculations.

To circumvent this problem Vanderbilt [13] introduced a new class of pseudopotentials, so-called ultrasoft pseudopotentials, in which norm conservation requirement has been relaxed. This allows for much larger values of R_l and consequently smoother pseudopotentials that need smaller number of plane waves making plane wave calculations faster and applicable to systems with nodeless valence states. On the other hand, the transferability of the ultrasoft pseudopotentials is comparable to norm-conserving pseudopotentials since more reference energies (usually two) are used for constructions of pseudopotentials.

In order to construct an ultrasoft pseudopotential we first construct a pseudo wavefunction φ_i^{PS} for each reference energy ϵ and orbital quantum number l in the same way as above but not requiring norm conservation; here $i = (lm, \epsilon)$. We then construct projection functions β_i that are dual to pseudo wavefunctions, $\langle \beta_i | \varphi_j^{PS} \rangle = \delta_{ij}$, using

$$|\beta_i\rangle = \sum_j (B^{-1})_{ij} |\chi_j\rangle \quad , \tag{4.26}$$

where $B_{ij} = \langle \varphi_j^{PS} | \chi_i \rangle$ and $|\chi_i\rangle = -(T + V^{local} - \epsilon)|\varphi_i^{PS}\rangle$ with V^{local} being an arbitrarily chosen local potential. The total pseudopotential is the sum of the V^{local} and the nonlocal part given by

$$V_{NL} = \sum_{ij} D_{ij} |\beta_j\rangle\langle\beta_i| \ . \tag{4.27}$$

The nonlocal part of the pseudopotential automatically has the Kleinman-Bylander form with the strength of the nonlocal pseudopotentials given by

$$D_{ij} = B_{ij} + \epsilon_i q_{ij}. \tag{4.28}$$

Here $q_{ij} = \int Q_{ij}(\boldsymbol{r}) d\boldsymbol{r}$ where $Q_{ij}(\boldsymbol{r}) = \varphi_i^{AE}(\boldsymbol{r})\varphi_j^{AE}(\boldsymbol{r})^* - \varphi_i^{PS}(\boldsymbol{r})\varphi_j^{PS}(\boldsymbol{r})^*$ are called augmentation functions. The second term in (4.28) represents the fact that all-electron φ_i^{AE} and pseudo wavefunctions have different norms.

Note that the relaxation of the norm conservation condition causes that the Blöch eigenstates are not orthogonal anymore. This requires introduction of the overlap matrix $S = 1 + \sum_{ij} q_{ij} |\beta_j\rangle\langle\beta_i|$ in the eigenvalue problem (4.21). Fortunately, iterative methods can also handle such generalized eigenvalue problem.

In this work we solved Kohn-Sham equations using projector augmented wave (PAW) method [14]. In principle, this is an all-electron method but it strongly related to pseudopotential approach and, in particular, ultrasoft pseudopotentials can be derived as a limiting case of PAW [15]. In PAW, we adopt a frozen core approximation in which the core states are found as for isolated atom and together with nucleons provide the ionic

potential v_{ext} for the valence electrons. We then write Bloch solutions of the Kohn Sham equation for the valence electrons as

$$|\phi_{\boldsymbol{kn}}\rangle = |\tilde{\phi}_{\boldsymbol{kn}}\rangle + \sum_i \left(|\varphi_i^{AE}\rangle - |\varphi_i^{PS}\rangle\right)\langle\beta_i||\tilde{\phi}_{\boldsymbol{kn}}\rangle \,. \tag{4.29}$$

Here $\tilde{\phi}_{\boldsymbol{kn}}$ is a pseudo Bloch function that is smooth and can be represented by a reasonable number of plane waves. The index *i* is shorthand for an atomic site inside the unit cell, the angular momentum numbers $\{lm\}$, and additional index *k* referring to the reference energy ϵ_{kl} (usually two reference energies are used for each *l*). Functions φ_i^{AE}, φ_i^{PS}, and β_i are the same as in the ultrasoft pseudopotential method. Using (4.29) the ground state density can be written as [14]

$$n(\boldsymbol{r}) = \tilde{n}(\boldsymbol{r}) + n^1(\boldsymbol{r}) - \tilde{n}^1(\boldsymbol{r}), \tag{4.30}$$

where

$$\tilde{n}(\boldsymbol{r}) = \sum_{\boldsymbol{kn}}^{occ} \tilde{\phi}_{\boldsymbol{kn}}^*(\boldsymbol{r})\, \tilde{\phi}_{\boldsymbol{kn}}(\boldsymbol{r}) \tag{4.31}$$

is the pseudo charge density

$$n^1(\boldsymbol{r}) = \sum_{ij} \rho_{ij} \left(\, \varphi_i^{AE}(\boldsymbol{r}) \,\right)^* \varphi_i^{AE}(\boldsymbol{r}) \tag{\4.32}$$

and

$$\tilde{n}^1(\boldsymbol{r}) = \sum_{ij} \rho_{ij} \left(\, \varphi_i^{PS}(\boldsymbol{r}) \,\right)^* \varphi_i^{PS}(\boldsymbol{r}) \,. \tag{4.33}$$

Here $\rho_{ij} = \sum_{\boldsymbol{kn}}^{occ} \langle \tilde{\phi}_{\boldsymbol{kn}}|\beta_i\rangle\langle\beta_j|\tilde{\phi}_{\boldsymbol{kn}}\rangle$ are called the PAW occupancies.

Within the PAW method we derive a modified Kohn-Sham equation by minimizing the ground state energy (4.12) with respect to pseudo wavefunction $\tilde{\phi}_{\boldsymbol{kn}}$ subject to the appropriate orthonormality constraint. Using (4.29) and the fact that $\phi_{\boldsymbol{kn}}$ are orthonormal the orthonormality condition can be found to be $\langle \tilde{\phi}_{\boldsymbol{k'n'}} | S | \tilde{\phi}_{\boldsymbol{kn}} \rangle = \delta_{\boldsymbol{kk'}} \delta_{nn'}$ where the overlap matrix is the same as in the ultrasoft pseudopotential method. As a result, we obtain a generalized eigenvalue problem very similar as in the ultrasoft pseudopotential method but with additional onsite contribution to the potentials, see Refs. [14, 15]. Further, the Hellman-Feynman forces can be evaluated from (4.8) [14, 15].

References

[1] M. Born and R. Oppenheimer, Ann. Physique **84**, 457 (1927).

[2] B. J. Alder and T. E. Wainwright, J. Chem. Phys. **31**, 459 (1959).

[3] P. Hohenberg and W. Kohn, Phys. Rev. **136**, 864B (1964).

[4] W. Kohn and L. Sham, Phys. Rev. **140**, 1133A (1965).

[5] D. M. Ceperley and B. J. Alder, Phys. Rev. Lett. 45, 566 (1980).

[6] V. I. Anisimov, J. Zaanen, and O. K. Andersen, Phys. Rev. B 44, 943 (1991).

[7] A. I. Liechtenstein, V. I. Anisimov, and J. Zaanen, Phys. Rev. B 52, R5467 (1995).

[8] R. M. Martin, *Electronic structure: Basic Theory and practical methods*,

[9] G. Kresse and J. Furthmüller, Phys. Rev. B **54**, 11169 (1996).

[10] D. R. Haman, M. Schlüter, and C. Chiang, Phys. Rev. Lett. **43**, 1494 (1979).

[11] G. Kresse and J. Hafner, J. Phys. Cond. Matter. **6**, 8245 (1994).

[12] L. Kleinman and D. Bylander, Phys. Rev. Lett. **48**, 1425 (1982).

[13] D. Vanderbilt, Phys. Rev. B **41**, 7892 (1990).

[14] P. E. Blöchl, Phys. Rev. B **50**, 17953 (1994).

[15] G. Kresse and D. Joubert, Phys. Rev. B **59**, 1758 (1999).

Chapter 5 Quantum nature of the two-dimensional electron gas confinement at the $SrTiO_3/LaAlO_3$ interface

In this chapter we study the confinement of the two-dimensional electron gas (2DEG) formed at the $SrTiO_3/LaAlO_3$ n-type interface using first principles electronic structure calculations [1]. We show that the 2DEG confinement can be explained by the formation of metal –induced gap states (MIGS) [2, 3] in the band gap of $SrTiO_3$. These states are formed as a result of quantum-mechanical tunneling of the charge created at the interface due to electronic reconstruction. This electronic tunneling occurs through the effective confining potential which can be found through band structure calculation. The attenuation length of the MIGS into $SrTiO_3$ is governed by the lowest decay rate evanescent states of bulk $SrTiO_3$ which are identified through complex band structure calculations for bulk $SrTiO_3$. Our calculations predict that the 2DEG is confined in $SrTiO_3$ within about 1 nm at the interface.

5.1 Metal-induced gap states

Since metal induced gap states (MIGS) [2, 3] play a central role in the physical mechanism responsible for the confinement of the 2DEG at the $SrTiO_3/LaAlO_3$ interface, in this section we review the basic properties of MIGS and their relation to the complex band structure.

According to the Bloch theorem, eigenfunctions of the bulk crystal Hamiltonian are Bloch waves

$$\phi_{\boldsymbol{kn}}(\boldsymbol{r}) = u_{\boldsymbol{kn}}(\boldsymbol{r})e^{i\boldsymbol{k}\cdot\boldsymbol{r}}, \tag{5.1}$$

where **k** is a wavevector from the first Brillouin zone, n is a band index and $u_{\boldsymbol{kn}}(\boldsymbol{r})$ has a periodicity of the lattice [4]. For an infinite system only real wavevectors are allowed. Indeed Bloch waves with complex wavevectors cannot be normalized as they would diverge at infinity. However, when the periodicity is broken by presence of some boundary (for example surface or interface), the Bloch waves with nonzero imaginary part of the wavevector in the direction normal to the boundary are allowed. Such evanescent states decay exponentially as we go away from the boundary into the bulk of the crystal and at the boundary they are matched by the wavefunction outside the crystal [2, 3]. Note that the boundary induced changes in the charge density and the potential are usually confined within first few monolayers from the boundary and beyond this region the Hamiltonian of the system is essentially bulk-like. For this reason the evanescent states can be studied using the bulk Hamiltonian.

Assuming that the boundary is perpendicular to the *z* axis we can split the wavevector into a part parallel to the boundary, $\mathbf{k}_{\|}$, and a part perpendicular to the boundary, k_z. As discussed above, *x*-*y* plane periodicity requires $\mathbf{k}_{\|}$ to be real but the presence of the boundary allows for complex $k_z = q + i\kappa$. The imaginary part, κ, is called the decay parameter since, according to Eq. 5.1, it corresponds to the evanescent Bloch wave that decays as $\sim e^{-\kappa z}$. The eigenvalues of the crystal Schrödinger, or Kohn-Sham, equation, for a certain $\mathbf{k}_{\|}$ and arbitrary complex k_z, form complex band structure of

the crystal. The complex band structure can be calculated for the bulk system without any reference to the nature of the boundary [5, 6].

For a given $\mathbf{k}_{\|}$, complex bands form the so-called real lines in the three-dimensional (q, κ, E) space where E is energy. The analytic properties of the real lines were studied by Kohn [7] and Heine [3, 4] and the topology of the complex bands was studied by Chang [5]. The real lines always appear in pairs of $\pm\kappa$ but the physically relevant states are those that decay as we go away from the boundary into the bulk of the crystal. Real lines depart from the real q axis wherever there is an extremum of the real band structure with respect to q. The bands can either extend in energy to $-\infty$, forming free-electron-like parabolic solutions, or connect back to other extrema of the real band structure forming loops.

Consider the case of insulator or semiconductor. In the bulk the electronic band structure is characterized by the presence of energy gap that separates occupied valence bands from empty conduction bands. No Bloch waves with a real wavevector exist in the band gap. However, evanescent states with energies within the band gap can exist. When the interface between an insulator and a metal is formed, typically Fermi level of the metal lies within the band gap of the insulator. Therefore, the evanescent states within the insulator band gap can couple to the metallic states forming so-called metal-induced gap states (MIGS) [2, 3] which are occupied by charge coming from the metal.

The concept of the complex band structure was often applied to determine the electronic structure of solids with planar defects (e.g., surfaces, interfaces, stacking faults, grain boundaries or superlattices). The total wavefunction of the system is expanded in

terms of Bloch and evanescent waves on both sides of the boundary plane which, in turn, are obtained from the complex band structure of the bulk constituents. The coefficients of the expansion are then determined by matching at the boundary plane and using appropriate boundary conditions. The main disadvantage of the method is that it doesn't take into account the variation of the charge density close to the boundary plane and therefore the electronic structure in immediate neighborhood of the boundary plane is not correctly described. Nevertheless, this method was very popular in the past when the slab calculations were unfeasible due to insufficient computer resources. In particular, this approach was utilized to determine the electronic structure of surfaces [2], interfaces [8], and superlattices [9]. Nowadays, even though the slab calculations for the systems with planar defects can be easily performed, the analysis of the complex band structure is very useful in interpreting the results and understanding basic physics that controls the electronic structure near the boundary. For example, the concept of MIGS and complex band structure has been invoked to understand the Schottky barrier height on the metal used in the metal-semiconductor interfaces [3, 10]. Further, the efficiency of the electron tunneling in metal/insulator/metal junctions can be understood in terms of MIGS in insulator [11]. In particular, the tunneling rate is determined by the evanescent state with the lowest decay rate assuming that it is allowed by symmetry to couple to the electronic states of the metal at the Fermi level [11].

5.2 Calculation methodology

We consider $(LaAlO_3)_m/(SrTiO_3)_n$ symmetric superlattices with the LaO/TiO_2 interface. Here m and n denote the numbers of atomic layers of $LaAlO_3$ and $SrTiO_3$, respectively. Both n and m are odd numbers as required for symmetric superlattices with a single type of interface. As a result both $LaAlO_3$ and $SrTiO_3$ films are nonstoichiometric which introduces an extra charge in the system of (in the case of the LaO/TiO_2 interface) 0.5e per interface. As discussed in Chapter III, this situation corresponds to the two-dimensional electron gas (2DEG) formed at the LaO/TiO_2 according to the polar catastrophe model in the limit of thick $LaAlO_3$ film. This geometry thus allows us to study the properties of the 2DEG regardless its origin. The $(LaO)_1/(SrTiO_3)_{21}$ superlattice is shown schematically in Fig. 1.

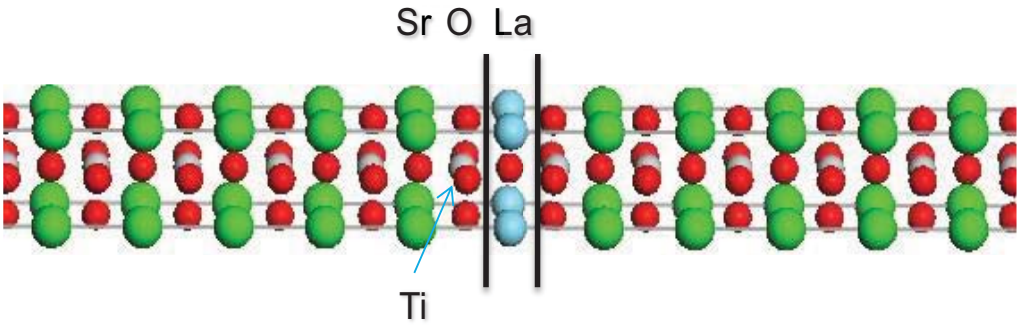

Figure 5.1: Schematic picture of the $(LaO)_1/(SrTiO_3)_{21}$ superlattice. Green, gray, red, and blue circles correspond to Sr, Ti, O, and La ions, respectively.

The atomic and electronic structure of the system were calculated using density functional theory [12, 13] within the local density approximation (LDA) [13] for the exchange correlation potential. In addition, the effects of electronic correlations were studied using LDA+U method [14, 15] with $U = 5$ eV and $J = 0.9$ eV on Ti *3d* states. The Kohn-Sham equations were solved using the projector augmented wave (PAW) method [16, 17] as implemented in the Vienna ab-initio simulation package (VASP) [18, 19].

The in-plane lattice constant was fixed to the theoretical equilibrium value for cubic $SrTiO_3$ within LDA (a = 3.87 Å), while the c/a ratio was optimized for each supercell. Ions were fully relaxed so that forces on each atom were smaller than 10 meV/Å. The energy cutoff for the plane wave expansion was 500 eV and we used $8\times8\times\max(1,8/N)$ k-point mesh where N is the number of unit cells perpendicular to the interface.

5.3 Results

For all superlattices we found strong ionic relaxations near the interface. It mainly involves substantial buckling distortion of the interfacial TiO_2 layer in which negatively charged O ions are displaced toward $LaAlO_3$ film while positively charged Ti ions move away from the $LaAlO_3$ film. This distortion produces an electric dipole which screens the electric field produced by the positively charged nonstoichiometric $LaAlO_3$ film. This behavior is similar to the one observed in $SrTiO_3/LaTiO_3$ superlattices [20].

Similar to the previous studies and as expected for the nonstoichiometric $LaAlO_3$ film, we found that the superlattices are metallic with the conduction charge density of about 0.5e per interface. For thin $SrTiO_3$ films (i.e., $n < 17$), however, our calculations show that the conduction electrons are nearly uniformly distributed over the $SrTiO_3$ film. This spurious behavior results from artificial geometrical confinement within the thin $SrTiO_3$ film. In fact, for thicker $SrTiO_3$ films ($n \sim 23$) the conduction charge density decays as we go away from the interface (see below) demonstrating the presence of the 2DEG that is confined to the interface. These results are rather independent on the thickness of the $LaAlO_3$ film.

Fig. 5.2 shows the local density of states (DOS) on the TiO_2 planes located at different distance l (given in monolayers) from the LaO layer in $LaO/(SrTiO_3)_{23}$ superlattice (m = 1). A substantial band bending is seen resulting, in particular, in the change of the valence band maximum (VBM) and the conduction band minimum (CBM) as a function of l. This is due to the variation of the electrostatic potential which rigidly shifts the bands with respect of the Fermi energy (E_F). We obtain the site-dependent electrostatic potential using the core-like O-2s states shown in the right panels of Fig. 5.2. These states reveal a pronounced peak changing its position with l that we use for the analysis of the band bending. This allows us to find the variation of the CBM in the $SrTiO_3$ film as follows. We add the value Δ_g = 1.83 eV corresponding to the calculated band gap for the bulk $SrTiO_3$ to the VBM obtained for the TiO_2 monolayer at l = 11 (i.e., the TiO_2 monolayer that is the furthest from the interface and its DOS is very much bulk-like). This determines the CBM at this site, which appears to be approximately 0.18 eV above the Fermi energy. This is consistent with the experimental value of 0.25 ± 0.07 eV

[21]. Then, we obtain the site variation of the CBM by adding the electrostatic potential difference from the shift of the core O-2s states. The result is shown by the dashed line in Fig. 5.2.

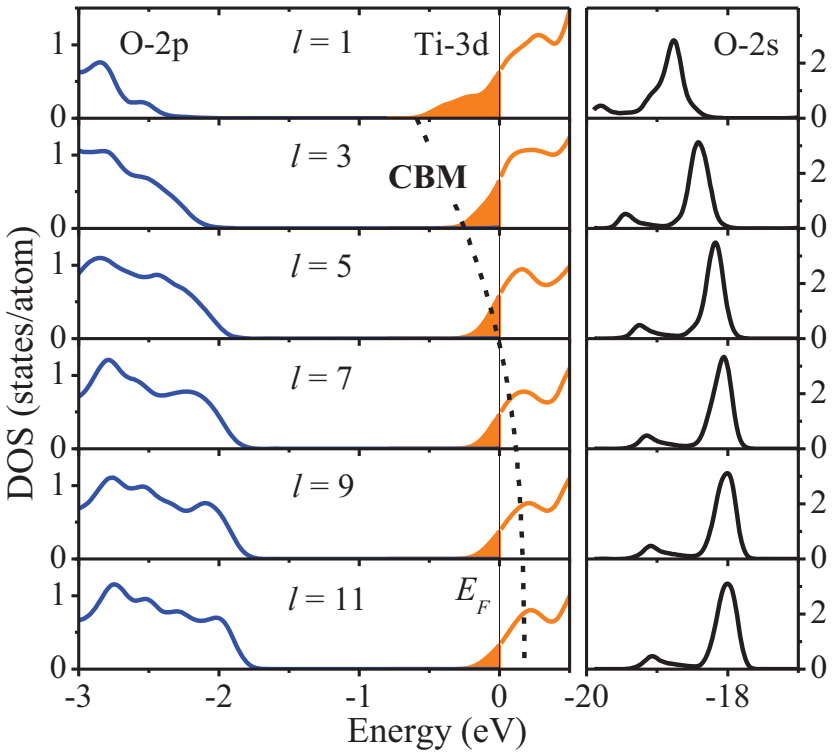

Figure 5.2: Layer-resolved DOS on the TiO_2 planes in $LaO/(SrTiO_3)_{23}$ superlattice (m = 1). Index l denotes the TiO_2 monolayer position away from the LaO monolayer placed at $l = 0$. Left panels show the DOS in the vicinity of the Fermi energy (E_F) denoted by the vertical line. The shaded areas indicate the occupied states forming 2DEG. The dashed line demonstrates the variation of the conduction band minimum (CBM) in $SrTiO_3$. Right panels show the DOS of the O-2s states at energies about 20eV below E_F.

The important conclusion which follows from this analysis is the presence of the substantial valence charge occupying a classically forbidden region. This is seen from the relative position of the CBM with respect to the shaded area in Fig. 5.2 that indicates the amount of charge forming the 2DEG. For $l = 1$ and $l = 3$ almost all the charge resides in the region above the CBM. This is consistent with the classical picture of electrons confined in a potential well. However, for $l = 5$, 7, 9, and 11, we see that the charge occupies a classically forbidden region below the CBM.

The physical mechanism responsible for the presence of charge in the classically forbidden region is quantum-mechanical tunneling under the potential barrier. In fact, the situation here is very similar to the metal/insulator interface. The "metal" is a region close to the $SrTiO_3/LaAlO_3$ interface where due to the band bending the conduction electrons are classically allowed while the "insulator" is the $SrTiO_3$ film beyond this region. Note that the thickness of the "metal" is energy dependent but this doesn't change the main physics here. In analogy to the real meta/insulator interfaces, as discussed in Section 5.1, the conduction electrons from the "metal" can tunnel into the gap of the "insulator" and form metal induced gap states (MIGS) [2, 3]. This is schematically illustrated in Fig. 5.3.

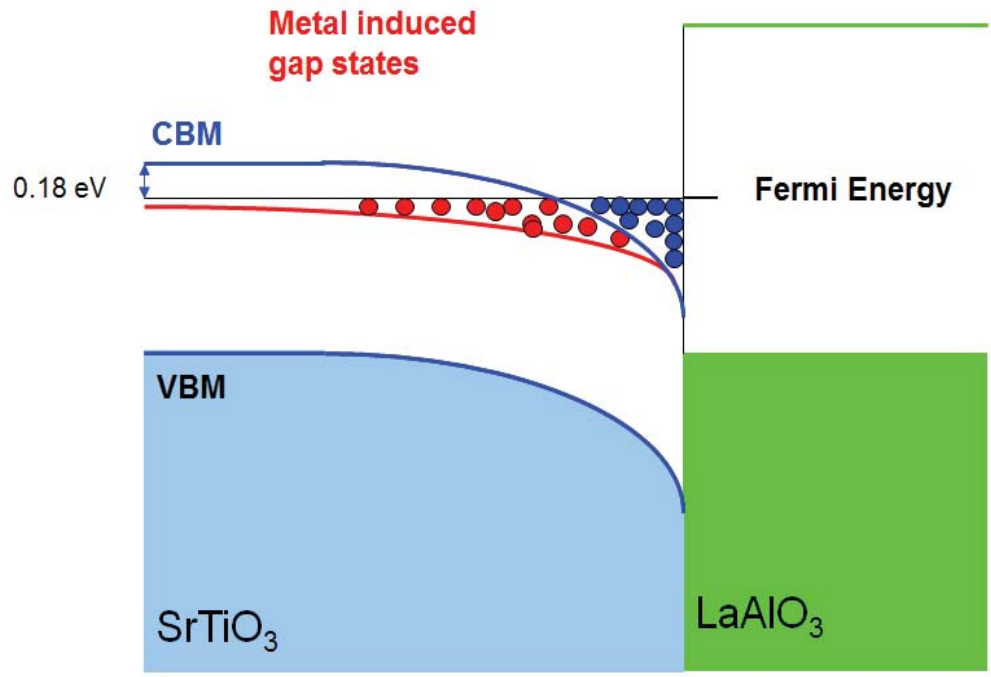

Figure 5.3: Schematic band diagram of the $SrTiO_3/LaAlO_3$ interface and the illustration of the formation of the MIGS. Band bending (blue line) at the $SrTiO_3/LaAlO_3$ interface leads to the notched structure at the $SrTiO_3$ film close to the interface where CBM is below the Fermi level. This forms a classically allowed region where extra electrons from the $LaAlO_3$ film (dark blue circles) can reside. Due to quantum-mechanical tunneling these electrons can tunnel into classically forbidden region forming MIGS (red circles) that determine the confinement of the 2DEG.

Fig. 5.4 shows the charge distribution in the $SrTiO_3$ film, calculated from the integrated partial DOS on Ti sites, for $(LaAlO_3)_m/(SrTiO_3)_{23}$ superlattices with m = 1, 3 and 5. The total amount of the charge on Ti atoms is about 0.39e. A fraction of this charge is confined on the first TiO_2 monolayer from where it decays exponentially in the

bulk of $SrTiO_3$ with the characteristic attenuation length δ. We fit the charge distribution by $n \propto \exp(-z/\delta)$, where z is a distance from the interfacial TiO_2 monolayer, to obtain the attenuation length (see Fig. 5.4). Not unexpectedly, we find that δ is almost independent of the number of $LaAlO_3$ monolayers and is equal to 1.03, 1.08 and 1.18 nm for m = 1, 3, and 5 respectively.

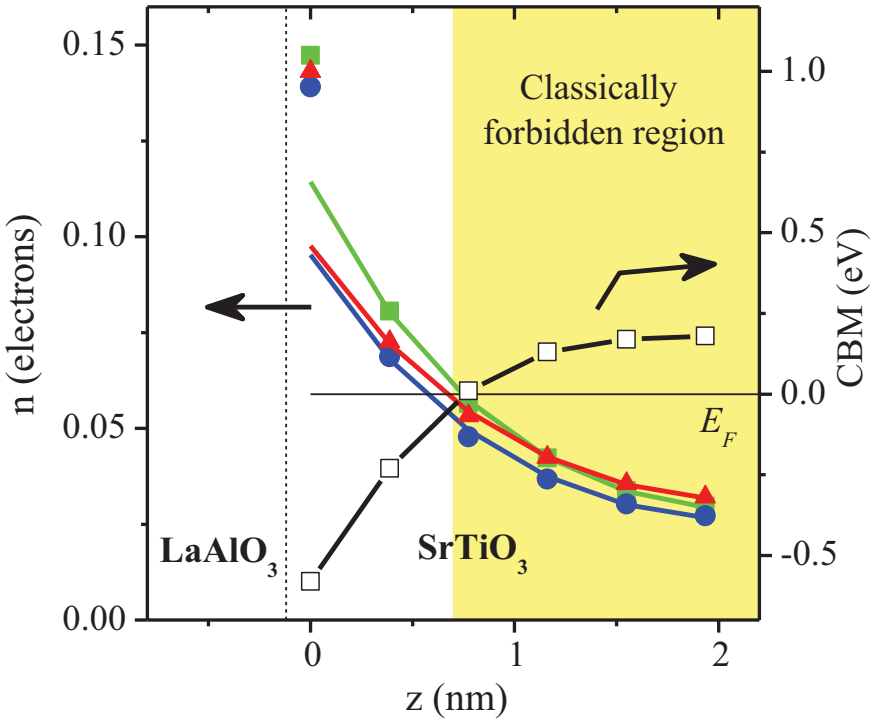

Figure 5.4: Charge on Ti sites (solid symbols) for $(LaAlO_3)_m/(SrTiO_3)_{23}$ superlattices with m = 1 (squares), m = 3 (circles) and m =5 (triangles), and the conduction band minimum (open squares) as a function of distance from the interface z. The interfacial TiO_2 monolayer is placed at z = 0 as a reference. The Fermi energy (EF) is shown by a horizontal line and is related to the CBM plot only.

Fig. 5.4 also shows the variation of the CBM within the $SrTiO_3$ film obtained from the calculation described above. This may be regarded as an effective tunneling potential barrier for the conducting electrons residing at the interface. The Fermi level crossing separates classically allowed and classically forbidden regions in the insulator. The latter is indicated in Fig. 5.4 by the shaded area and contains about 0.42 of the total charge on Ti atoms. The presence of such substantial charge within the classically forbidden region is the evidence for the presence of MIGS at the $SrTiO_3/LaAlO_3$ interface. The classical electrostatic confinement potential is short-ranged and extends only up to the second TiO_2 monolayer; however the charge spills much further due to presence of MIGS. This is the manifestation of the quantum nature of the 2DEG confinement which is determined by MIGS. We also note that only insignificant amount of charge is induced in $LaAlO_3$.

In order to obtain further insights into the electronic properties of the 2DEG, in Fig. 5.5a we have plotted $\mathbf{k}_{\|}$-resolved charge density of the 2DEG for the $LaO/(SrTiO_3)_{23}$ superlattice (m = 1) in the two-dimensional Brillouin zone, integrated in the range of energies from E_F – 1 eV to E_F, which contains the 2DEG. It is seen that the largest charge density is at the Γ point ($\mathbf{k}_{\|}$ = 0). In the vicinity of the Γ point the charge distribution is reminiscent of a Fermi circle. This implies that free electron is a good starting approximation to investigate properties of the 2DEG. The spherical charge distribution for small $\mathbf{k}_{\|}$ is consistent with the band structure of the system which is shown in Fig. 5.6 that reveals quadratic dispersion of the conduction bands close to the Γ point. By fitting these bands to a parabola we find the average effective mass $m^* \approx 9m_e$, which is consistent with the calculations performed for bulk $SrTiO_3$ [22]. Such a large value of the

effective mass is due to the localized nature of the Ti-3*d* states resulting in low band dispersion and is detrimental to achieving high mobility of the 2DEG.

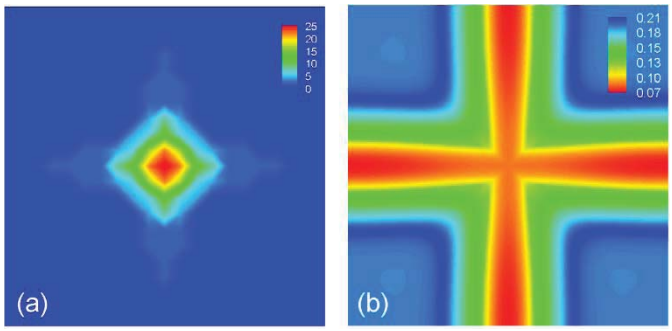

Figure 5.5: $k_{||}$-resolved charge density (a) and the lowest decay rate of the evanescent states in $SrTiO_3$ (b) within the two-dimensional Brillouin zone. The charge density is evaluated for the energy range from E_F – 1.0 eV to E_F. The decay rate (in units of $2\pi/a$) is evaluated for bulk $SrTiO_3$ at 0.2 eV below the CBM.

As we go away from the Γ point, the charge distribution pattern exhibits an outer region with lower charge density deviating from the circular shape. This is the consequence of the decay rate anisotropy in $SrTiO_3$. In order to reveal this anisotropy, we have calculated the complex band structure of bulk $SrTiO_3$ [23]. Fig. 5.5b shows the lowest decay rate of the evanescent states as a function of $\mathbf{k}_{||}$ evaluated at 0.2 eV below the conduction band minimum. In this energy range the lowest decay rate has the Δ_5 symmetry. As seen, the states with the lowest decay rate form a cross pattern along the Γ-M directions in the two-dimensional Brillouin zone. In the area around the Γ point where

the charge density is highest the decay rate is nearly constant and the corresponding attenuation length is about $\delta \sim 0.8$ nm. This is in good agreement with the results of our supercell calculations. Thus, the complex band structure of bulk $SrTiO_3$ correctly estimates the attenuation length of the conduction charge density at the LaO/TiO_2 interface which confirms that the confinement of the 2DEG has a quantum nature and is governed by the formation of MIGS at the interface. This interpretation allows us also to explain the insignificant amount of charge induced in the $LaAlO_3$ film. Indeed, the decay rate in the $LaAlO_3$ is much larger due to a larger band gap and the fact that the Fermi level of the superlattice lies approximately in the middle of the $LaAlO_3$ band gap where the decay rate is maximal. Consequently, MIGS in $LaAlO_3$ decay on much shorter length.

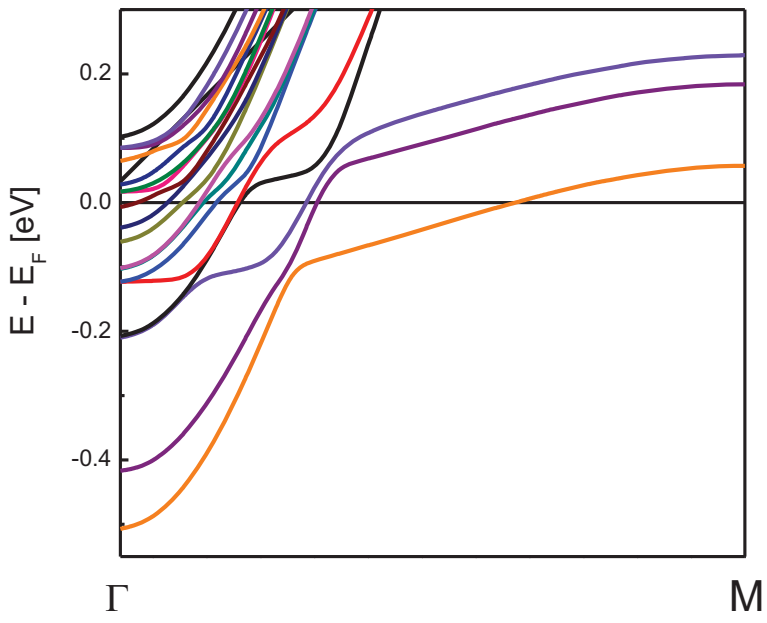

Figure 5.6: Band structure along Γ-M direction of the $LaO/(SrTiO_3)_{23}$ superlattice (m = 1). Close to the Γ point the dispersion of conducting bands is quadratic.

According to the MIGS model the $\mathbf{k}_{\|}$-dependent decay rate determines the shape of the charge density of the 2DEG in the two-dimensional Brillouin zone. Indeed, close to the zone center the decay rate is low and weakly dependent on $\mathbf{k}_{\|}$ producing a nearly spherical part of the charge density. Further away from the Γ point the decay rate sharply increases and exhibits strong anisotropy which is seen in Fig. 5.5a from the elongated contour of the charge density in the [100] and [010] directions.

We note that the well-known problem of LDA to underestimate the band gap does not affect significantly the predicted confinement width. The latter is determined by the conduction band bending due to the electrostatic potential that places the conduction band minimum at a certain position above the Fermi energy. Also the inclusion of electron correlations through LDA+*U* method does not change significantly our results. This is consistent with the previous work [24]. Electron correlations affect the confinement through unequal occupation of the two spin channels which moves slightly the charge center of mass further down in energy. Thus, the charge of the interface faces a slightly higher decay rate in the $SrTiO_3$ [23].

5.4 Conclusions

In conclusion, we find that the 2DEG at the LaO/TiO_2 interface of $LaAlO_3/SrTiO_3$ superlattices is confined in $SrTiO_3$ within about 1 nm from the interface. This 2DEG confinement is formed by the metal induced gap states (MIGS) in the insulator. The latter are the result of quantum-mechanical tunneling of the charge created at the interface due

to electronic reconstruction. The MIGS are controlled by the complex band structure of the insulator through the decay rate of evanescent states. The predicted quantum nature of the 2DEGs at oxide interfaces needs to be taken into account when interpreting experimental data.

References

[1] K. Janicka, J. Velev, and E. Y. Tsymbal, Phys. Rev. Lett. **102**, 106803 (2009).

[2] V. Heine, Proc. Phys. Soc. London **81**, 300 (1962).

[3] V. Heine, Phys. Rev. B **138**, A1689 (1965).

[4] N. W. Ashcroft and N. D. Mermin, *Solid State Physics* (1976).

[5] Y-C. Chang, Phys. Rev. B **25**, 605 (1982).

[6] Y-C Chang and J. N. Schulman, Phys. Rev. B **25**, 3975 (1982).

[7] W. Kohn Phys. Rev. **115**, 809, (1959).

[8] G. C. Osbourn and D. L. Smith, Phys. Rev. B **19**, 2124 (1979).

[9] J. N. Schulman and Y. C. Chang, Phys. Rev. B **24**, 4445 (1981).

[10] J. Tersoff, Phys. Rev. Lett. **52**, 465 (1984).

[11] P. Mavropolus, N. Papanikolaou, and P. H. DEderichs, Phys. Rev. Lett. **85**, 1088 (2000).

[12] P. Hohenberg and W. Kohn, Phys. Rev. **136**, 864B (1964).

[13] W. Kohn and L. Sham, Phys. Rev. **140**, 1133A (1965).

[14] V. I. Anisimov, J. Zaanen, and O. K. Andersen, Phys. Rev. B 44, 943 (1991).

[15] A. I. Liechtenstein, V. I. Anisimov, and J. Zaanen, Phys. Rev. B 52, R5467 (1995).

[16] P. E. Blöchl, Phys. Rev. B **50**, 17953 (1994).

[17] G. Kresse and D. Joubert, Phys. Rev. B **59**, 1758 (1999).

[18] G. Kresse and J. Hafner, Phys. Rev. B **48**, 13115 (1993).

[19] G. Kresse and J. Furthmüller, Phys. Rev. B **54**, 11169 (1996).

[20] S. Okamoto, A. J. Millis, and N. A. Spaldin, Phys. Rev. Lett. **97**, 056802 (2006).

[21] K. Yoshimatsu *et al.*, Phys. Rev. Lett. **101**, 026802 (2008).

[22] W. Wunderlich, H. Ohta, and K. Koumoto, Physica B **404**, 2202 (2009).

[23] J. P. Velev *et al.*, Phys. Rev. Lett. **95**, 216601 (2005).

[24] D. R. Hamman *et al.*, Phys. Rev. B **73**, 195403 (2006).

Chapter 6 Magnetism at the $SrTiO_3/LaAlO_3$ interface

In this chapter I describe first principles electronic structure calculations to elucidate magnetic properties of the $LaAlO_3/SrTiO_3$ n-type interface. We found that in $(LaAlO_3)_3/(SrTiO_3)_3$ superlattice the n-type interface is magnetic with a magnetic moment on the Ti^{3+} atom of $0.2\mu_B$, as revealed by the spin-polarized calculations within the local density approximation. For thicker $SrTiO_3$ layers the magnetic moment decreases and eventually disappears because the electron gas spreads over more than one unit cell, making the electrons delocalized across the superlattice and violating the Stoner criterion for magnetism. Thus, magnetization in these superlattices is due to geometric confinement of the electron gas. The inclusion of electron correlations via the LDA+*U* approximation with $U = 5$ eV on the Ti atoms, makes the two-dimensional electron gas half-metallic, enhances and stabilizes the interface magnetization.

6.1 Introduction

According to the polar catastrophe model the origin of the two-dimensional electron gas (2DEG) at the $LaAlO_3/SrTiO_3$ n-type interface is an electronic reconstruction in which electrons are transferred from the $LaAlO_3$ film into the interface and occupy empty Ti *3d* states which form conduction band in bulk $SrTiO_3$. Since Ti *3d* states are localized close to the Ti ions, the Coulomb interaction between these electrons is large which may lead to magnetic ordering. Indeed, as discussed in Chapter II, there

are experimental evidences that at low temperatures the 2DEG becomes magnetic [1,2 3]. Different experiments, however, reported different types of magnetic order including ferromagnetism [1, 2] and antiferromagnetism [3]. On the other hand, Reyren *et al.* [4] observed that the 2DEG is nonmagnetic but instead it becomes superconducting at low temperatures. Evidently, different types of magnetic order compete with each other and with superconductivity, and depending on sample preparation conditions different electronic orderings set in.

It is therefore of great importance to understand effects of different factors on magnetism of the 2DEG. This knowledge would allow experimentalists to design sample preparation conditions in such a way that the 2DEG would become magnetic. This in turn would open exciting possibilities for application of the $LaAlO_3/SrTiO_3$ interface in spintronic technology. Conversely, as the superconductivity likely competes with magnetism in this system, by growing samples such as to disfavor magnetism one can expect to enhance the superconductivity and therefore to study this exciting state of matter in greater depth.

Several first-principles studies addressed the magnetic properties of the 2DEG at the $LaAlO_3/SrTiO_3$ n-type interface [5, 6, 7]. In particular, Pentcheva and Pickett [5, 6] studied effects of lattice relaxations and electronic correlations on magnetic order. They found that lattice relaxations has a minor effect on magnetism but strong electronic correlations on Ti 3d states included by LDA+U method lead to a ferromagnetic ground state that is accompanied by the c(2 × 2) charge ordering that makes the interface insulating. Without Hubbard U the interface is nonmagnetic and metallic. On the other

hand, Zhong and Kelly [7] have shown that relaxations have a profound effects on magnetic properties and that ferromagnetic state with c(2×2) charge ordering competes with p(2 × 2) antiferromagnetic insulating state with charge ordering.

In this chapter, we study the effect of the thickness of the $SrTiO_3$ film and the electronic correlations on the ferromagnetism of the 2DEG at the $LaAlO_3/SrTiO_3$ n-type interface using first principles calculations [8]. We found that for thin $SrTiO_3$ film the 2DEG is magnetic even in the absence of Hubbard U. On the other hand, when electronic correlations are included by the GGA+U method, the 2DEG becomes half-metallic. For thicker $SrTiO_3$ the 2DEG spreads over the $SrTiO_3$ film making the conduction electrons more delocalized. As a result, within GGA, the Stoner criterion is violated and the 2DEG is nonmagnetic. Inclusion of the Hubbard U, however, stabilizes ferromagnetic order even for thick $SrTiO_3$ films.

6.2 Stoner model

In this section I will review the Stoner model for magnetism (see, for example, Ref. [9]) which, as shown in this Chapter, is able to capture basic physics of magnetic properties of the 2DEG formed at the $LaAlO_3/SrTiO_3$ interface.

The first theory of magnetism was Weiss' molecular field theory (see for example [9]) which assumes that electrons in magnetic crystals form localized magnetic moments that interact with internal molecular field. This picture can be justified in case of insulators. Here one can assume that the electronic structure can be represented by a

collection of weakly interacting ions which according to Hund's rules often have magnetic moments. In case of metals however, the existence of local magnetic moments cannot be easily justified. Therefore, in order to explain magnetism in metals, (like Fe, Co or Ni) Stoner has proposed an alternative approach [10].

In the Stoner model we take into account that electrons in metals are delocalized and form electronic bands. The electronic structure can be described in terms of density of states (DOS). Knowledge of DOS for each spin direction allows us to find number of electrons with spin up and down using

$$n_\sigma = \int_0^{\varepsilon_F} N_\sigma(\varepsilon) d\varepsilon, \tag{6.1}$$

where n_σ and $N_\sigma(\varepsilon)$ are, respectively, a number of electrons and DOS with spin $\sigma = +, -$ (here "+" denotes spin up and "–" denotes spin down). We chose zero energy to be well below the bottom of the valence band and ε_F is the Fermi energy. Fig. 6.1 shows an example of DOS for each spin direction. In this case DOSs for each spin direction are exactly the same so that $n_+ = n_- = n/2$ (here n is the total number of electrons) and the system is nonmagnetic.

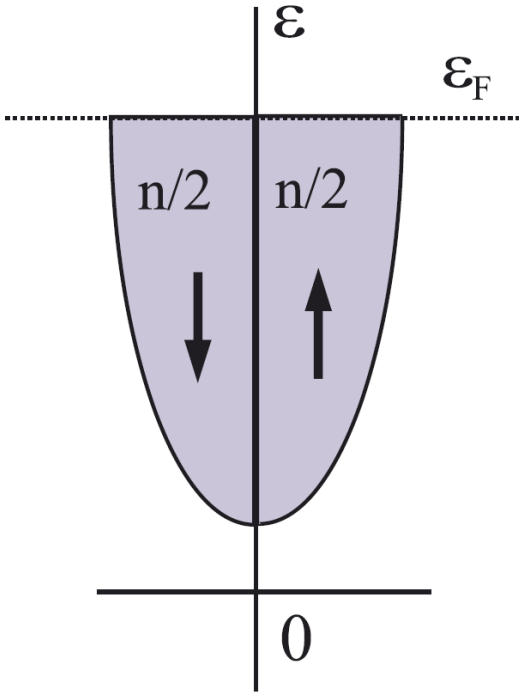

Figure 6.1: Example of a nonmagnetic DOS. Only occupied part (below Fermi level, ε_F) is shown. The figure is adapted from Ref. [9].

Let's imagine now that we apply a small external magnetic field, H_{ext}, so that the DOS is split between the two spins by ΔE (see Fig. 6.2). Consequently, numbers of electrons with spin up and down are different, and we have nonzero magnetization given by

$$m = n^+ - n^- = \int_0^{\varepsilon_F} N_+(\varepsilon)d\varepsilon - \int_0^{\varepsilon_F} N_-(\varepsilon)d\varepsilon = \int_0^{\varepsilon_F} N(\varepsilon + \Delta E/2)d\varepsilon - \int_0^{\varepsilon_F} N(\varepsilon - \Delta E/2)d\varepsilon = \int_0^{\varepsilon_F+\Delta E/2} N(\varepsilon)d\varepsilon - \int_0^{\varepsilon_F-\Delta E/2} N(\varepsilon)d\varepsilon = \int_{\varepsilon_F-\Delta E/2}^{\varepsilon_F+\Delta E/2} N(\varepsilon)d\varepsilon \ . \quad (6.2)$$

Here we used the fact that DOSs for each spin direction are simply shifted versions of the nonmagnetic DOS per spin, $N(\varepsilon)$.

The band energy (i.e. the total energy minus the exchange-correlation energy) of the system is given by

$$E_b = \int_0^{\varepsilon_F} \varepsilon N_+(\varepsilon) d\varepsilon + \int_0^{\varepsilon_F} \varepsilon N_-(\varepsilon) d\varepsilon \,, \tag{6.3}$$

which can be written as

$$E_b = E_b^{NM} + \int_{\varepsilon_F}^{\varepsilon_F + \Delta E/2} \varepsilon N(\varepsilon) d\varepsilon - \int_{\varepsilon_F - \Delta E/2}^{\varepsilon_F} \varepsilon N(\varepsilon) d\varepsilon \,, \tag{6.4}$$

where $E_b^{NM} = 2\int_0^{\varepsilon_F} N(\varepsilon) d\varepsilon$ is the band energy of the nonmagnetic system.

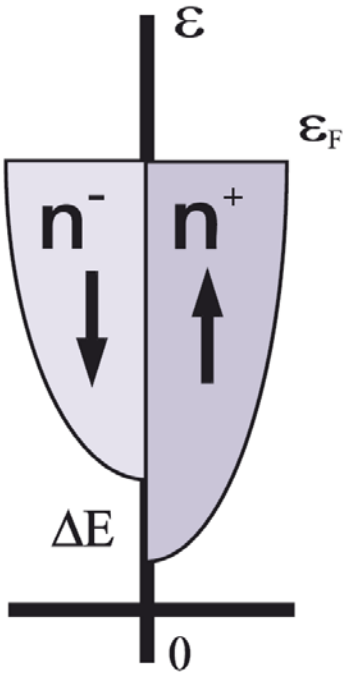

Figure 6.2: Spin-splitting of DOS. Only occupied part (below Fermi level, ε_F) is shown. The figure is adapted from Ref. [9].

Since ΔE is small (because H_{ext} is small), we can assume that $N(\varepsilon)$ is constant in the range $\left(\varepsilon_F - \frac{\Delta E}{2}, \varepsilon_F + \frac{\Delta E}{2}\right)$ and equal to $N(\varepsilon_F)$. From Eq. (6.2) we then obtain

$$m = N(\varepsilon_F)\Delta E \ , \tag{6.5}$$

and from Eq. (6.4) we then obtain

$$E_b = E_b^{NM} + \frac{1}{4} N(\varepsilon_F)(\Delta E)^2 = E_b^{NM} + \frac{1}{4}\frac{1}{N(\varepsilon_F)} m^2 \ . \tag{6.6}$$

Note that the last term is positive and therefore band energy disfavors magnetism.

In addition to the band energy Stoner considered the exchange contribution to the energy. The exchange energy is a result of the fact that electrons that interact with themselves by Coulomb forces are fermions and therefore must satisfy Pauli exclusion principle. This contribution to energy favors parallel spins as Pauli exclusion principle requires them to avoid each other which minimizes the Coulomb interaction. In analogy to the Weiss model, Stoner introduced a molecular field that represents exchange interaction. The molecular field is assumed to be proportional to magnetization and given by $H_m = Im$ where I is a Stoner parameter. The exchange energy is then given by

$$E_{ex} = -\int H_m dm = -\frac{1}{2} I m^2 \ . \tag{6.7}$$

The total energy is then a sum of band energy, exchange energy and the Zeeman energy

$$E_{tot} = E_b^{NM} + \frac{1}{4}\frac{1}{N(\varepsilon_F)} m^2 - \frac{1}{2} I m^2 - \mu_B H_{ext} m \ . \tag{6.8}$$

Here μ_B is the Bohr magneton. The ground state magnetization can be found by minimizing the total energy with respect m

$$m = \frac{2N(\varepsilon_F)\mu_B H_{ext}}{1-2N(\varepsilon_F)I} \quad . \tag{6.9}$$

It follows that magnetic susceptibility is given by

$$\chi = \mu_B \frac{dm}{dH_{ext}} = \frac{2\mu_B^2 N(\varepsilon_F)}{1-2N(\varepsilon_F)I} \quad . \tag{6.10}$$

Note that when the Stoner condition

$$2N(\varepsilon_F)I > 1 \quad . \tag{6.11}$$

is satisfied the susceptibility is negative indicating that the paramagnetic state is unstable with respect to creation of nonzero magnetization and therefore the system is ferromagnetic.

The Stoner criterion is more likely to be satisfied in the materials with large DOS at the Fermi level. This requires partially filled nondispersive bands which usually have d or f characters. Indeed, most of known metallic magnets, like Fe or Gd, have partially filed d or f states at the Fermi level.

The Stoner parameter represents the strength of the effective interaction between electrons. This can be shown explicitly if we represent electronic correlations by the Hubbard term [11]

$$E_U = U \sum_i n_{i+} n_{i-} \, . \tag{6.12}$$

Here index *i* represents quantum numbers of some localized atomic-like basis and *U* is an on-site effective (screened) Coulomb interaction parameter. Applying Hartree-Fock approximation we obtain [11]

$$E_U = U\left(\frac{n^2}{4} - m^2\right). \tag{6.13}$$

The second term in Eq. (6.13) is similar to the exchange energy given by Eq. (6.7). Therefore the electron correlation U is additive to the Stoner parameter I.

When the Stoner criterion is satisfied, one can find the equilibrium magnetization by minimizing the total energy which is a sum of the exchange energy given by Eq. (6.7) and the band energy given by Eq. (6.4). In contrast to the above description, however, one needs evaluate (6.4) by taking into account the energy dependence of the paramagnetic DOS in the neighborhood of the Fermi energy [9]. One can then show the following relation [9]

$$I = \frac{\Delta E}{m}\ . \tag{6.14}$$

Here *m* is an equilibrium magnetization and ΔE is the corresponding (exchange) splitting of the DOS between two spin states. Eq. (6.14) can be used to find the Stoner parameter from the results of spin polarized *ab initio* calculations.

Alternatively, the Stoner parameter can be calculated directly from first principles [12]. Using such calculated values of the Stoner parameter as well as paramagnetic DOS it was found that the Stoner criterion (6.11) correctly predicts presence or absence of magnetism in most of metals [12].

6.3 Calculation methodology

We consider $(SrTiO_3)_n/(LaAlO_3)_m$ superlattices (here *n* and *m* are the numbers of monolayers of $SrTiO_3$ and $LaAlO_3$ films, respectively) with m = 3 and n = 3, 5, 7, 9. The odd values of *n* and *m* cause that both $SrTiO_3$ and $LaAlO_3$ films are nonstoichiometric and that resulting superlattices are symmetric, i.e., they have a mirror symmetry plane perpendicular to the "growth" direction. This requires both interfaces to be identical and here we consider the LaO/TiO_2 n-type interface. On the other hand, nonstoichiometricity of the $LaAlO_3$ film introduces extra electron in the system which allows us to study the magnetic properties of the 2DEG gas regardless of its origin (see Chapter III for discussion of this approach).

We study the atomic and electronic structure of the superlattices using density functional theory [13, 14] within the Perdew-Burke-Ernzerhof (PBE) generalized gradient approximation (GGA) [15] for the exchange correlation potential. Further, electronic correlations were included using GGA+U method [16, 17] with U = 5eV and J = 0.9eV. We solve the Kohn-Sham equations using the projector augmented wave method [18, 19] implemented in the Vienna *Ab-Initio* Simulation Package (VASP) [20, 21]. The in-plane lattice constant was fixed to the average value of the experimental lattice constants of $LaAlO_3$ (3.789 Å) and $SrTiO_3$ (3.905 Å). The resulting supercell is tetragonal with $a = b = 3.847$ Å and the *c/a* ration was set to $(n + m)/2$. The ionic positions within such supercell were fully relaxed. The energy cutoff for the plane wave expansion was set to 500 eV. We used k-point mesh of $8\times8\times\max(1,8/N)$ and $12\times12\times\max(1,12/N)$ for relaxation and density of states (DOS) calculations, respectively.

Here *N* is the number of unit cells perpendicular to the interface. Forces on each atom were converged to < 20 meV/Å.

6.4 Results

Both for GGA and GGA+U strong ionic relaxations were found near the interface for all considered superlattices in agreement with earlier calculations [22]. Mainly, they have a form of buckling distortion of the interfacial TiO_2 layer in which negatively charged O ions are displaced toward $LaAlO_3$ film while positively charged Ti ions move away from the $LaAlO_3$ film. As it produces an electric dipole that screens electric field produced by the positively charged $LaAlO_3$ film, this distortion originates mainly from electrostatic interactions.

First, we consider the electronic structure of the paramagnetic 2DEG at the LaO/TiO_2 interface as a function of the $SrTiO_3$ thickness using GGA. We find that the conduction band is partially occupied and that the number of the conduction electrons is 0.5 electrons per interface, as obtained from the integrated density of states. This agrees with the fact that we used nonstoichiometric film of $LaAlO_3$. In agreement with previous works [22-24], the conduction electrons occupy Ti-3*d* conduction states. We find that, as thickness of $SrTiO_3$ increases, the conduction electrons are distributed to all Ti atoms inside the $SrTiO_3$ slab, rather than being confined only to the Ti atoms at interfaces. This behavior is different from that in $(LaTiO_3)_m/(SrTiO_3)_n$ superlattices where the electron gas was found to be localized within a couple of monolayers near the interface [25]. The 2DEG

remains also delocalized over the $SrTiO_3$ film even when electronic correlations are included by GGA+U method.

Table 6.1: Magnetic moments on the interface Ti atom (m_{Ti}), magnetization of the unit cell (m), the exchange splitting (ΔE), and the parameter $2N(\varepsilon_F)I$ entering the Stoner criterion (6.11) for $(LaAlO_3)_3/(SrTiO_3)_n$ superlattices with different $SrTiO_3$ layer thickness (n) calculated within PBE (U =0).

n	m_{Ti} [μ_B]	m [μ_B]	ΔE [eV]	$2N(\varepsilon_F)I$
3	0.21	0.53	0.29	1.17
5	0.07	0.22	0.10	0.53
7	0.023	0.10	0.03	0.34
9	0.016	0.07	0.02	0.35

As discussed in the Introduction, some experiments [1] suggest that the Ti-3*d* electrons localized at the $LaAlO_3/SrTiO_3$ interfaces align ferromagnetically leading to magnetic behavior at low temperatures. In order to understand the origin of the magnetism we perform spin-polarized calculations of the electronic structure of $(LaAlO_3)_m/(SrTiO_3)_n$ superlattices having LaO/TiO_2 interfaces. For n=3 $SrTiO_3$ film, we

find within GGA that the 2DEG becomes magnetic, with a magnetic moment of 0.2 μ_B on Ti atoms. However, as is evident from Table 6.1, with increasing the $SrTiO_3$ thickness this magnetic moment decreases and disappears.

Fig. 6.3a shows the majority- and minority-spin density of states (DOS) for the Ti atom at the interface for different thicknesses of $SrTiO_3$. As is seen, the exchange splitting ΔE decreases rapidly with $SrTiO_3$ thickness: it has a maximum ΔE=0.29 eV for 3 monolayers (ML) and practically vanishes for 7 MLs of $SrTiO_3$ (see Table 6.1). In order to understand this behavior we employ the Stoner model introduced in Section 6.2.

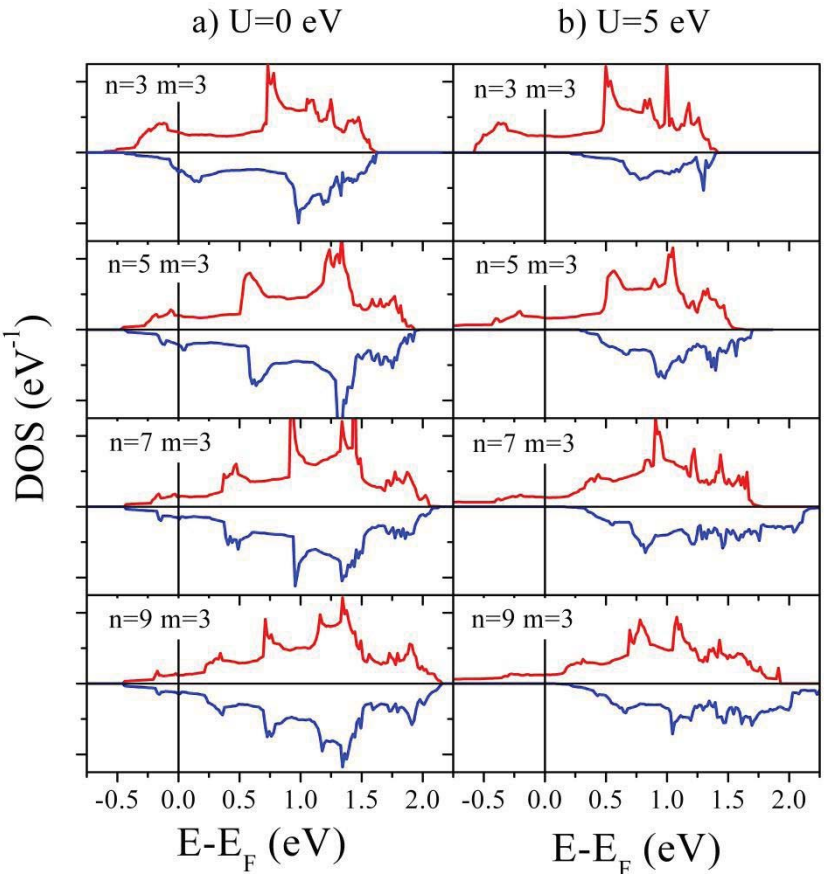

Figure 6.3: Density of states for majority- and minority-spin electrons on the Ti atom at the interface for $(LaAlO_3)_3/ (SrTiO_3)_n$ superlattices. a) U=0, b) U=5 eV. The Fermi energy is denoted by the vertical solid line.

Using Eq. (6.14) and values of ΔE and m obtained from the first-principles calculation for the $(LaAlO_3)_3/(SrTiO_3)_3$ superlattice we find $I = 0.725\,\text{eV}$. Assuming that this value is independent of $SrTiO_3$ thickness in the superlattice, the parameter $2N(\varepsilon_F)I$ entering the Stoner criterion (6.11) can then be calculated for each thickness of $SrTiO_3$. The results are shown in Table 6.1. It is seen that the decay of magnetism in the system is

associated with the violation of the Stoner criterion. Thus, the disappearance of the magnetic moment on the Ti atoms, with the increasing $SrTiO_3$ thickness, is caused by the delocalization of the electron gas that is spread over all the Ti atoms in the $SrTiO_3$, resulting in the decrease of $N(\varepsilon_F)$.

Table 6.2: Magnetic moments on the interface Ti atom (m_{Ti}), magnetization of the unit cell (m), the exchange splitting (ΔE), and the parameter $2N(\varepsilon_F)I$ entering the Stoner criterion (6.11) for $(LaAlO_3)_3/ (SrTiO_3)_n$ superlattices with different $SrTiO_3$ layer thickness (n) calculated within GGA+U with $U = 5$ eV.

n	m_{Ti} [μ_B]	m [μ_B]	ΔE [eV]	$2N(\varepsilon_F)I$
3	0.41	0.996	1.17	7.56
5	0.26	0.999	0.87	3.44
7	0.17	0.995	0.75	2.24
9	0.16	1.006	0.57	2.31

The Ti-3*d* bands play an essential role in the conducting and magnetic properties of $LaAlO_3/SrTiO_3$ superlattices. Due to the localized nature of the 3*d* states, a proper treatment of the on-site Coulomb interaction between electrons is required. Using the

GGA+*U* approximation, we find that the inclusion of the on-site Coulomb interaction with a moderate value of *U*=5eV leads to half-metallicity of the 2DEG in the heterostructures. This is evident from Fig. 6.3b which shows the spin-dependent DOS on the interface Ti atom for different thicknesses of $SrTiO_3$, indicating a zero minority-spin DOS at the Fermi energy. In addition, the on-site Coulomb interaction stabilizes magnetism. As is seen from Table 6.2, for all $SrTiO_3$ thicknesses the calculated GGA+U magnetic moment of the unit cell is about 1 μ_B. The enhancement of magnetism by the GGA+U magnetism is a result of the fact that addition of Hubbard U increases the onsite Coulomb interaction which, as discussed in Section 6.2, increases the Stoner parameter.

6.5 Conclusions

In conclusion, we have studied magnetism and conducting properties of nonstoichiometric $LaAlO_3/SrTiO_3$ (001) superlattices for different thickness of $SrTiO_3$. We found that nonstoichiometricity of the $LaAlO_3$ film causes a partial occupation of the Ti-3*d* conduction band in $SrTiO_3$. For the smallest $SrTiO_3$ thickness the system becomes magnetic, however, the magnetism disappears as the thickness of $SrTiO_3$ increases. The Stoner model predicts that the delocalization of the electron gas over the $SrTiO_3$ thickness reduces the magnetic moment. Taking into account electron-electron correlations within the GGA+U method, we found that the on-site Coulomb interaction stabilizes the magnetization and make the 2DEG half-metallic.

References

[1] A. Brinkman, *et al.*, Nature Mater. **6**, 493 (2007).

[2] M. van Zalk *et al.*, arXiv.org0806.4450 (2008).

[3] M. Ben Shalom *et al.* Phys. Rev. B **80**, 140403 (2009).

[4] N. Reyren, *et al.*, Science **317**, 1196 (2007).

[5] R. Pentcheva and W. E. Picket, Phys. Rev. B **74**, 035112 (2006).

[6] R. Pentcheva and W. E. Picket, Phys. Rev. B **78**, 205106 (2008).

[7] Z. Zhong and P. J. Kelly, Europhys. Lett. **84**, 27001 (2008).

[8] K. Janicka, J. P. Velev, and E. Y. Tsymbal, J. Appl. Phys. **103**, 07B508 (2008).

[9] P. Mohn, *Magnetism in the Solid State: an Introduction*, Springer (2006).

[10] E. C. Stoner, Proc. R. Soc. **165A**, 372 (1938).

[11] P. Fazekas, *Lecture Notes on Electron Correlations and Magnetism*, World Scientific, Singapore (1999).

[12] J. F. Janak, Phys. Rev. B, 16, 255 (1977).

[13] P. Hohenberg and W. Kohn, Phys. Rev. **136**, 864B (1964).

[14] W. Kohn and L. Sham, Phys. Rev. **140**, 1133A (1965).

[15] J. P. Perdev, K. Burke, and M. Ernzerhof, Phys. Rev. Lett. **77**, 3865 (1996).

[16] V. I. Anisimov, J. Zaanen, and O. K. Andersen, Phys. Rev. B 44, 943 (1991).

[17] A. I. Liechtenstein, V. I. Anisimov, and J. Zaanen, Phys. Rev. B 52, R5467 (1995).

[18] P. E. Blöchl, Phys. Rev. B **50**, 17953 (1994).

[19] G. Kresse and D. Joubert, Phys. Rev. B **59**, 1758 (1999).

[20] G. Kresse and J. Hafner, Phys. Rev. B **48**, 13115 (1993).

[21] G. Kresse and J. Furthmüller, Phys. Rev. B **54**, 11169 (1996).

[22] M. S. Park, S. H. Rhim, and A. J. Freeman, Phys. Rev. B **74**, 205416 (2006).

[23] R. Pencheva and W. E. Pickett, Phys. Rev. B **74**, 035112 (2006).

[24] R. Pencheva and W. E. Pickett, Phys. Rev. Lett. **99**, 016802 (2007).

[25] Z. S. Popovic and S. Satpathy, Phys. Rev. Lett. **94,** 176805 (2005).

Chapter 7 Effect of polar interfaces and two-dimensional electron gas on thin-film ferroelectricity.

In this chapter we apply the first principles and model calculations to investigate the ferroelectric stability of thin-film ferroelectrics that form polar interfaces at which a two-dimensional electron gas (2DEG) is present [1]. As a representative model, we consider a TiO_2-terminated $BaTiO_3$ film with LaO monolayers at the two interfaces. We find that the polar interfaces create an intrinsic electric field that is screened by the 2DEG that decays into the $BaTiO_3$ film. Three types of heterostructures were considered (Vacuum/LaO/$BaTiO_3$/LaO, LaO/$BaTiO_3$, and $SrRuO_3$/LaO/$BaTiO_3$/LaO) in which different boundary conditions lead to different 2DEG density.

We find that the intrinsic electric field forces ionic displacements in $BaTiO_3$ to produce the electric polarization directed into the interior of the $BaTiO_3$ layer. This creates a ferroelectric dead layer near the interfaces that is non-switchable and thus detrimental to ferroelectricity. We show that the effect is stronger for a larger effective ionic charge at the interface and longer screening length due to a stronger intrinsic electric field that penetrates deeper into the ferroelectric. The predicted mechanism for a ferroelectric dead layer at the interface controls the critical thickness for ferroelectricity in systems with polar interfaces.

7.1 Introduction

According to the polar catastrophe model the 2DEG at the $SrTiO_3/LaAlO_3$ interface is a result of electronic reconstruction in the form of charge transfer from the $LaAlO_3$ surface to the interface. This electronic reconstruction removes the polar catastrophe caused by alternating charged layers of the polar $LaAlO_3$ film that accumulate diverging electrostatic potential. These electrostatic arguments suggest that there is nothing special about $SrTiO_3$ and $LaAlO_3$ and that, in principle, we can expect 2DEG to form at any interface between polar and nonpolar systems as long as the band gap of the nonpolar system is not too large so that the energy cost for electronic reconstruction is relatively small. In particular, 2DEG was predicted to form at the interfaces involving ferroelectric materials [2, 3].

Ferroelectric materials that are characterized by a switchable macroscopic spontaneous polarization have attracted significant interest due to their technological applications in ferroelectric field-effect transistors and nonvolatile random access memories [4-6]. To increase the capacity of the storage media, it becomes essential to bring ferroelectricity into the nanometer scale. Much experimental and theoretical effort has been devoted to determine the critical thickness of ferroelectric thin films and elucidate its origin. Based on early experiments it was believed that the ferroelectricity vanishes below a critical thickness of a few tens of nm [7] due to the depolarizing field produced by polarization charges on the two surfaces of the ferroelectric film [8]. There is a depolarizing field in a ferroelectric film placed between two metal electrodes due to incomplete screening which is inversely proportional to the thickness of the ferroelectric.

As a result, there is a critical thickness for a ferroelectric below which depolarizing field becomes too large resulting in the suppression of ferroelectricity. Recent experimental and theoretical findings demonstrate, however, that ferroelectricity persists down to a nanometer scale [9]. In particular, it was discovered that in organic ferroelectrics ferroelectricity can be sustained in thin films of monolayer thickness [10]. In perovskite ferroelectric oxides ferroelectricity was observed in nm-thick films [11-16]. These experimental results are consistent with first-principles calculations that predict that the critical thickness for ferroelectricity in perovskite films can be as small as a few lattice parameters [17-22]. The existence of ferroelectricity in ultrathin films opens possibilities for novel nanoscale devices, such as ferroelectric [23-29] and multiferroic [30-33] tunnel junctions.

Ferroelectric properties of thin films placed between two metal electrodes to form a ferroelectric capacitor or a ferroelectric tunnel junction are affected by a number of factors. It was demonstrated that in addition to the screening associated with free charges in the metal electrodes [8] there is an important contribution resulting from ionic screening if electrodes are oxide metals, such as $SrRuO_3$ [20]. It was also predicted that the interface bonding at the ferroelectric-metal interfaces influences strongly the ferroelectric state through the formation of intrinsic dipole moments at the interfaces, as determined by the chemical constituents and interfacial metal-oxide bonds [19]. For some interfaces, these dipole moments are switchable and may enhance the ferroelectric instability of the thin film, which is interesting for engineering the electrical properties of thin-film devices [34]. For other interfaces, however the effect of interface bonding is

detrimental and leads to the “freezing” of polar displacements in the interfacial region, thus resulting in a ferroelectrically inactive layer near the interface [19].

Using a ferroelectric material to form a 2DEG is interesting due to a new functionality that allows controlling 2DEG properties. In particular, it was demonstrated that the switching of spontaneous ferroelectric polarization allows modulations of the carrier density and consequently the conductivity of the 2DEG [2, 3]. This effect occurs due to the screening charge at the interface that counteracts the depolarizing electric field and depends on polarization orientation. A necessary condition for such a new functionality is the ability of a ferroelectric polarization to switch involving a nm-thick region adjacent to the interface where the 2DEG is formed. However, the polar interface which is required for producing a 2DEG [35] may affect the ferroelectric stability due to the electric field associated with the polar interface. This intrinsic electric field is determined by the electron charge distributed near the interface to screen the ionic charge of the interfacial plane and penetrates into the ferroelectric. The intrinsic electric field is detrimental to ferroelectricity due to pinning ionic displacements near the interface that prevents their switching. These arguments indicate the important role of polar interfaces in ferroelectric stability and serve as the motivation for the present study. The importance of this issue also follows from the fact that polar interfaces may occur in ferroelectric capacitors and tunnel junctions. For example, $A^{1+}B^{5+}O_3$ perovskite ferroelectrics (such as $KNbO_3$) have alternating charged monolayers of $(AO)^{-}$ and $(BO_2)^{+}$ along the [001] direction so that the (001) surface is expected to be polar. In addition, metal oxide electrodes may have charge uncompensated atomic planes along the growth direction

(such as $La_{2/3}Sr_{1/3}MnO_3(001)$), so that epitaxially grown films may produce polar interfaces.

7.2 Computational methodology

We consider three types of heterostructures: Vacuum/LaO/$(BaTiO_3)_m$/LaO, LaO/$(BaTiO_3)_n$, and $(SrRuO_3)_{5.5}$/LaO/$(BaTiO_3)_m$/LaO, where m = 8.5 and n = 8.5, 14.5 or 21.5. Here the growth direction is along (001) direction which we choose to be z axis. We impose periodic boundary conditions and assume that $BaTiO_3$ is TiO_2-terminated at both interfaces. For all heterostructures we set the in-plane lattice constant to be equal to the theoretical bulk lattice constant of $SrTiO_3$, *i.e.* a = 3.871 Å. This choice is motivated by the fact that typically oxide heterostructures are grown on a $SrTiO_3$ substrate.

We perform first principles electronic structure calculations based on the density functional theory [35, 36] within the local density approximation (LDA) [37]. We use the projected augmented wave (PAW) method [38] as implemented in the Vienna Ab-Initio Simulation Package (VASP) [39]. The plane-wave energy cutoff is set to 500eV and we use 8×8×1 Monkhorst-Pack k-point mesh [40]. Ferroelectric states of the superlattices are obtained by starting from the displacement pattern according to the tetragonal soft mode of bulk $BaTiO_3$ with polarization pointing along the growth direction and relaxing all the ions until the forces on the ions are less 20 meV/Å.

The ferroelectric polarization of the whole system is calculated using the Berry's phase method [41] while the local polarization distribution is estimated using the model

based on the Born effective charges [42]. In the latter case we compute the local polarization $P(z)$ by averaging over the z-dependent displacements in the $BaTiO_3$ primitive unit cell using equation $P(z) = \frac{e}{\Omega}\sum_{m=1}^{N} Z_m^* \delta u_m$. Here N is the number of atoms in the primitive unit cell, δu_m is the change of the position vector of the m-th atom, and Ω is the volume of the unit cell. We use the Born effective charges Z_m^* as 2.77, 7.25, -2.15, -5.71 for Ba, Ti, $O_\perp$ and $O_\parallel$ ions respectively [43]. Using this approach the polarization of the strained (with an in-plane lattice parameter of 3.871 Å as in the considered heterostructures) bulk $BaTiO_3$ is calculated to be 0.27/m^2, which is in excellent agreement with the rigorous result of the Berry phase method, i.e. 0.26 C/m^2. We note that the method based on the Born effective charges calculated for bulk ferroelectrics cannot provide a quantitatively accurate description of the local polarization distribution in heterostructures due to the effects of interfaces and local fields which do not exist in the bulk. Nevertheless, we find this approach valuable for a semi-quantitative estimate of the polarization behavior and comparison with our phenomenological model (see Section 7.5).

7.3 Electronic structure

We find that in all the structures the presence of the interfacial LaO donor monolayer produces an extra valence charge that resides near the interface, partly or fully leaking into the $BaTiO_3$ layer. The latter fact is evident from Fig. 7.1, which shows the density of states (DOS) projected onto the 3d-orbitals of Ti atoms located at the left and

right interfaces (solid lines) and in the middle of the $BaTiO_3$ layer (shaded area) for the three heterostructures. There are occupied states at and below the Fermi level (placed at zero energy in Fig. 7.1), the density of which decreases with the distance from the interface in the interior of $BaTiO_3$. The attenuation length depends on the state energy in the band gap. Typically the shortest decay length corresponds to energies close to the middle of the gap while at the band gap edges, adjacent to the conduction band minimum or the valence band maximum, the decay length diverges due to the imaginary part of the complex wave vector tending to zero [44]. The average decay length is about 1nm for all the three heterostructures similar as for the $LaAlO_3/SrTiO_3$ system [45]. We note the DOS at the Fermi energy decays at a larger scale and involves metal-induced gap states [45], so that a much larger thickness of $BaTiO_3$ is required to approach a zero DOS. This is discussed in detail in Appendix 7A, where we analyze the band alignment for the $LaO/(BaTiO_3)_{21.5}$ system. The total leakage charge can be calculated by integrating the total DOS lying within the band gap of $BaTiO_3$ up to the Fermi energy. We find for the $Vacuum/LaO/(BaTiO_3)_{8.5}/LaO$, $LaO/(BaTiO_3)_{8.5}$, and $(SrRuO_3)_{5.5}/LaO/(BaTiO_3)_{8.5}/LaO$ heterostructures that this charge is equal to $-1e$, $-0.5e$, and $-0.26e$ per unit cell area respectively.

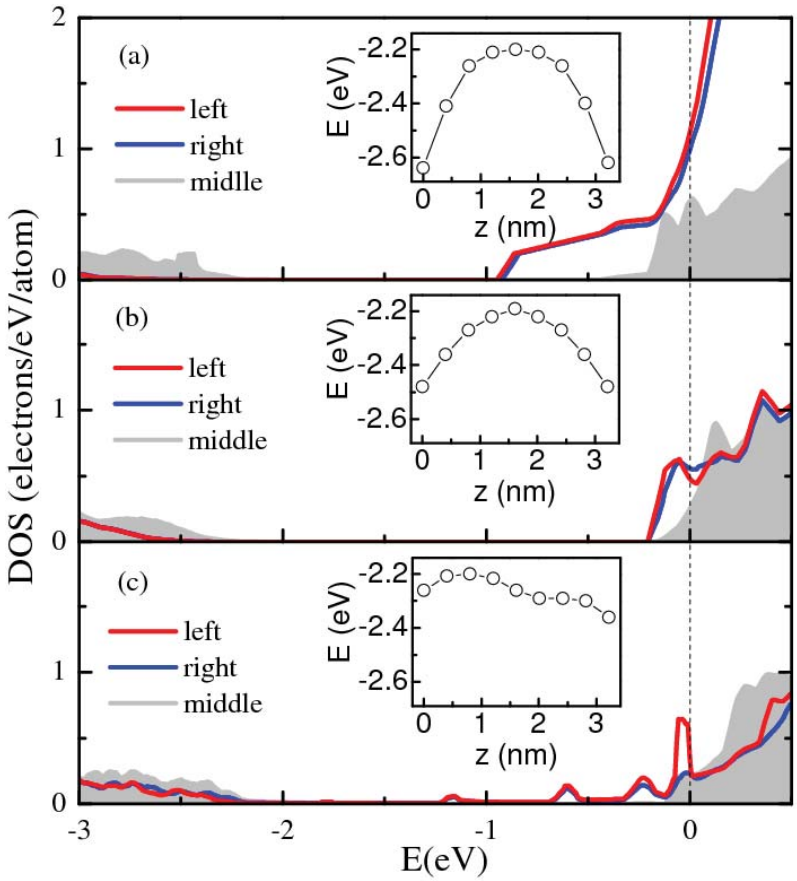

Figure 7.1: Density of states (DOS) projected onto the 3*d* states of Ti atoms located at the left and right interfaces (solid lines) and in the middle of the $BaTiO_3$ layer (shaded area) for (a) Vacuum/LaO/$(BaTiO_3)_{8.5}$/LaO, (b) LaO/$(BaTiO_3)_{8.5}$, and (c) $(SrRuO_3)_{5.5}$/LaO/$(BaTiO_3)_{8.5}$/LaO heterostructures. The Fermi level lies at zero energy and denoted by the dashed line. The insets show the valence band maximum (VBM) with respect to the Fermi energy within the $BaTiO_3$ layer as a function of *z*.

As is evident from the DOS plotted in Fig. 7.1a, for a Vacuum/LaO/$(BaTiO_3)_{8.5}$/LaO heterostructure, there is a significant shift of the valence

band maximum (VBM) in the middle of $BaTiO_3$ layer as compared to the interfaces. This is an indication of the electrostatic potential change in the insulator and hence an intrinsic electric field. We show the variation of the electrostatic potential energy across the $BaTiO_3$ layer in the inset of Fig. 7.1a by plotting the VBM energy as a function of position *z* (measured in unit cells) within $BaTiO_3$. Note that almost symmetric variation of the electrostatic potential is the indication of the absence of ferroelectric polarization in $BaTiO_3$ which is expected to break the symmetry. A significant increase in the electrostatic potential energy at the two interfaces that is seen from the inset indicates the presence of the intrinsic electric field pointing away from the interfaces. This field originates from the positively charged LaO layer. The magnitude of the field close to the interfaces is about 0.5 V/nm and as we go away from the interface the field is screened by the conduction electrons within the screening length of about 1 nm. This intrinsic electric field is shown schematically in Fig. 7.2.

A similar behavior is present in a $LaO/(BaTiO_3)_{8.5}$ heterostructure. In this case, however, as seen from the inset in Fig. 7.1b, the electric field is reduced by a factor of two, as compared to the $Vacuum/LaO/(BaTiO_3)_{8.5}/LaO$ system. This reduction is a consequence of the fact that the positive charge at the $(LaO)^+$ layer is partially compensated by negative charge of -0.5*e* per unit interface residing on the other side of the interface. The electric field is still sufficiently large to not allow for ferroelectric polarization to develop for the 8.5 unit cell thick $BaTiO_3$ layer, as follows from the almost symmetric energy profile seen in the inset of Fig. 7.1b.

Figure 7.2: Schematic illustration of the charge distribution and the intrinsic electric field in a $BaTiO_3$ film terminated with positively charged $(LaO)^+$ monolayers at the left and right interfaces. A gradient shadow region indicates the screening charge penetrating into $BaTiO_3$. Blue arrows indicate the direction of the intrinsic electric field that has a tendency to pin the local polarization along the field direction.

The situation changes for a $(SrRuO_3)_{5.5}/LaO/(BaTiO_3)_{8.5}/LaO$ heterostructure. Here most of electrons are transferred to the $SrRuO_3$ film and only -0.26*e* per interface leaks into $BaTiO_3$. Consequently, the charge of -0.74*e* per interface residing at the $SrRuO_3$ film strongly compensates the positive charge at the $(LaO)^+$ layer and significantly reduces the intrinsic electric field in the $BaTiO_3$ layer allowing ferroelectric polarization to develop in the system, as we will see below. An indirect indication of this fact is a complex electrostatic energy profile across the $BaTiO_3$ layer (see the inset in Fig. 7.1c) which in addition to the intrinsic electric field includes contributions from the depolarizing field created by a non-uniform polarization and the associated screening charge.

We note that the amount and the penetration depth of the electron charge into $BaTiO_3$ are largely determined by the position of the Fermi energy with respect to the bottom of the conduction band of $BaTiO_3$. The latter is controlled by the conduction band bending due to the electrostatic potential associated with the screening charge that places the conduction band minimum at a certain position above the Fermi energy. Therefore, the well-known problem of LDA to underestimate the band gap of insulator and predict an incorrect band offset between metal and insulators does not affect significantly the predicted results.

7.4 Atomic structure and polarization

The effect of the intrinsic electric field at the interface on ferroelectric polarization is evident from polar atomic displacements in the studied systems which are correlated with a ferroelectric instability. Figs. 7.3a,b,c show the displacements of cations (Ba and Ti) with respect to oxygen anions in the $BaTiO_3$ layer for Vacuum/LaO/$(BaTiO_3)_{8.5}$/LaO, LaO/$(BaTiO_3)_{8.5}$, and $(SrRuO_3)_{5.5}$/LaO/$(BaTiO_3)_{8.5}$/LaO heterostructures respectively. As seen from Fig. 7.3a, the displacements profile is nearly inversion-symmetric and, although the displacements are very large (about 0.2 Å) close to the interfaces, they have opposite sign. This behavior is the consequence of the intrinsic electric field pointing away from the interfaces that forces the polarization to be pinned in the same direction. The LaO/$(BaTiO_3)_{8.5}$ system exhibits a similar displacements profile, although the magnitude of the displacements is somewhat reduced at the interface due to reduces value of the intrinsic electric field (Fig. 7.3b). For the

$(SrRuO_3)_{5.5}/LaO/(BaTiO_3)_{8.5}/LaO$ system the intrinsic electric field is further reduced that allows a ferroelectric polarization to develop. This follows from the asymmetric polarization profile in Fig. 7.3c with a larger portion of electric dipoles pointing in the positive direction along the *z* axis (i.e. from left to right interface).

Using the model based on Born effective charges we evaluated the local polarization distribution within the $BaTiO_3$ layer for all considered heterostructures. The results are displayed in Figs. 7.3d-f (squares). It is seen that for $Vacuum/LaO/(BaTiO_3)_{8.5}/LaO$ (Fig. 7.3d) and $LaO/(BaTiO_3)_{8.5}$ (Fig. 7.3e) heterostructures the polarization profiles are nearly inversion-symmetric resulting in very low average polarization values: 0.029 and 0.037 C/m^2 for the two systems respectively. For the $(SrRuO_3)_{5.5}/LaO/(BaTiO_3)_{8.5}/LaO$ heterostructure (Fig. 7.3f) the ferroelectric polarization is more pronounced (the average value is 0.09 C/m^2) due to the screening of the depolarizing field in the $SrRuO_3$ electrodes. Nevertheless, even in this case the presence of the intrinsic electric field associated with the polar interfaces force the dipole moments in $BaTiO_3$ to be pointed away from the interfaces, resulting in a ferroelectric dead layer as discussed below.

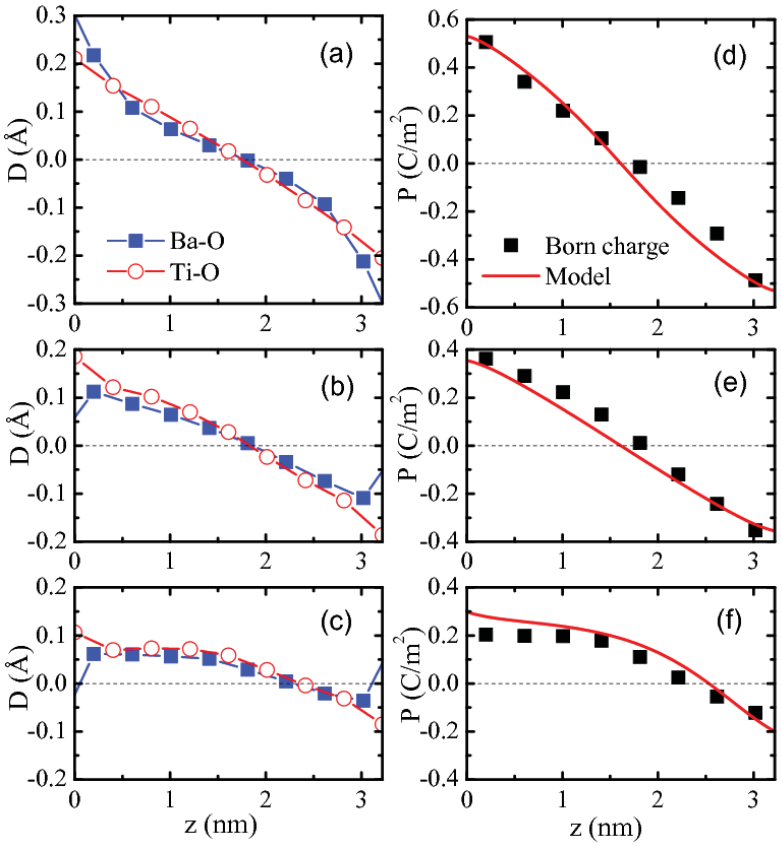

Figure 7.3: Displacements (D) of cations (Ba and Ti) with respect to oxygen anions (a, b, c) and local polarizations (P) (d, e, f) across a $BaTiO_3$ layer in Vacuum/LaO/$(BaTiO_3)_8$/LaO (a, d), LaO/$(BaTiO_3)_{8.5}$ (b, e) and $(SrRuO_3)_{5.5}$/LaO/$(BaTiO_3)_{8.5}$/LaO (c, f) heterostructures. Solid squares and open circles in (a-c) denote Ba-O and Ti-O displacements respectively. In figures (d-f) the local polarizations are obtained using the displacements calculated from first-principles in conjunctions with the Born effective charges (squares) and from the phenomenological model (solid lines).

The presence of a ferroelectric dead layer, i.e. the $BaTiO_3$ region near the interface that does not switch upon ferroelectric polarization reversal, can be seen from the dependence of polar displacements and local polarization distribution as a function of $BaTiO_3$ thickness. To study this dependence we have performed calculations for $LaO/(BaTiO_3)_n$ heterostructures containing n = 8.5, 14.5 or 21.5 unit cells of $BaTiO_3$ that correspond to $BaTiO_3$ thicknesses t = 3.2, 5.6, 8.4 nm. Since the boundary conditions at the two interfaces are identical, the intrinsic electric field is independent of $BaTiO_3$ thickness. The results are displayed in Figs. 7.4a-f. It is seen that as the $BaTiO_3$ thickness increases, the ferroelectric polarization becomes more stable involving a larger thickness of the $BaTiO_3$ layer. The average polarization of $BaTiO_3$ increases from $\bar{P}$ = 0.029 C/m^2 for t = 3.2 nm to $\bar{P}$ = 0.095 C/m^2 and 0.12C/m^2 for t = 5.6 and 8.4 nm respectively. It is notable, however, that even at a relatively large thickness of 8.4 nm the ferroelectric polarization in the middle of the $BaTiO_3$ layer is 0.21 C/m^2, i.e. it does not reach the respective strained bulk value of 0.27 C/m^2.

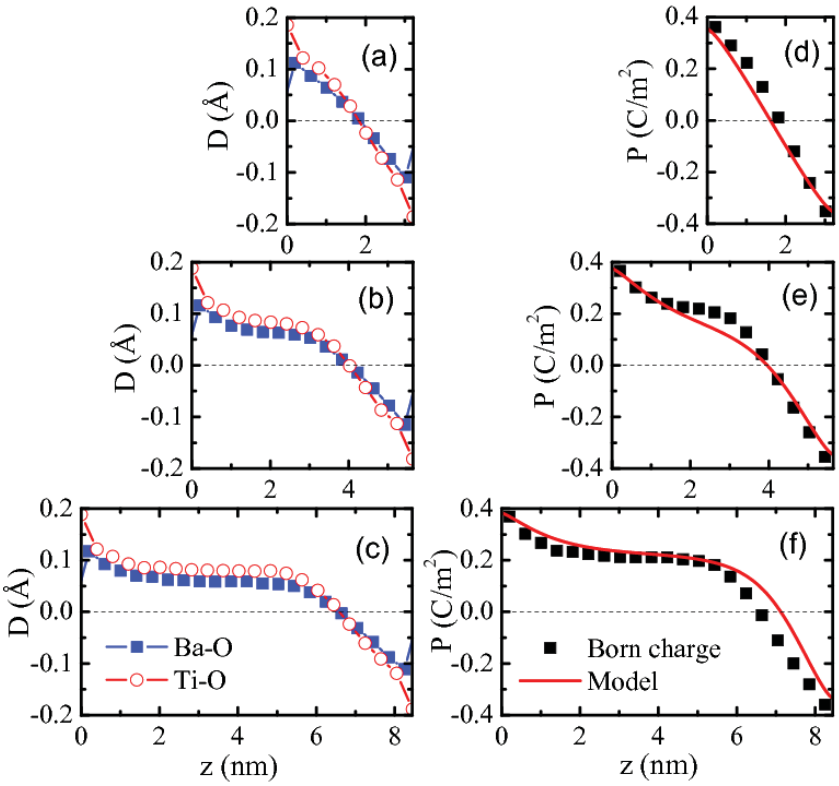

Figure 7.4: Displacements (D) of cations (Ba and Ti) with respect to oxygen anions (a, b, c) and local polarizations (P) (d, e, f) across the $BaTiO_3$ layer in $LaO/(BaTiO_3)_n$ heterostructures containing n = 8.5 (a, d), 14.5 (b, e) or 21.5 (c, f) unit cells of $BaTiO_3$. Solid squares and open circles in (a-c) denote Ba-O and Ti-O displacements respectively. In figures (d-f) the local polarizations are obtained using the displacements calculated from first-principles in conjunctions with the Born effective charges (squares) and from the phenomenological model (solid lines).

The enhancement of polarization at large $BaTiO_3$ thickness does not affect significantly the $BaTiO_3$ region adjacent to the right interface where the polar displacements remain opposite to the spontaneous polarization displacements. From comparison of Figs. 7.4d-f it is seen that the region where the polar displacements are

reversing is almost independent of $BaTiO_3$ thickness and cover about 3 nm thicknesses near the interface. This may be regarded as a ferroelectric dead layer and determines the critical thickness for ferroelectricity in this system.

We note that in the previous calculation of critical thickness for ferroelectricity of a $KNbO_3$ film placed between two metal electrodes [19] the effect of the polar interfaces may also play a role due to the $KNbO_3$(001) layer being comprised of the charged $(KO)^-$ and $(NbO_2)^+$ planes along the [001] direction. The predicted ferroelectric domain wall occurring in the $SrRuO_3/KNbO_3$ heterostructure may partly be caused by an intrinsic electric field occurring at the polar interface in this system.

7.5 Phenomenological model

In order to further investigate the effect of the intrinsic electric field on ferroelectric polarization of the $BaTiO_3$ film we introduced a phenomenological model based on the Landau-Ginzburg-Devonshire theory [46, 47]. For this purpose it is convenient to introduce the notion of *effective ionic charge* which is a sum of the positive charge at the LaO monolayer and a negative electron charge distributed on the other side of the interface. As discussed above, the first principles calculations find ionic charges equal to $+e$, $+0.5e$, and $+0.26e$ per lateral unit cell area for Vacuum/LaO/$(BaTiO_3)_m$/LaO, LaO/$(BaTiO_3)_n$, and $(SrRuO_3)_{5.5}$/LaO/$(BaTiO_3)_m$/LaO ,respectively. These effective ionic charge creates an *intrinsic electric field* in the $BaTiO_3$ film pointing away from the interface as shown in Fig. 7.2. According to the first principles calculations this field is

screened by the conduction electrons within the screening length of about 1 nm from the interface.

The free energy of a ferroelectric film can be written as [48, 49]

$$F = \int (\frac{A}{2} P^2 + \frac{B}{4} P^4 + \frac{C}{2} (\nabla \cdot P)^2 - E_i P - \frac{1}{2} E_{ds} P) dV + \int \frac{C}{2\delta} \left\{ [P(0) + P_i]^2 + [P(d) - P_i]^2 \right\} dS \tag{7.1}$$

Here $P(z)$ is a ferroelectric polarization, which is assumed to be homogeneous in the x-y plane of the film, P_i is the interface polarization, and E_i is the intrinsic electric field not related to the polarization. The last term in the volume integral represents the self-energy of the depolarizing field E_{ds} that includes screening (see Appendix 7B). Constant A is given by Curie-Weiss law $A = \frac{T - T_C}{C_0 \varepsilon_0}$, where C_0 and T_C are the Curie constant and temperature, and ε_0 is the permittivity of free space. Constant B is given by $B = -A / P_0^2$, where P_0 is the polarization at zero temperature. Constant C is related to A as follows: $C = -A a_0^2$, where a_0 is of the order of lattice spacing [48]. The extrapolation length δ is a phenomenological parameter associated with the derivatives of the $P(z)$ at the interface.

We obtain the intrinsic electric field E_i and depolarizing field E_{ds}, as described in the Appendix 7B, assuming that the free charge that screens the effective ionic charge at the interfaces decays exponentially into the ferroelectric layer with decay length λ and is redistributed between the interfaces to screen the depolarizing field. Variation of the

free energy functional given by Eq. (7.1) over the polarization yields the Euler–Lagrange equation for polarization

$$C\frac{d^2P}{dx^2} = AP + BP^3 - E_i + \frac{1}{2}\frac{2P - R\bar{P} - \overline{RP}}{\varepsilon_f} \tag{7.2}$$

subject to boundary conditions

$$\left(P \mp \delta\frac{dP}{dz}\right)_{z=0,d} = \mp P_i \ . \tag{7.3}$$

In Eq. (7.2) $\bar{P}$ and $\overline{RP}$ are the average polarization $P(z)$ and the average function $R(z)P(z)$ over film thickness, where $R(z)$ is given by Eq. (7B.8). Eq. (7.2) can be solved numerically using an iterative procedure. Numerical calculations suggest that the last term in Eq. (7.2) can be replaced, with reasonable accuracy, by $\frac{P - R\bar{P}}{\varepsilon_f}$ which simplifies the convergence to a self-consistent solution. In particular calculations, we use a set of parameters appropriate for $BaTiO_3$: $T_C = 403K$, $P_0 = 0.27C/m^2$, $C_0 = 1.7\cdot 10^5$, [50] and $a_0 = 0.8nm$ [51, 52]. The dielectric permittivity ε_f originates from the non-ferroelectric lattice modes [53] and for $BaTiO_3$ is assumed to be $\varepsilon_f = 90\varepsilon_0$ [28]. This value describes adequately the depolarizing field in $BaTiO_3$ obtained from first-principles calculations for a $SrRuO_3/BaTiO_3/SrRuO_3$ ferroelectric tunnel junction [32]. In the calculations we use different effective ionic charges σ_i at the $BaTiO_3$ surfaces which enter Eq. (7B.2) for the intrinsic electric field. For the Vacuum/LaO/$BaTiO_3$/LaO system, the effective interface charge σ_i is assumed to be $+e$ per lateral unit cell area, while for LaO/$BaTiO_3$ and

$SrRuO_3$/LaO/$BaTiO_3$/LaO systems lattices they are assumed to be +0.5*e* and +0.26*e* respectively. Other parameters, i.e. λ, δ and P_i, are the adjustable parameters of the model.

The local polarization obtained by numerical solution of the Eq. (7.2) is fitted to the results of the first principles calculations and the model based on Born effective charges. To reduce the number of fitting parameters we fixed λ = 1nm consistent with our first principles results and δ = 1.2nm. The value of $P_i = -0.45 C/m^2$ was fitted and was assumed to be the same for all the structures considered. Different effective ionic charges σ_i at the $BaTiO_3$ surfaces corresponding to different heterostructures were used. Figs. 7.3e-f and 4e-f show results of the fitting by solid lines, demonstrating that the phenomenological model is capable of describing all the major features in the distributions of the local polarization that are obtained from the first-principles displacements combined with the Born effective charges. In particular, the model clearly indicates that the intrinsic electric field associated with polar interfaces pins the atomic displacements near the interfaces and thus is detrimental to ferroelectricity. For a given decay length λ inside the ferroelectric, the larger effective ionic charge at the interface creates a wider ferroelectric dead layer near the interface and thus produces a stronger destructive effect on ferroelectricity.

To obtain a further insight into the effect of the intrinsic electric field on ferroelectricity we have modeled the average polarization of a ferroelectric layer terminated by a polar interface allowing the decay length λ to be a variable parameter. In the simulation we kept all the other parameters to be the same as those for the

LaO/$(BaTiO_3)_n$ heterostructure. Fig. 7.5a shows the resulting average polarization $\bar{P}$ as a function of λ for films of different thicknesses t. It is seen that with increasing decay length the average polarization of the film decreases and at some value of λ it vanishes even for a very thick $BaTiO_3$ layer. This detrimental effect on ferroelectricity originates from the increasing penetration depth of the intrinsic electric field into the ferroelectric layer that broadens a ferroelectrically dead region near the interfaces. On the other hand, when λ tends to zero the pinning electric field near the interfaces vanishes and the average polarization approaches its bulk value as the thickness of $BaTiO_3$ is increasing.

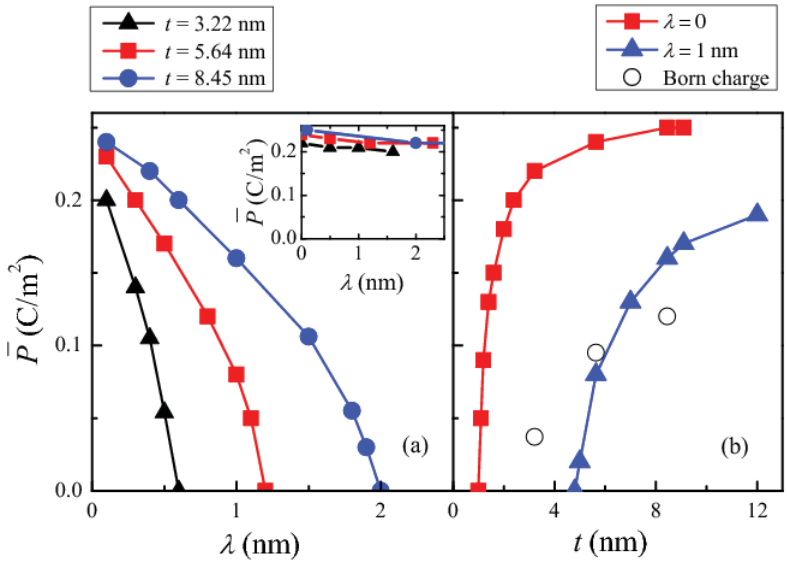

Figure 7.5: Average polarization $\bar{P}$ of a $BaTiO_3$ film (a) as a function of the decay length λ for three film thicknesses t and (b) as a function of the film thickness t for two values of λ calculated within the phenomenological model (solid symbols) and using first-principles calculations and the Born charge model (open symbols). The inset in (a) shows $\bar{P}$ for $E_i = 0$.

The stability of ferroelectric polarization strongly depends on the screening length λ. The latter determines the penetration depth of the screening charge and consequently the electric field into the ferroelectric layer. Increasing the screening length leads to the increase of the critical thickness for ferroelectricity. This statement is confirmed in our model calculations displayed in Fig. 7.5b that show the average polarization as a function of ferroelectric layer thickness t for different λ. In this calculation the magnitude of the charge that screens polarization is kept fixed so that only the penetration depth of the charge that screens the intrinsic electric field is varied. It is seen that the increase of the screening length from $\lambda = 0$ to $\lambda = 1$nm leads to the increase in the critical thickness from about 1 nm to about 5 nm. The latter is qualitatively consistent with our first-principles calculations combined with the model based on the effective Born charges.

We would like to emphasize that the predicted suppression of polarization in our systems is entirely caused by the polar interfaces and the associated intrinsic electric field resulting in a ferroelectric dead layer. Other possible mechanisms detrimental to ferroelectricity such as insufficient screening of polarization charge and the interface bonding do not play a decisive role. The polarization screening due to the redistribution of the free charge between interfaces (see Appendix 7B) is sufficient to maintain the polarization. This fact follows from the calculation we performed within the phenomenological model in which the intrinsic electric field was artificially set equal to zero, i.e. $E_i = 0$, in the free energy given by Eq. (7.1), but other parameters of the model were kept fixed. The calculation of the average polarization with respect to film thickness t predicts no decay of polarization with λ (see the inset in Fig. 7.5a) and the critical thickness for ferroelectricity of about 1 nm (see Fig. 7.5b) consistent with previous first-

principles results [17-20]. We can also rule out the effect of interface bonding as a possible mechanism of suppression of ferroelectricity. If it were due to the interface bonding, then the ferroelectric polarization in the three structures considered would be similar due to the same LaO monolayers terminating $BaTiO_3$. However, the results of our first-principles calculations suggest a very different behavior for the three systems.

Our results are consistent with the stability of ferroelectric $KNbO_3$ in the presence of 2DEG at the $KNbO_3/SrTiO_3$ interfaces predicted earlier [2, 3]. In this case the positive charge at the polar interface is screened by a free electron charge penetrating almost equally both to the $KNbO_3$ and $SrTiO_3$ layers. As follows from symmetry, this implies that only $0.25e$ per interface leak into the $KNbO_3$ with decay length of about 1nm. Due to the same leakage charge and the decay length, the local polarization distribution is expected to be qualitatively similar to that found for the $SrRuO_3/LaO/BaTiO_3/LaO$ heterostructure. This fact is evident from the similarity between displacements shown in Fig. 7.3c and those in Fig. 7.4a of Ref. [3].

7.6 Summary

Based on first-principles calculations and a phenomenological model we have investigated the effect of polar interfaces on the ferroelectric stability of thin-film ferroelectrics using $Vacuum/LaO/BaTiO_3/LaO$, $LaO/BaTiO_3$, and $SrRuO_3/LaO/BaTiO_3/LaO$ heterostructures as representative systems. In all the three systems a LaO monolayer at the interface with a TiO_2-terminated $BaTiO_3$ produces a

polar interface and serves as a doping layer donating an electron at the interface that compensates the ionic charge of the positively charged $(LaO)^+$ monolayer. This interface ionic charge creates an intrinsic electric field at the interface which is screened by the screening electron charge leaking into the $BaTiO_3$ layer within the screening length of about 1 nm from the interface. The three systems considered are different by the amount of the screening charge changing from $-e$ per a lateral unit cell to $-0.5e$ and $-0.26e$ and thus *effective ionic charge* for the Vacuum/LaO/$BaTiO_3$/LaO, LaO/$BaTiO_3$, and $SrRuO_3$/LaO/$BaTiO_3$/LaO systems respectively. Within the screening region the intrinsic electric field forces ionic displacements in $BaTiO_3$ to produce the dipole moments pointing into the interior of the $BaTiO_3$ layer and thus pins the polarization near the interface. This creates a ferroelectric dead layer near the interfaces that is non-switchable and thus detrimental to ferroelectricity. Our first-principles and model calculations demonstrate that the effect is stronger for a system, in which the effective ionic charge at the interface is larger and the screening length is longer resulting in a stronger intrinsic electric field that penetrates deeper into the ferroelectric. The predicted mechanism for a ferroelectric dead layer at the interface controls the critical thickness for ferroelectricity in systems with polar interfaces.

Appendix 7A: Band alignment in LaO/$(BaTiO_3)_{21.5}$ system

Here we analyze the band alignment in LaO/$(BaTiO_3)_{21.5}$ system. Fig. 7.6a shows the calculated density of states (DOS) on the TiO_2 monolayers located at different distances from the LaO monolayers at the interface. A substantial band bending is seen

resulting in the change of the valence band maximum (VBM) and the conduction band minimum (CBM) as a function of *l*. This is due to the variation of the macroscopic electrostatic potential which rigidly shifts the bands with respect to the Fermi energy. The macroscopic electrostatic potential is obtained by performing the macroscopic averaging of the microscopic potential obtained from the supercell calculation that allows filtering out microscopic periodic oscillations in the original data [54, 55]. Fig. 7.6b shows the result of this averaging for the $LaO/(BaTiO_3)_{21.5}$ superlattice, where the planer-averaged electrostatic potential (thin line) and the potential additionally averaged over the $BaTiO_3$ c-lattice constant (i.e. macroscopically averaged) (thick line) are shown as a function of the position *z* within the $BaTiO_3$ layer. We find that the variation of the macroscopic electrostatic potential is consistent with the change in the VBM seen in Fig. 7.6a, as is evident from the respective solid curve plotted in accordance to Fig. 7.6b. This allows us to find the variation of the conduction band minimum (CBM) in $BaTiO_3$ as follows. We add the calculated band gap of the bulk $BaTiO_3$ with the same lattice constant of 2.2eV to the VBM obtained for the TiO_2 monolayer in the middle of $BaTiO_3$ layer. This determines the CBM at this site, which appears to be approximately 0.2 eV above the Fermi energy. Then, we obtain the site variation of the CBM by adding the electrostatic potential difference as shown by the solid curve in the conduction band in Fig. 7.6a. It is clearly seen that CBM below the Fermi energy are confined close to the interface layers.

The approach used here is similar to that applied in Ref. [45], to prove the importance of evanescent states in controlling the confinement width of 2DEG. As seen from Fig. 7.6c the variation in the electrostatic potential shown in Fig. 7.6b is consistent

with the position of the core-like O-2s states. This justifies the method used in Ref. [45] to analyze the variation of the electrostatic potential based on the O-2s states.

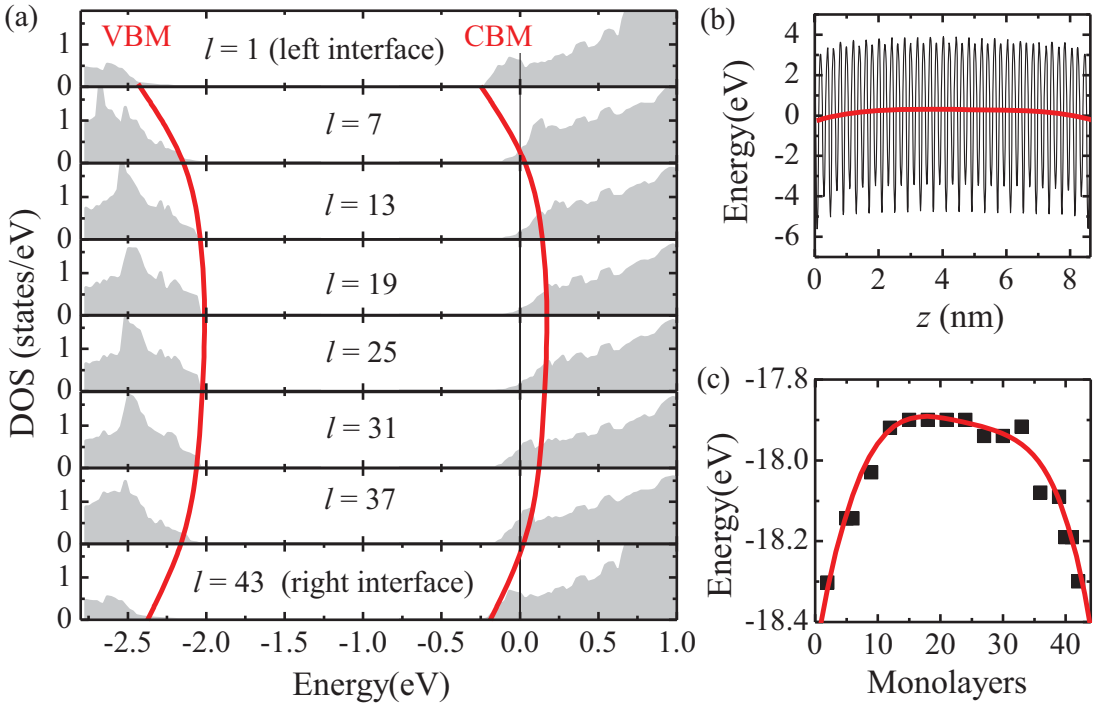

Figure 7.6: Band alignment in LaO/$(BaTiO_3)_{21.5}$ system. (a) Local DOS on TiO_2 monolayers (l) as a function of the energy. The curved line to the left (right) indicates the position of the valence band maxima (conduction band minima) and the vertical solid line denotes the Fermi energy E_F; (b) Planar-averaged electrostatic potential across $BaTiO_3$ (thin line) and the macroscopic electrostatic potential (thick line); (c) Position of the core-like O-2s states for different TiO_2 layers (squares) and the macroscopic electrostatic potential shifted by -18.2 eV (solid line).

Appendix 7B: Intrinsic and depolarizing fields

Here we calculate the intrinsic electric field E_i associated with the surface ionic charge screened by the free electron charge penetrating into the interior of a $BaTiO_3$ layer (see Fig. 7.2) and the depolarizing electric field E_{ds} associated with ferroelectric polarization. We consider a ferroelectric thin film of thickness d and polarization $P(z)$ and assume that there is an effective ionic (positive) charge density σ_i deposited on each of the two interfaces. As was discuss in Section 7.3, this effective ionic charge is different depending on a particular interface. We assume that there is no polarization and field outside the film. Consistent with the Thomas-Fermi model, we assume that a free electron (negative) charge that screens the ionic charge decays exponentially into the $BaTiO_3$ layer with decay length λ. Due to charge conservation the resulting volume charge density is given by

$$\rho_i = -\frac{\sigma_i}{\lambda}\frac{e^{\frac{-z}{\lambda}} + e^{\frac{z-d}{\lambda}}}{1-e^{-\frac{d}{\lambda}}} \quad . \tag{7B.1}$$

The resulting electric field produced by both the interface ionic charge and the screening charge is given by:

$$E_i(z) = \frac{\sigma_i}{\varepsilon_f}\frac{e^{\frac{-z}{\lambda}} - e^{\frac{z-d}{\lambda}}}{1-e^{-\frac{d}{\lambda}}} \quad , \tag{7B.2}$$

where ε_f is the dielectric constant of the ferroelectric at saturation.

The ferroelectric polarization of the film produces the volume polarization charge density $\rho_p = -\frac{dP(z)}{dz}$ and surface polarization charge density at the two interfaces, $\sigma_p(0) = -P(0)$ and $\sigma_p(d) = -P(d)$. The associated (unscreened) depolarizing field is given by

$$E_d(z) = -\frac{P(z)}{\varepsilon_f}, \tag{7B.3}$$

where the dielectric permittivity ε_f originates from the non-ferroelectric lattice modes [53]. This field is partly screened by the redistribution of the free charge density between the two interfaces. Note that this screening of the depolarizing field is different from the screening of the ionic charge located at the interfaces. For simplicity we assume that the screening charge density do not change the shape of the free charge density distribution, but rather adds charge at one interface and removes it at the other interface. Thus the volume screening charge density can be written in the following form:

$$\rho_s = -\frac{\sigma_s}{\lambda}\frac{e^{\frac{-z}{\lambda}} - e^{\frac{z-d}{\lambda}}}{1-e^{-\frac{d}{\lambda}}}, \tag{7B.4}$$

where σ_s is the surface screening charge density and the total screening charge (i.e. the integral of (7B.4) over film thickness) is equal to zero. The associated screening field is

$$E_s = -\frac{\sigma_s}{\varepsilon_f}\frac{1+e^{\frac{-d}{\lambda}} - e^{\frac{-z}{\lambda}} - e^{\frac{z-d}{\lambda}}}{1-e^{\frac{-d}{\lambda}}}. \tag{7B.5}$$

In order to obtain the value of σ_s, we use the short-circuit boundary condition which follow from the periodic boundary condition of the supercell geometry. This condition implies that the electrostatic potential must be equal at the two interfaces, i.e. $\Phi(0) = \Phi(d)$. Using this condition we find

$$\sigma_s = -\bar{P}\frac{1-e^{\frac{-d}{\lambda}}}{1+e^{\frac{-d}{\lambda}}-\frac{2\lambda}{d}+\frac{2\lambda}{d}e^{\frac{-d}{\lambda}}} \quad , \tag{7B.6}$$

where $\bar{P} \equiv \frac{1}{d}\int_0^d P(z)dz$ is the average polarization.

Thus, the net depolarizing field that takes into account the effect of screening is given by

$$E_{ds} = E_d + E_s = \frac{\bar{P}R(z) - P(z)}{\varepsilon_f} \quad , \tag{7B.7}$$

where

$$R(z) = \frac{1+e^{\frac{-d}{\lambda}}-e^{\frac{-z}{\lambda}}-e^{\frac{z-d}{\lambda}}}{1+e^{\frac{-d}{\lambda}}-\frac{2\lambda}{d}+\frac{2\lambda}{d}e^{\frac{-d}{\lambda}}} \quad . \tag{7B.8}$$

This depolarizing field enters the free energy functional given by Eq. (7.1).

References

[1] Y. Wang, M. K. Niranjan, K. Janicka, J. P. Velev, M. Y. Zhuravlev, S. S. Jaswal, and E. Y. Tsymbal, Phys. Rev. B **82**, 094114 (2010).

[2] M. K. Niranjan, Y. Wang, S.S. Jaswal, and E.Y. Tsymbal, Phys. Rev. Lett. **103**, 016804 (2009).

[3] Y. Wang, M. K. Niranjan, S. S. Jaswal, and E. Y. Tsymbal, Phys. Rev. B **80**, 165130 (2009).

[4] M. Dawber, K. M. Rabe, and J. F. Scott, Rev. Mod. Phys. **77**, 1083 (2005).

[5] N. Setter, D. Damjanovic, L. Eng, G. Fox, S. Gevorgian, S. Hong, A. Kingon, H. Kohlstedt, N. Y. Park, G. B. Stephenson, I. Stolitchnov, A. K. Taganstev, D. V. Taylor, T. Yamada, and S. Streiffer, J. Appl. Phys. **100**, 051606 (2006).

[6] J. F. Scott, Science **315**, 954 (2007).

[7] N. A. Spaldin, Science **304**, 1606 (2004).

[8] R. R. Mehta, B. D. Silverman, and J. T. Jacobs, J. Appl. Phys. **44**, 3379 (1973).

[9] C. Lichtensteiger, M. Dawber, and J.-M. Triscone, in *Physics of ferroelectrics: A modern perspective*, Series: Topics in Applied Physics, Vol. **105**, eds. K.M. Rabe, C. H. Ahn, and J.-M. Triscone (Springer, 2007) pp. 305-336.

[10] A. V. Bune, V. M. Fridkin, S. Ducharme, L. M. Blinov, S. P. Palto, A. V. Sorokin, S. G. Yudin, and A. Zlatkin, Nature **391**, 874 (1998).

[11] T. Tybell, C. H. Ahn, and J-M. Triscone, Appl. Phys. Lett. **75**, 856 (1999).

[12] D. D. Fong, G. B. Stephenson, S. K. Streiffer, J. A. Eastman, O. Auciello, P. H. Fuoss, and C. Thompson, Science **304**, 1650 (2004).

[13] C. Lichtensteiger, J. M. Triscone, J. Junquera, and Ph. Ghosez, Phys. Rev. Lett. **94**, 047603 (2005).

[14] D. D. Fong, A. M. Kolpak, J. A. Eastman, S. K. Streiffer, P. H. Fuoss, G. B. Stephenson, C. Thompson, D. M. Kim, K. J. Choi, C. B. Eom, I. Grinberg, and A. M. Rappe, Phys. Rev. Lett. **96**, 127601 (2006).

[15] D. A. Tenne, A. Bruchhausen, N. D. Lanzillotti-Kimura, A. Fainstein, R. S. Katiyar, A. Cantarero, A. Soukiassian, V. Vaithyanathan, J. H. Haeni, W. Tian, D. G. Schlom, K. J. Choi, D. M. Kim, C. B. Eom, H. P. Sun, X. Q. Pan, Y. L. Li, L. Q. Chen, Q. X. Jia, S. M. Nakhmanson, K. M. Rabe, and X. X. Xi, Science **313**, 1614 (2006).

[16] C. L. Jia, V. Nagarajan, J. Q. He, L. Houben, T. Zhao, R. Ramesh, K. Urban, and R. Waser, Nature Mater. **6**, 64 (2007).

[17] J. Junquera and Ph. Ghosez, Nature **422**, 506 (2003).

[18] N. Sai, A. M. Kolpak, and A. M. Rappe, Phys. Rev. B **72**, 020101 (R) (2005).

[19] C.-G. Duan, R. F. Sabiryanov, W. N. Mei, S. S. Jaswal, and E. Y. Tsymbal, Nano Lett. **6**, 483 (2006).

[20] G. Gerra, A. K. Tagantsev, N. Setter, and K. Parlinski, Phys. Rev. Lett. **96**, 107603 (2006).

[21] C.-G. Duan, S. S. Jaswal, E. Y. Tsymbal, Phys. Rev. Lett. **97**, 047201 (2006).

[22] G. Gerra, A. K. Tagantsev, and N. Setter, Phys. Rev. Lett. **98**, 207601 (2007).

[23] M. Y. Zhuravlev, R. F. Sabirianov, S. S. Jaswal, and E. Y. Tsymbal, Phys. Rev. Lett. **94**, 246802 (2005); *ibid*. **102**, 169901 (2009).

[24] H. Kohlstedt, N. A. Pertsev, J. Rodríguez Contreras, and R. Waser, Phys. Rev. B **72**, 125341 (2005).

[25] E. Y. Tsymbal and H. Kohlstedt, Science **313**, 181 (2006).

[26] J. P. Velev, C.-G. Duan, K. D. Belashchenko, S. S. Jaswal, and E. Y. Tsymbal, Phys. Rev. Lett. **98**, 137201 (2007).

[27] V. Garcia, S. Fusil, K. Bouzehouane, S. Enouz-Vedrenne, N. D. Mathur, A. Barthélémy, and M. Bibes, Nature **460**, 81(2009).

[28] M. Y. Zhuravlev, Y. Wang, S. Maekawa, and E. Y. Tsymbal, Appl. Phys. Lett. **95**, 052902 (2009).

[29] A. Gruverman, D. Wu, H. Lu, Y. Wang, H. W. Jang, C. M. Folkman, M. Y. Zhuravlev, D. Felker, M. Rzchowski, C.-B. Eom, and E. Y. Tsymbal, Nano Letters **9**, 3539 (2009).

[30] M. Y. Zhuravlev, S. S. Jaswal, E. Y. Tsymbal, and R. F. Sabirianov, Appl. Phys. Lett. **87**, 222114 (2005); M. Y. Zhuravlev, S. Maekawa, and E. Y. Tsymbal, Phys. Rev. B **81**, 104419 (2010).

[31] M. Gajek, M. Bibes, S. Fusil, K. Bouzehouane, J. Fontcuberta, A. Barthélémy, and A. Fert, Nature Mater. **6**, 296 (2007).

[32] J. P. Velev, C.-G. Duan, J. D. Burton, A. Smogunov, M. K. Niranjan, E. Tosatti, S. S. Jaswal, and E. Y. Tsymbal, Nano Letters **9**, 427 (2009).

[33] V. Garcia, M. Bibes, L. Bocher, S. Valencia, F. Kronast, A. Crassous, X. Moya, S. Enouz-Vedrenne, A. Gloter, D. Imhoff, C. Deranlot, N. D. Mathur, S. Fusil, K. Bouzehouane, and A. Barthélémy, Science **327**, 1106 (2010).

[34] M. Stengel, D. Vanderbilt, and N. A. Spaldin, Nature Mater. **8**, 392 (2009).

[35] N. Nakagawa, H. Y. Hwang, and D. A. Muller, Nature Mater **5**, 204 (2006).

[36] P. Hohenberg and W. Kohn, Phys. Rev. **136**, B864 (1964).

[37] W. Kohn and L. J. Sham, Phys. Rev. **140**, A1133 (1965).

[38] P. E. Blöchl, Phys. Rev. B **50**, 17953 (1994).

[39] G. Kresse and J. Furthmüller, Phys. Rev. B **54**, 11169 (1996).

[40] H. J. Monkhorst and J. D. Pack, Phys. Rev. B **13**, 5188 (1976).

[41] R. Resta, Ferroelectrtics **36**, 51 (1992); R. D. King-Smith and D. Vanderbilt, Phys. Rev. B **47**, 1651 (1993).

[42] R. Pick, M. H. Cohen, and R. M. Martin, Phys. Rev. B **1**, 910 (1970).

[43] P. Ghosez, J. P. Michenaud, and X. Gonze, Physical Review B **58**, 6224 (1998).

[44] J. A. Stroscio, P. N. First, R. A. Dragoset, L. J. Whitman, D. T. Pierce, and R. J. Celotta, J. Vac. Sci. & Tech. A: Vacuum, Surfaces, and Films **8**, 284 (1990).

[45] K. Janicka, J. P. Velev, and E. Y. Tsymbal, Phys. Rev. Lett. **102**, 106803 (2009).

[46] L. D. Landau, e. M. Lifshitz, and L. P. Pitaevskii, *Electrodynamics of Continuous Media* (Pergamon, Oxford, 1984), p. 153.

[47] A. F. Devonshire, Phil. Mag. **40**, 1040 (1949); *ibid.* **42**, 1065 (1951).

[48] R. Kretschmer and K. Binder, Phys. Rev. B **20**, 1065 (1979).

[49] M. D. Glinchuk and A. N. Morozovska, J. Phys.: Condens. Matt. **16**, 3517 (2004).

[50] A. W. Hewat, J. Phys. C: Solid State Physics **6**, 2559 (1973).

[51] Y. L. Li, S. Y. Hu, S. Choudhury, M. I. Baskes, A. Saxena, T. Lookman, Q. X. Jia, D. G. Schlom, and L. Q. Chen, J. Appl. Phys. **104**, 104110 (2008).

[52] Y. L. Li, S. Y. Hu, and L. Q. Chen, J. Appl. Phys. **97**, 034112 (2005).

[53] A. K. Tagantsev and G. Gerra, J. Appl. Phys. **100**, 051607 (2006).

[54] A. Balderschi, S. Baroni, and R. Resta, Phys. Rev. Lett. **61**, 734 (1988).

[55] L. Colombo, R. Resta, and S. Baroni, Phys. Rev. B **44**, 5572 (1991).

List of publications

1. *Metallic and insulating oxide interfaces controlled by electronic correlations*, H. W. Jang, D. A. Felker, C. W. Bark, Y. Wang, M. K. Niranjan, C. T. Nelson, Y. Zhang, D. Su, C. M. Folkman, S. H. Baek, S. Lee, **K. Janicka**, Y. Zhu, X. Q. Pan, D. D. Fong, E. Y. Tsymbal, M. S. Rzchowski and C. B. Eom, *Science* **331**, 886 (2011).
2. *Ferroelectric dead layer driven by a polar interface*,Y. Wang, M. K. Niranjan, **K. Janicka**, J. P. Velev, M. Y. Zhuravlev, S. S. Jaswal, and E. Y. Tsymbal, *Physical Review B* **82**, 094114 (2010).
3. *Quantum Nature of Two-Dimensional Electron Gas Confinement at $LaAlO_3/SrTiO_3$ Interfaces*, **K. Janicka**, J. P. Velev, and E. Y. Tsymbal, *Physical Review Letters* **102**, 106803 (2009).
4. *Magnetism of $LaAlO_3/SrTiO_3$ superlattices*, **K. Janicka**, J. P. Velev, and E. Y. Tsymbal, *Journal of Applied Physics* **103**, 07B508 (2008).
5. *Effects of magnetostatic coupling on stripe domain structures in magnetic multilayers with perpendicular anisotropy*, **K. Janicka**, J. D. Burton, and E. Y. Tsymbal, *Journal of Applied Physics* **101**, 113921 (2007).

6. *Domain overlap in antiferromagnetically coupled [Co/Pt]/NiO/[Co/Pt] multilayers*, A. Baruth, L. Yuan, J. D. Burton, **K. Janicka**, E. Y. Tsymbal, S. H. Liou, and S. Adenwalla, *Applied Physics Letters* **89**, 202505 (2006).

7. *Origin of the interlayer exchange coupling in [Co/Pt]/NiO/[Co/Pt] multilayers studied with XAS, XMCD, and micromagnetic modeling*, A. Baruth, D. J. Keavney, J. D. Burton, **K. Janicka**, E. Y. Tsymbal, L. Yuan, S. H. Liou, and S. Adenwalla, *Physical Review B* **74**, 054419 (2006).